ISBN 978-82-471-2279-2 (printed ver.)
ISBN 978-82-471-2280-8 (electronic ver.)
ISSN 1503-8181

Martin Larsson

Doctoral theses at NTNU, 2010:155

Martin Larsson

Numerical Modeling of Fluid-Structure Interaction in the Human Larynx

NTNU
Norwegian University of
Science and Technology
Thesis for the degree of
philosophiae doctor
Faculty of Engineering Science and Technology
Department of Energy and Process Engineering

Doctoral theses at NTNU, 2010:155

NTNU

Martin Larsson

Numerical Modeling of Fluid-Structure Interaction in the Human Larynx

Thesis for the degree of philosophiae doctor

Trondheim, August 2010

Norwegian University of
Science and Technology
Faculty of Engineering Science and Technology
Department of Energy and Process Engineering

NTNU
Norwegian University of
Science and Technology

NTNU
Norwegian University of Science and Technology

Thesis for the degree of philosophiae doctor

Faculty of Engineering Science and Technology
Department of Energy and Process Engineering

ISBN 978-82-471-2279-2 (printed ver.)
ISBN 978-82-471-2280-8 (electronic ver.)
ISSN 1503-8181

Doctoral Theses at NTNU, 2010:155

Printed by Tapir Uttrykk

NTNU
Det skapende universitet

NORWEGIAN UNIVERSITY OF SCIENCE AND TECHNOLOGY

DOCTORAL THESIS

Numerical Modeling of Fluid-Structure Interaction in the Human Larynx

Author:
Martin LARSSON

Supervisor:
Prof. Bernhard MÜLLER

Faculty of Engineering Science and Technology

Department of Energy and Process Engineering

Trondheim, Norway

August 11, 2010

Abstract

This thesis presents a method for fluid-structure interaction in a simplified 2D model of the human larynx using the arbitrary Lagrangian–Eulerian (ALE) approach and a strictly stable high order finite difference method. The ALE method is first tested for the fluid solver with a prescribed boundary movement, and then the method is extended to a two-way coupled explicit fluid-structure interaction where the vocal folds interact with the airflow in the larynx.

In each case, the fluid is treated as a Newtonian fluid obeying the perfect gas law and laminar flow is always assumed. Since the interest is ultimately phonation, the compressible Navier–Stokes equations are solved in order to resolve both the flow field and the acoustic waves. Characteristic-based non-reflecting boundary conditions are used so that no unphysical reflections occur at the outflow boundary of the limited computational domain.

The finite difference method relies on the summation by parts (SBP) technique which allows energy estimates to be made for the discretized equations in an analogous way as for the continuous problem. In the interior, the difference operator corresponds to the standard sixth order explicit difference method and is third order accurate near the boundaries. The classical explicit fourth order Runge–Kutta method is used for time integration.

For the structure field, the linear elastic wave equation is formulated as a first order system. The spatial derivatives are discretized by the same high order difference operator as employed for the flow equations. To implement boundary conditions for displacement or traction, a simultaneous approximation term (SAT) method is derived. Verification proves that the method is nearly fourth order accurate. The linear model is then extended to a nonlinear hyperelastic model based on a neo-Hookean constitutive relation. The strict energy estimate is only valid for the linear equation, but the SAT approach provides a consistent way to implement the traction boundary condition also for the nonlinear equations.

Fluid-structure interaction simulations are performed with model parameters corresponding to the real geometry of the human larynx and physical properties of the human vocal folds. Results for the vortex dynamics are investigated and preliminary acoustic results are obtained.

Preface

The present doctoral thesis is submitted to the Norwegian University of Science and Technology (NTNU) for the degree Doctor of Philosophy (Ph.D.). The work has been carried out in the Department of Energy and Process Engineering (EPT) under the supervision of Professor Bernhard Müller. The research has been funded by the Swedish Research Council (Vetenskapsrådet) under the project "Numerical Simulation of Respiratory Flow".

Acknowledgments

First and foremost, I would like to thank my supervisor Bernhard Müller who first introduced me to computational fluid dynamics and got me interested in numerical methods for fluid dynamics. His support has been a tremendous driving force and his vast knowledge in the field has been an invaluable asset for the successful conclusion of this project.

I am also grateful for the generous assistance and valuable input from my fellow Ph.D. students in the fluid engineering group at NTNU, Asif Farooq, Claudio Walker and Joris Verschaeve.

Furthermore, I would like to thank professor Bjørn Skallerud at the Department of Structure Engineering at NTNU, whose knowledge in structure dynamics has been a great aid and has helped to steer the project in the right direction.

Last but not least, I would like to thank the people at Aerodynamisches Institut, RWTH Aachen, Wolfgang Schröder, Mathias Meinke and Kai Pielhop, and Siegfried Müller at the Institut für Geometrie und Praktische Mathematik for assistance with verification of the fluid-structure interaction.

Contents

1 Introduction

1.1 Motivation

Fluid-structure interactions (FSIs) occur when a flexible structure interacts with a flowing fluid. The fluid flow exerts an aerodynamic force on the structure which causes it to deform, while the flow induced deformation yields a new structural boundary to which the flow adheres. This inherently two-way coupled interaction is responsible for many different phenomena which are of crucial importance in engineering applications such as aircraft wing flutter and bridge design, where structural motion is undesirable. The study of these phenomena, spurred in part by such catastrophic events as the collapse of the Tacoma Narrows bridge in 1940, has given rise to the scientific field of aeroelasticity.

In engineering applications, aeroelastic effects are usually to be avoided. A design goal for an engineer may be to make a rotating propeller blade as quiet as possible or a bridge insensitive to vibrations caused by the wind. On the other hand, the coupling between fluid flow and structural motion plays an important role in many biological systems such as our cardiovascular and respiratory systems. The pulsatile blood flow in viscoelastic arteries and the transient airflow in the upper airways are the prime examples where FSI effects are in fact desirable. A direct consequence of FSI in the vocal tract is voice production, where the motion of the soft tissue in the vocal folds interacts dynamically with the glottal airflow to produce sound.

Increasing the knowledge of respiratory flow by advanced numerical techniques will be decisive for developing protective respiration concepts to reduce the mortality of artificial respiration. The numerical simulation of pulmonary flow will not only have an impact on the understanding of the physiological conditions and of mechanical ventilation, but also contribute to the investigation of human phonation. With the detailed flow and acoustics information, even diagnostic tools like ultrasound can be further improved.

The vision is that numerical simulation of respiratory flow will contribute to Computer Aided Surgery. The surgeon should be enabled to simulate the consequences of an operation on respiration and phonation before performing the operation. Thus, the operation can be optimally prepared, and the risk for the patient can be minimized.

1.2 Principles of voice production

The vocal folds, also called vocal cords, are two symmetric membranes that protrude from the walls of the larynx at the top of the trachea of humans and most mammals forming a slit-like opening known as the glottis in the airway. In a simplified three-layer model, the vocal folds are composed of the thyroarytenoid muscle, also known as the vocal fold muscle, and the vocal ligament covered by a mucous layer. The parts of the larynx can be seen in Figure 1.

During normal breathing, the vocal tract is open and air can pass unobstructedly. During phonation, the vocal fold muscle is tensed in the longitudinal direction so that the glottal opening becomes narrower. The higher pressure air expelled from the lungs is forced through this narrow opening and starts to push the stationary air column located downstream of the glottis. As the air column gains momentum, pressure builds up behind it causing the vocal folds to open up further. The increase in velocity is then followed by a pressure drop in the glottis according to the Bernouilli principle. The decrease in pressure leads to an aerodynamic force which, together with the elastic force in the vocal folds, strives to close the glottis. As the glottis begins to close, the air flow is restricted leading to a partial vacuum downstream due to the inertia of the air column, contributing to the closure of the glottis. A build-up in pressure upstream before the glottis results from the closure, leading to a pressure force which opens the vocal folds and allows the passage of air. For certain values of vocal muscle tension and lung pressure, this process is able to repeat itself in a self-sustained manner and is driven only by the pressure from the lungs. It is important to point out that no periodic contraction of muscles occurs during phonation. The opening and closing of the glottis is, in this respect, a passive process [28].

During normal speech, the vocal folds collide with each other, closing the glottis completely. However, in certain types of phonation such as a very breathy voice or while whispering, the vocal folds do not necessarily make contact. The outermost mucous layer of the vocal folds has been shown to play an important role in the self-sustained oscillation, facilitating the vibrations of the much stiffer ligament [28, 27].

As the vocal folds oscillate rapidly, they generate a fundamental frequency. When we speak normally only the lowest mode of vibration is excited, in which all the layers of the vocal folds vibrate symmetrically and as a whole.

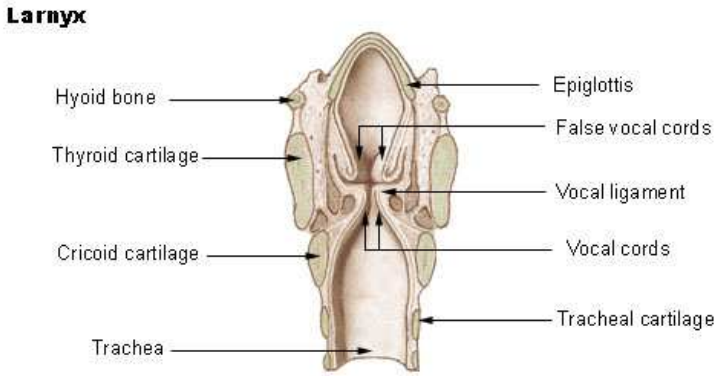

Figure 1: Schematic view of the human larynx, showing in particular the vocal folds and the trachea.

Higher modes of oscillation can, however, be excited to produce higher pitched tones for example when singing. By stretching the vocal fold muscle, the vocal fold length changes as well as the stiffness, and higher modes can thus be created. These higher modes correspond to an oscillation concentrated mainly to the ligament or the mucous layer. The different modes of oscillation are commonly referred to as registers (modal, falsetto etc) and singers are often particularly good at smoothing out the transition between these registers. Going from one register to the next is called registration [27].

The signal resulting from the vocal folds themselves is then further modified by the vocal tract which functions as an acoustic filter. By changing the shape of the vocal tract, different frequencies are amplified and suppressed so that a multitude of different vowels can be formed from the same source signal.

The computational challenge in aeroelastic simulations for human phonation lies in having to deal with unsteady flows at low to moderate Reynolds numbers, large deformations, moving interfaces, fluid-structure interactions and intrinsically 3D motion [9, 28].

1.3 Vocal fold models

Computational models for self-oscillating vocal folds driven by the pressure predicted from the Bernoulli relation were developed in the late 1960s and early 1970s [28, 26]. These very basic models for the vocal folds comprised one or two masses coupled to a spring forming an oscillating mass-spring system. Multi-mass models were subsequently developed in the mid-1970s and these models were used with variations until the mid-1990s when a body-cover for the two-mass model was developed by Story and Titze [23] to incorporate the body-cover model of the vocal folds. Even though the early lumped mass models were elegant in concept, there is considerable doubt that they represent the actual geometry and viscoelastic properties of the vocal folds adequately enough to identify voice disorders and special voice qualities [1]. Therefore, continuum models have been developed for such purposes.

In the mid-1990s, more elaborate models for the vocal folds were developed. Finite element analysis with a continuum model was used by Alipour and Titze [3] to model the vocal fold deformation, coupled to the flow field which was obtained through a Navier–Stokes solver. The advantage with the FEM (finite element method) over lumped multi-mass models is its predictive power and accuracy.

Berry and Titze calculated the eigenmodes and eigenfrequencies of oscillation for a continuum model of the vocal folds using the Ritz method [5]. The model is simplistic as the vocal fold is modeled as a rectangular parallelepiped and aerodynamic forces are absent. However simple, the model is adequate to obtain the analytical eigenmodes. The investigations showed that unlike in the lumped-mass models, two of the lower order modes lie closely spaced in frequency over a wide range of tissue sizes and stiffnesses. These two eigenmodes play a major role in the self-

sustained oscillation of the vocal folds. The fact that their relative frequency does not vary much over different tissue parameters implies that the model is rather insensitive to such parameters. The vocal folds are assumed to be elastic and transversely isotropic, meaning that the tissue is isotropic in the plane transverse to the fibers, while the elastic properties in the direction of the fibers are different from those in the transverse plane. Small oscillations are considered and the following assumptions are made: (1) the stress–strain relation is linear, and (2) all displacements in the direction of the fibers are negligible.

In an attempt to improve over the aforementioned study, Alipour, Berry and Titze presented a model where aerodynamic forces are included and the layered structure of the vocal folds is accounted for [1]. The nonlinear time dependent system of partial differential equations was solved using an FEM code developed at the authors' lab. The field variable that was solved for was the displacement vector. The glottal aerodynamics was modeled with a finite volume solution of the incompressible Navier–Stokes equations [2]. An advantage with the FEM is the ability to handle complex boundaries and driving forces. The simplifying assumptions were (1) small deformations of the structure (linear elasticity), (2) the vibration takes place in a single plane, (3) the tissue layers are either isotropic or transversely isotropic, and (4) the grid motion during finite-element space integration is neglected. The 3D geometry of the vocal fold was divided into thin layers along its length, and a 2D finite element solution was used in each layer [2]. Therefore it is a quasi-three-dimensional (hybrid) model [7].

Recently [7], the box model of the vocal folds first presented in [5] was analyzed further to determine the influence of spatial dimensions on vibratory response in the continuum model and to investigate whether planar displacement is a valid approximation. The material properties and model dimensions were the same as in [5]. But here both an FEM and the Ritz method were used, as opposed to only the Ritz method in [5]. It was found that the eigenfrequencies of the oscillatory modes were most sensitive to the vocal fold length in the longitudinal direction. The assumption of planar displacement was found to be equivalent to infinite longitudinal stiffness E' (in the fiber direction). For values of the stiffness ratio, $n = E'/E$ (where E is the transverse stiffness and $n = 1$ corresponds to isotropy) up to 20, this assumption did not lead to serious errors in the modal frequencies. However, there is currently not enough empirical data to safely state that the stiffness ratio is below 20 [7]. It was also found that out-of-plane stresses have a significant effect on the vibratory response of the continuum model. Thus, two-dimensional structure models may not be sufficient to accurately model the vocal fold dynamics as these do not account for out-of-plane stresses.

Detailed measurements of the vocal fold and glottal channel shape have been performed in [21].

2 Theory

2.1 Fluid

2.1.1 Arbitrary Lagrangian-Eulerian approach

In an Eulerian reference frame, the motion of a fluid is specified at certain points in space through which the fluid moves while the mesh remains fixed. For example, the fluid velocity $\mathbf{u}(\mathbf{x},t)$ and the pressure $p(\mathbf{x},t)$ are defined as functions of the space and time coordinates. In the Lagrangian formulation, on the other hand, the mesh moves with the material. The motion in this case is expressed in terms of displacements from an initial configuration.

In practice, the fluid phase is almost universally described using an Eulerian reference frame (mainly due to its inherent convenience in describing boundary conditions) while it is more natural to use a Lagrangian formulation for the solid phase. Lagrangian descriptions can also be successfully used for contained fluids, but not so much for flowing media, as the mesh would be highly distorted if required to follow the motion of the fluid [11]. These representations are, however, incompatible [4]. But if the deformations are moderate, the Eulerian flow description and the Lagrangian structure description can be combined in an *arbitrary Lagrangian-Eulerian* (ALE) formulation. An ALE formulation comprises both pure Eulerian and pure Lagrangian formulations. This requires a continuous adaption of the mesh without modification of the mesh topology. In an early contribution [11], the ALE formulation was implemented with a finite-element method and applied to incompressible viscous flow.

In the derivation of the Eulerian equations, the velocity of the reference configuration is set to be zero. In an ALE formulation, the mesh is required to adapt to the boundary of the structure. This gives rise to an advective term containing the relative velocity and accounts for transport of material past the moving mesh. This additional term

makes solving the ALE equations more difficult than solving the Lagrangian equations, where the relative velocity is zero [22]. Implementation of the ALE equations can be done in two different ways, corresponding to two approaches taken in implementing the Eulerian viewpoint in fluid mechanics.

– Solution of the fully coupled equations for CFD. This approach can only handle a single material within an element.

– *Operator split* approach. The calculation for each step is divided into two phases: First a Lagrangian phase, in which the mesh moves with the material. Changes in velocity and internal energy due to internal and external forces are calculated. In the second phase, transport of mass, internal energy and momentum across cell boundaries are computed.

An example of the implementation of ALE for fluid-structure coupling, is given in [22]. The authors simulate an underwater explosion where an outgoing spherical pressure wave is incident on a deformable plate. The results show that the plate is able to deform in response to the increasing pressure.

2.1.2 Navier–Stokes equations

In fluid mechanics, the Navier–Stokes equations, named after the engineer Claude-Louis Navier and the mathematician and physicist George Gabriel Stokes, a system of nonlinear partial differential equations, describe the motion of fluids. They can be used to model a wide variety of phenomena on different scales, such as ocean currents, air flow in the atmosphere and the human airways and blood flow in the arteries.

In Cartesian coordinates, the equations of continuity, momentum balance and energy balance can be written

$$\frac{\partial \rho}{\partial t} + \frac{\partial u_i}{\partial x_i} = 0 \tag{1}$$

$$\frac{\partial \rho u_j}{\partial t} + \frac{\partial (\rho u_i u_j)}{\partial x_i} = -\frac{\partial p}{\partial x_j} + \frac{\partial \tau_{ij}}{\partial x_i} + \rho f_j \tag{2}$$

$$\frac{\partial (\rho E)}{\partial t} + \frac{\partial ((\rho E + p) u_i)}{\partial x_i} = \frac{\partial}{\partial x_i}(\tau_{ij} u_j) + \rho f_i u_i - \frac{\partial q_i}{\partial x_i} + r \tag{3}$$

where the Einstein summation convention has been used (sum over repeated indices) and

- t is the time in seconds (s)
- ρ is the mass density in kg/m^3
- u_i are the Cartesian components of the Eulerian velocity field in m/s
- p is the pressure in Pa
- τ_{ij} are components of the viscous stress tensor in Pa
- f_i is an external force density in N/kg
- E is the total energy per unit mass in J/kg
- q_i is the heat flux in the i-direction in $\mathrm{J}/(\mathrm{m}^2 \cdot \mathrm{s})$
- r is the radiation heat loss density in $\mathrm{J}/(\mathrm{m}^3 \cdot \mathrm{s})$.

These equations will now be simplified using a number of assumptions relevant to the flow of air in the human airways and transformed to a form more suitable for computer implementation. One can reasonably assume that the external force f_i, e.g. gravity does not play an important role for the flow and that there are no radiation losses r. Furthermore, perfect gas and Newtonian fluid are reasonable assumptions.

2.1.3 Constitutive relations

The viscous stress tensor for a Newtonian fluid is under the Stokes hypothesis defined by

$$\tau_{ij} = \mu \left(\frac{\partial u_i}{\partial x_j} + \frac{\partial u_j}{\partial x_i} \right) - \frac{2}{3} \mu \frac{\partial u_k}{\partial x_k} \delta_{ij}$$

where the dynamic viscosity μ in units $\mathrm{Pa} \cdot \mathrm{s}$ has been introduced. Fourier's law states that the heat flux is proportional to the temperature gradient through the thermal conductivity κ in $\mathrm{W}/(\mathrm{K} \cdot \mathrm{m})$ by the relation

$$q_i = -\kappa \frac{\partial T}{\partial x_i}.$$

The variation of viscosity as a function of temperature can for gases be modeled by Sutherland's formula which states that

$$\mu(T) = C_1 \frac{T^{3/2}}{T + C_2}$$

where the constants $C_1 = 1.458 \times 10^{-6}\,\mathrm{kg}/(\mathrm{m} \cdot \mathrm{s} \cdot \sqrt{\mathrm{K}})$ and $C_2 = 110.4\,\mathrm{K}$ for air at STP (standard temperature and pressure). For constant Prandtl number ($\mathrm{Pr} = 0.72$ at STP), the thermal conductivity is related to the viscosity by

$$\kappa = \frac{c_p}{\mathrm{Pr}} \mu$$

where $c_p = 1004.5\,\mathrm{m}^2/(\mathrm{K} \cdot \mathrm{s}^2)$ is the specific heat at constant pressure.

2.1.4 Equation of state

The perfect gas law models a theoretical gas where the molecules behave as point particles and do not interact. For air at standard conditions, it is a good assumption and the pressure can thereby be related to the internal energy according to the equation

$$p = (\gamma - 1) \left(\rho E - \frac{1}{2} \rho |\mathbf{u}|^2 \right)$$

where the ratio of specific heats $\gamma = 1.4$ for air.

2.1.5 Perturbation formulation

When variations in the flow field are small compared to their respective stagnation values, as is often the case in low Mach number flow, a finite difference discretization and other discretizations will suffer from cancellation errors. Consider for example the pressure $p = p_\infty + p'$ where p_∞ is the stagnation value and p' is the perturbation. If $p' \ll p_\infty$ then both numbers in the numerator of the finite difference approximation $(p_{i+1} - p_i)/\Delta x$ of $\dfrac{\partial p}{\partial x} = \dfrac{\partial p'}{\partial x}$ at $x = x_i$, are large and cancellation occurs. It is therefore preferable to approximate this derivative by $(p'_{i+1} - p'_i)/\Delta x$ where the constant stagnation pressure has been removed. Expressing the conservative variables as $\mathbf{U}(\mathbf{x},t) = \mathbf{U}_\infty(\mathbf{x},t) + \mathbf{U}'(\mathbf{x},t)$, i.e. as the sum of the stagnation flow state $\mathbf{U}_\infty(\mathbf{x},t)$ and the perturbation $\mathbf{U}'(\mathbf{x},t)$, does not change the equations, but allows for a finite difference discretization or other discretization with minimized cancellation errors.

For the chosen stagnation flow state $\mathbf{U}_\infty(\mathbf{x},t) = (\rho_\infty, \mathbf{0}, (\rho E)_\infty)$, the Navier–Stokes equations in perturbation form can be expressed as [17]

$$\frac{\partial \rho'}{\partial t} + \frac{\partial}{\partial x_i}(\rho u_i)' = 0 \tag{4}$$

$$\frac{\partial}{\partial t}(\rho u_j)' + \frac{\partial}{\partial x_i}((\rho u_i)' u'_j) = -\frac{\partial p'}{\partial x_j} + \frac{\partial \tau'_{ij}}{\partial x_i} + (\rho_\infty + \rho') f_j \tag{5}$$

$$\frac{\partial}{\partial t}(\rho E)' + \frac{\partial}{\partial x_i}[((\rho E)_\infty + (\rho E)' + p_\infty + p') u'_i] = \frac{\partial}{\partial x_i}(\tau'_{ij} u'_j + (\kappa_\infty + \kappa') \frac{\partial T'}{\partial x_i}) + (\rho u_i)' f_i \tag{6}$$

for the vector of unknowns $\mathbf{U}'(\mathbf{x},t) = (\rho', (\rho\mathbf{u})', (\rho E)')^{\mathrm{T}}$, where the perturbation values for the primitive variables are given by $\mathbf{u}' = (\rho\mathbf{u})'/(\rho_\infty + \rho')$, $p' = (\gamma-1)[(\rho E)' - \frac{1}{2}(\rho\mathbf{u})'\cdot\mathbf{u}']$. Furthermore,

$$\tau'_{ij} = (\mu_\infty + \mu')(\frac{\partial u'_j}{\partial x_i} + \frac{\partial u'_i}{\partial x_j}) - \frac{2}{3}(\mu_\infty + \mu')\frac{\partial u'_k}{\partial x_k}\delta_{ij} \tag{7}$$

$$\mu' = \mu(T_\infty + T') - \mu(T_\infty), T' = \frac{p'/R - \rho' T_\infty}{\rho_\infty + \rho'}, \kappa' = \kappa(T_\infty + T') - \kappa(T_\infty) \tag{8}$$

2.1.6 Non-dimensional variables

It is often convenient to go from the dimensional form of the original equations to a non-dimensional form using certain reference values for the variables. From a theoretical viewpoint, the advantage is that the relative importance of each term is easily seen in the equations and which effect a change in any of the model parameters has on the equations. Furthermore, the errors in the arithmetic computations performed by the computer are minimized when all variables in the implementation are scaled to lie in approximately the same range. For internal low Mach number flow, it is preferable to use the stagnation value ρ_∞ for the density, the stagnation speed of sound c_∞ and a characteristic length scale of the domain L_∞ as reference values. The stagnation pressure is given by $p_\infty = \dfrac{\rho_\infty c_\infty^2}{\gamma}$. The non-dimensional quantities are $x^* = \frac{x}{L}, y^* = \frac{y}{L}, u_i^* = \frac{u_i}{c_\infty}, t^* = \frac{tc_\infty}{L}, \rho^* = \frac{\rho}{\rho_\infty}, T^* = \frac{T}{T_\infty}, p^* = \frac{p}{\rho_\infty c_\infty^2}, E^* = \frac{E}{c_\infty^2}$.

When non-dimensionalizing μ and κ, a special choice is made so that the non-dimensional equations assumes exactly the same form as its dimensional counterpart. This choice consists of specifying

$$\mu^* = \frac{1}{\mathrm{Re}_\infty}\frac{\mu}{\mu_\infty}, \quad k^* = \frac{1}{(\gamma-1)\mathrm{Pr}_\infty \mathrm{Re}_\infty}\frac{\kappa}{\kappa_\infty} \tag{9}$$

where the reference Reynolds and Prandtl numbers are given by

$$\mathrm{Re}_\infty = \frac{\rho_\infty c_\infty L_\infty}{\mu_\infty}, \quad \mathrm{Pr}_\infty = \frac{c_p \mu_\infty}{\kappa_\infty}. \tag{10}$$

Henceforth, the superscript * is dropped from the notation and all variables are assumed dimensionless. Using the non-dimensional variables in perturbation formulation, the 2D Navier–Stokes equations can be compactly written as

$$\mathbf{U}'_t + \mathbf{F}'_x + \mathbf{G}'_y = 0, \tag{11}$$

where $\mathbf{U}'(\mathbf{x},t)$ is the vector of conservative perturbation variables, and the perturbation fluxes split up into their viscous and inviscid parts are $\mathbf{F}' = \mathbf{F}^{c\prime} - \mathbf{F}^{v\prime}$ and $\mathbf{G}' = \mathbf{G}^{c\prime} - \mathbf{G}^{v\prime}$. Explicit expressions are given below.

$$\mathbf{F}^{c\prime} = \begin{pmatrix} (\rho u)' \\ (\rho u)'u' + p' \\ (\rho v)'u' \\ ((\rho H)_\infty + (\rho H)')u' \end{pmatrix}, \quad \mathbf{G}^{c\prime} = \begin{pmatrix} (\rho v)' \\ (\rho u)'v' \\ (\rho v)'v' + p' \\ ((\rho H)_\infty + (\rho H)')v' \end{pmatrix} \tag{12}$$

$$\mathbf{F}^{v\prime} = \begin{pmatrix} 0 \\ \tau'_{xx} \\ \tau'_{xy} \\ u'\tau'_{xx} + v'\tau'_{xy} + kT'_x \end{pmatrix}, \quad \mathbf{G}^{v\prime} = \begin{pmatrix} 0 \\ \tau'_{yx} \\ \tau'_{yy} \\ u'\tau'_{yx} + v'\tau'_{yy} + kT'_y \end{pmatrix} \tag{13}$$

where the stagnation total enthalpy is given by $(\rho H)_\infty = (\rho E)_\infty + p_\infty$ and the total enthalpy perturbation $(\rho H)'$ by $(\rho H)' = (\rho E)' + p'$.

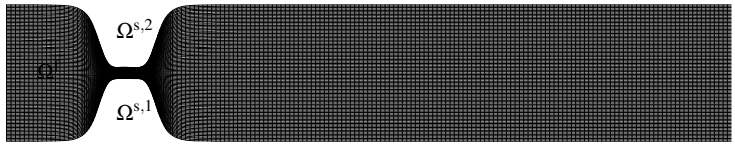

Figure 2: Typical mesh for the vocal tract. The time-dependent mesh region $\Omega^{f}(t)$ is determined by the displacement of the structure on the fluid-structure interface.

2.1.7 ALE formulation for the Navier–Stokes equations

To be able to perform calculations for general geometries such as the human larynx, cf. Fig. 2, the physical coordinates x, y in the physical domain are transformed to Cartesian coordinates ξ, η on a rectangular domain in the computational plane. For moving geometries the transformation will also depend on time, i.e. for each time instant, the mapping $x = x(\xi, \eta)$ will be different. The general coordinate transformation can be summarized as

$$\begin{aligned} x &= x(\xi, \eta, \tau) \\ y &= y(\xi, \eta, \tau) \\ t &= \tau \end{aligned} \tag{14}$$

The time dependent metric terms and Jacobian determinant of the transformation are

$$J^{-1}\xi_x = y_\eta, \quad J^{-1}\xi_y = -x_\eta, \quad J^{-1}\eta_x = -y_\xi, \quad J^{-1}\eta_y = x_\xi, \quad J^{-1} = x_\xi y_\eta - x_\eta y_\xi. \tag{15}$$

If analytical expressions for the inverse transformation are available, the 2D metric terms can be calculated analytically [25]. If on the other hand the transformation is a result of a grid generation scheme, finite difference approximations in the computational plane must be employed to obtain the metric terms. For example, the evaluation of $J^{-1}\eta_y = x_\xi$ at a grid point i, j using a central second order approximation could be approximated as

$$(x_\xi)_{i,j} \approx \frac{x_{i+1,j} - x_{i-1,j}}{2\Delta\xi} \tag{16}$$

where i, j are the grid point indices and $\Delta\xi$ is the grid spacing. As the domain changes with time, each point moves with a certain velocity prescribed by the time dependent coordinate transformation $\dot{x} = x_\tau, \dot{y} = y_\tau$. These are the velocities of the grid point at the location x, y. These give rise to the metric terms

$$\begin{aligned} \xi_t &= -\xi_x \dot{x} - \xi_y \dot{y} \\ \eta_t &= -\eta_x \dot{x} - \eta_y \dot{y} \end{aligned} \tag{17}$$

The 2D Navier–Stokes equations in ALE form are then [20]

$$\mathbf{U}'_\tau = \frac{1}{J^{-1}}(-\hat{\mathbf{F}}'_\xi - \hat{\mathbf{G}}'_\eta - (J^{-1})_\tau \mathbf{U}') \tag{18}$$

where the transformed flux vectors are

$$\hat{\mathbf{F}}' = J^{-1}(\xi_t \mathbf{U}' + \xi_x \mathbf{F}' + \xi_y \mathbf{G}'), \quad \hat{\mathbf{G}}' = J^{-1}(\eta_t \mathbf{U}' + \eta_x \mathbf{F}' + \eta_y \mathbf{G}'). \tag{19}$$

The time derivative of the Jacobian determinant is given by the geometric conservation law

$$(J^{-1})_\tau + (J^{-1}\xi_t)_\xi + (J^{-1}\eta_t)_\eta = 0, \tag{20}$$

because the ξ- and η-derivatives in (20) are calculated from the grid point velocities (17).

2.2 Structure

2.2.1 Linear elasticity

The extension of a linear spring resulting from an applied force is expressed by the linear relation $F = -kx$ known as Hooke's law, where F is the applied force, x is the displacement of the spring from its equilibrium length and k is the spring constant in N/m. An elastic rod with cross sectional area A can be modeled as a linear spring. When the rod is loaded with a force, its cross-section changes and the molecules rearrange which, if the deformations are large enough changes the stress-strain relationship in the rod and Hooke's law is no longer valid. However, for some materials under certain loading conditions, i.e. within the elastic range of the material, Hooke's law is a good approximation.

When we make the assumption that the deformations are small enough that the restoring force in the material is proportional to the deformation, we arrive at the theory of linear elasticity. When the deformations are larger, the response may be nonlinear, but the linear model will still hold as a first approximation in this case. For even larger deformations, the bonds between the molecules in the material will break irreparably causing the material to adopt a new configuration and undergo what is known as plastic deformation.

The displacement of a deformable solid is defined in terms of the displacement vector $\mathbf{p}$ from its equilibrium position.

$$\mathbf{p} = \mathbf{p}(x,y,z,t) = p_1(x,y,z,t)\mathbf{e}_1 + p_2(x,y,z,t)\mathbf{e}_2 + p_3(x,y,z,t)\mathbf{e}_3$$

The velocity is the time derivative of the displacement vector.

$$\mathbf{u} = \mathbf{u}(x,y,z,t) = \frac{\partial \mathbf{p}}{\partial t} = \dot{p}_1(x,y,z,t)\mathbf{e}_1 + \dot{p}_2(x,y,z,t)\mathbf{e}_2 + \dot{p}_3(x,y,z,t)\mathbf{e}_3$$

The Cauchy strain tensor $\boldsymbol{\varepsilon}$ is defined in terms of the displacement vector by

$$\varepsilon_{ij} = \frac{1}{2}\left(\frac{\partial p_i}{\partial x_j} + \frac{\partial p_j}{\partial x_i}\right), \quad i,\ j = 1,\ 2,\ 3$$

Note that the strain tensor is symmetric and therefore has 6 independent components in 3D.

Arranging the 6 independent components of the strain tensor into a 1D vector, Hooke's law in 3D can be expressed in the form $\boldsymbol{\sigma} = S\boldsymbol{\varepsilon}$ where S is the 6×6 stiffness matrix and $\boldsymbol{\sigma}$ is the tensile (Cauchy) stress.

For the human vocal folds, the elastic properties in the longitudinal direction, i.e. along the vocal fold muscle (here, the y-direction), deviate significantly from those in the plane perpendicular to this direction. Refering to Fig. 1 showing a cut in the xz-plane, the fibers of the vocal fold muscle extend in the direction perpendicular to the plane. Assuming transverse isotropy, Hooke's law takes the form [13]

$$\begin{bmatrix} \varepsilon_{11} \\ \varepsilon_{22} \\ \varepsilon_{33} \\ \varepsilon_{12} \\ \varepsilon_{23} \\ \varepsilon_{13} \end{bmatrix} = \begin{bmatrix} 1/E & -\nu'/E' & -\nu/E & 0 & 0 & 0 \\ -\nu'/E & 1/E' & -\nu'/E & 0 & 0 & 0 \\ -\nu/E & -\nu'/E' & 1/E & 0 & 0 & 0 \\ 0 & 0 & 0 & 1/(2\mu') & 0 & 0 \\ 0 & 0 & 0 & 0 & 1/(2\mu') & 0 \\ 0 & 0 & 0 & 0 & 0 & (1+\nu)/E \end{bmatrix} \begin{bmatrix} \sigma_{11} \\ \sigma_{22} \\ \sigma_{33} \\ \sigma_{12} \\ \sigma_{23} \\ \sigma_{13} \end{bmatrix}$$

where primed variables represent quantities in the longitudinal fiber axis and unprimed variables stand for their transverse counterparts. E and ν are Young's modulus and Poisson's ratio, respectively.

Inverting this matrix equation gives the stresses expressed as functions of the strains. When displacement in the y-direction is neglected, using the definition of the strain tensor and taking the time derivative of the final result, the

following system of evolution equations is obtained for the stress components,

$$\frac{\partial}{\partial t}\sigma_{11} = c_1\mu\frac{\partial u}{\partial x} + c_2\mu\frac{\partial w}{\partial z} \tag{21}$$

$$\frac{\partial}{\partial t}\sigma_{22} = 0 \tag{22}$$

$$\frac{\partial}{\partial t}\sigma_{33} = c_2\mu\frac{\partial u}{\partial x} + c_1\mu\frac{\partial w}{\partial z} \tag{23}$$

$$\frac{\partial}{\partial t}\sigma_{12} = 2\mu'\frac{\partial u}{\partial y} \tag{24}$$

$$\frac{\partial}{\partial t}\sigma_{23} = 2\mu'\frac{\partial w}{\partial y} \tag{25}$$

$$\frac{\partial}{\partial t}\sigma_{13} = 2\mu(\frac{\partial w}{\partial x} + \frac{\partial u}{\partial z}). \tag{26}$$

where $c_1 = 2(\alpha - \nu'^2)/(\alpha(1-\nu) - 2\nu'^2)$, $c_2 = 2(\alpha\nu - \nu'^2)/(\alpha(1-\nu) - 2\nu'^2)$, $\mu = E/2(1+\nu)$ and $\alpha = E'/E$. Conservation of momentum gives

$$\rho\frac{\partial}{\partial t}u = \frac{\partial\sigma_{11}}{\partial x} + \frac{\partial\sigma_{12}}{\partial y} + \frac{\partial\sigma_{13}}{\partial z} \tag{27}$$

$$\rho\frac{\partial}{\partial t}v = 0 \tag{28}$$

$$\rho\frac{\partial}{\partial t}w = \frac{\partial\sigma_{31}}{\partial x} + \frac{\partial\sigma_{32}}{\partial y} + \frac{\partial\sigma_{33}}{\partial z} \tag{29}$$

Finally, in 2D, all variations in the y-direction are neglected and the following first-order system for the five unknowns $u, w, \sigma_{11}, \sigma_{13}, \sigma_{33}$ is obtained,

$$\rho\frac{\partial}{\partial t}u = \frac{\partial\sigma_{11}}{\partial x} + \frac{\partial\sigma_{13}}{\partial z} \tag{30}$$

$$\rho\frac{\partial}{\partial t}w = \frac{\partial\sigma_{13}}{\partial x} + \frac{\partial\sigma_{33}}{\partial z} \tag{31}$$

$$\frac{\partial}{\partial t}\sigma_{11} = c_1\mu\frac{\partial u}{\partial x} + c_2\mu\frac{\partial w}{\partial z} \tag{32}$$

$$\frac{\partial}{\partial t}\sigma_{13} = 2\mu(\frac{\partial w}{\partial x} + \frac{\partial u}{\partial z}) \tag{33}$$

$$\frac{\partial}{\partial t}\sigma_{33} = c_2\mu\frac{\partial u}{\partial x} + c_1\mu\frac{\partial w}{\partial z} \tag{34}$$

where the symmetry of σ has been used.

2.2.2 Linear elastic wave equation in 2D

The linear elastic wave equation in second order form in 2D reads

$$\rho p_{tt} = (\lambda + 2\mu)p_{xx} + \mu p_{yy} + (\lambda + \mu)q_{xy}$$
$$\rho q_{tt} = (\lambda + 2\mu)q_{yy} + \mu q_{xx} + (\lambda + \mu)p_{xy}$$

Making the change of variables

$$u = p_t$$
$$v = q_t$$
$$f = (2\mu + \lambda)p_x + \lambda q_y$$
$$g = \mu(q_x + p_y)$$
$$h = \lambda p_x + (2\mu + \lambda)q_y$$

leads to a first-order formulation

$$\begin{aligned} \rho u_t &= f_x + g_y \\ \rho v_t &= g_x + h_y \\ f_t &= (2\mu+\lambda)u_x + \lambda v_y \\ g_t &= \mu(v_x + u_y) \\ h_t &= \lambda u_x + (2\mu+\lambda)v_y \end{aligned} \tag{35}$$

which is identical to (30) after the substitutions

$$\begin{aligned} &x \longrightarrow x, \quad z \longrightarrow y, \quad u \longrightarrow u, \quad w \longrightarrow v \\ &2\mu \longrightarrow \mu, \quad c_2\mu \longrightarrow \lambda, \quad c_1\mu \longrightarrow \lambda + 2\mu \\ &\sigma_{11} \longrightarrow f, \quad \sigma_{13} \longrightarrow g, \quad \sigma_{33} \longrightarrow h. \end{aligned}$$

Thus, the 2D linear elastic wave equation is the basic equation for describing the kinematics of a transversely isotropic material. The Lamé parameters λ, μ in (35) are given by the material properties E, E', ν, ν' as the functions

$$\mu = \mu(E, E', \nu, \nu'), \quad \lambda = \lambda(E, E', \nu, \nu')$$

depending on the structure model.

2.2.3 Nonlinear kinematics

The basic equations for structure mechanics when large deformations and nonlinear effects are taken into account are the Lagrangian field equations which arise from Newton's second law applied to a continuum. For large deformation elasticity a Lagrangian viewpoint is adopted, meaning that the motion of each material particle is expressed as a function of its position in a reference configuration and time. Thus, the displacement field is $\mathbf{p} = \mathbf{p}(\mathbf{x}, t)$ where $\mathbf{x}$ is a coordinate in the reference configuration, $\mathbf{p}(\mathbf{x}, t)$ is the displacement of the particle situated at $\mathbf{x}$ and $\mathbf{x}'(\mathbf{x}, t) = \mathbf{x} + \mathbf{p}(\mathbf{x}, t)$ is the current position of the particle.

Let a deformable body occupy some domain Ω_0 in space. The set Ω_0 is called the reference configuration of the body. As the body translates, rotates and deforms through space, the particle originally at position $\mathbf{x}$ is at a later time found at a new position $\mathbf{x} + \mathbf{p}(\mathbf{x}, t)$ in the current configuration of the body Ω. The basic measure of deformation in the body is the deformation gradient $\mathbf{F} = \mathbf{1} + \nabla_{\mathbf{x}}\mathbf{p}(\mathbf{x}, t)$. An infinitesimal line element in the reference configuration $d\mathbf{x}$ transforms to $dx_i' = (\partial x_i'/\partial x_\alpha)dx_\alpha = F_{i\alpha}dx_\alpha$ where $x_i'(\mathbf{x}, t) = x_i + p_i(\mathbf{x}, t)$ is the new position.

The Lagrangian field equations in 2D are [18]

$$\begin{aligned} \rho p_{tt} &= (S_{11})_x + (S_{21})_y \\ \rho q_{tt} &= (S_{12})_x + (S_{22})_y \end{aligned}$$

where $\mathbf{S} = \Sigma\mathbf{F}^{\mathrm{T}}$ is the nominal stress tensor and the components of the deformation gradient are

$$\mathbf{F} = \begin{bmatrix} \partial x'/\partial x & \partial x'/\partial y \\ \partial y'/\partial x & \partial y'/\partial y \end{bmatrix} = \begin{bmatrix} 1 + p_x & p_y \\ q_x & 1 + q_y \end{bmatrix}.$$

The components of the symmetric Piola-Kirchhoff stress tensor are functions of the deformation gradient, i.e.

$$\Sigma = \begin{bmatrix} f & g \\ g & h \end{bmatrix}$$

where $f = f(p_x, p_y, q_x, q_y)$ and similarly for g and h.

2.2.4 Constitutive relations

The functional dependence of $\boldsymbol{\Sigma}$ comes from a constitutive model. Here, the neo-Hookean model is used. The stress tensor is derived from a strain energy potential function and the resulting expression is

$$\boldsymbol{\Sigma} = \mu\mathbf{1} + \left(\frac{\lambda}{2}\ln(\det\mathbf{C}) - \mu\right)\mathbf{C}^{-1}. \tag{36}$$

where the right Cauchy–Green strain tensor $\mathbf{C}$ is given by $\mathbf{C} = \mathbf{F}^{\mathrm{T}}\mathbf{F}$, cf. PAPER2 of this thesis for more details. The constitutive relation (36) gives rise to the second Piola–Kirchhoff stress components

$$\begin{aligned} f &= (2\mu+\lambda)p_x + \lambda q_y + \mathscr{O}(p_x^2+p_y^2+q_x^2+q_y^2) \\ g &= \mu(q_x+p_y) + \mathscr{O}(p_x^2+p_y^2+q_x^2+q_y^2) \\ h &= \lambda p_x + (2\mu+\lambda)q_y + \mathscr{O}(p_x^2+p_y^2+q_x^2+q_y^2). \end{aligned} \tag{37}$$

When the deformations are small, the expressions (37) reduce to the linear elastic wave equation. Taking the time-derivative of the constitutive relation $\Sigma = \Sigma(p_x, p_y, q_x, q_y)$ gives a time evolution equation for each component of Σ, namely

$$\frac{\partial}{\partial t}\Sigma = \frac{\partial}{\partial t}\Sigma(p_x,p_y,q_x,q_y) = \frac{\partial \Sigma}{\partial p_x}\underbrace{\frac{\partial p_x}{\partial t}}_{u_x} + \ldots$$

Furthermore, the time evolution of the displacement is determined by the velocity,

$$\frac{\partial}{\partial t}p = u, \quad \frac{\partial}{\partial t}q = v$$

and the Lagrangian field equations expressed in terms of components of the second Piola–Kirchhoff stress tensor are

$$\begin{aligned} \rho u_t &= [(1+p_x)f + p_y g]_x + [(1+p_x)g + p_y h]_y \\ \rho v_t &= [q_x f + (1+q_y)g]_x + [q_x g + (1+q_y)h]_y \end{aligned}$$

which reduces to the linear elastic equations when the deformation gradient is small, i.e. $|p_x| \ll 1$ etc.

The close relation between the linear elastic wave equation and the nonlinear equation based on the neo-Hookean model allows for simple theoretical models to be developed for the linear case and then to be directly applied to the nonlinear equations. In PAPER5, simultaneous approximation term (SAT) expressions were derived for the linear elastic wave equation which can be used for the nonlinear equations knowing that they are exact for small deformations and a good approximation for larger deformations.

2.3 Fluid-structure interaction

2.3.1 Fluid-structure models

The structural motion is determined by a variety of force distributions, e.g. inertial, structural damping, stiffness and aerodynamic forces [29]. When solving FSI problems one must consider the two-way coupling between the distinct physical models, i.e. between fluid and solid mechanics. This can be accomplished in either direct or sequential multidisciplinary approaches [12]. In the direct coupled field analysis approach, one tries to solve for all the degrees of freedom of the system in one single sweep, whereas in the sequential coupling approach, the flow and structure solvers are applied sequentially and coupling is achieved iteratively. For example, the results of one flow solver iteration, is passed on as loads, e.g. pressure, to the structure solver and iterated until a convergence criterion has been met for the loads, cf. [29, 8]. Treating the flow and structural equations as one monolithic system seems like an attractive approach from a modeling point of view. In doing so, however, one has to sacrifice efficiency and to restrict to smaller-scale aeroelastic problems [29]. Historically, solution techniques for the different physical fields have evolved separately and naturally one seeks to make use of the mature techniques already available in the separate fields. Therefore, sequential coupling procedures are almost always used in current research, treating the flow and structure separately and coupling through a synchronization technique in space and time.

An interesting approach employing a three-field model (fluid, solid an acoustic) has been studied in [14]. The incompressible Navier–Stokes equations are used to solve the flow field and Lighthill's acoustic analogy is employed to obtain the acoustic field.

2.3.2 Immersed boundary methods

In the immersed boundary (IB) method, presented in [19], moving boundaries of a geometry are represented as a field of forces on the rectangular fluid mesh. The author developed this method for the purpose of simulating blood flow in the heart, where the tissue can be considered incompressible, i.e. of constant density ρ. A single divergence-free velocity field was used to describe motion of the blood, valves and heart muscle. Instead of having to adapt the mesh to the moving walls of the heart, the velocity field was defined on a larger fixed periodic domain filled with fluid. The presence of the external fluid was assumed to have little effect on the internal flow pattern, provided that the periodic mesh was big enough and that external sources and sinks are provided to account for volume changes in the heart during the cardiac cycle. Because of the periodicity, no special treatment for external boundaries was required. To describe the forces acting on the heart, a force density was introduced. This force density should be nonzero only in the non-fluid regions and added as an external force to the Navier–Stokes system. The same equations could then be used on the entire periodic domain. A Lagrangian representation was used to obtain the spatial configuration of the internal boundary. This was needed in order to calculate the aforementioned force field due to the immersed boundary. A set of massless points moving with the local fluid velocity was used to specify the configuration of the boundary, and a force density expressed in terms of those points specified the boundary force field. Tension forces were imposed point-wise and distributed to neighboring nodes. According to the author, the strength of this method lies in its generality. Investigations can be performed for arbitrary complexity and design parameters of the heart or other structures without changing the method.

In recent years, the popularity of IB methods has grown considerably [16], because they allow researchers to easily develop computational models for flows with complex geometries and moving boundaries which would have been difficult or impossible with boundary fitted mesh techniques. Without the need for complex grids, setting up and initiating a simulation can be done with relative ease. The drawback with these methods is their accuracy. For high Reynolds numbers, the solver needs to accurately resolve the boundary layers on the immersed surface, which is challenging if the surface is not aligned with the grid lines. The local accuracy near the immersed boundary can be improved by modifying the computational stencil near the surface and two methods for doing this are discussed in [16]. The advantages of IB methods are that they are simple to implement, can be used on rectangular Cartesian grids, allowing fast solvers to be used and are well-suited for flows with elastic boundaries.

Recently [15], immersed boundary methods have been applied to model phonation.

2.3.3 Present FSI approach

Consider the 2D linear elastic wave equation (35) written in first order form. The traction boundary condition, which specifies an applied force per unit area on any part of the boundary, is given by $\boldsymbol{\Sigma}\mathbf{n} = \mathbf{T}(\mathbf{x},t)$ where $\boldsymbol{\Sigma}$ is the symmetric stress tensor, $\mathbf{n}$ is the outward unit normal on the boundary and $\mathbf{T}(\mathbf{x},t)$ is the given traction on the boundary. This leads to a system of equations at each point on the boundary

$$\begin{aligned} fn_x + gn_y &= t_x \\ gn_x + hn_y &= t_y \end{aligned}$$

where the symmetric stress components f, g and h are to be determined. However, as there is not enough data to determine all three of the variables, only linear combinations of f, g and h can be determined. Hence the injection method does not work for the traction boundary condition, i.e. it is not possible to give, say f, a definite value after a complete time step in the Runge–Kutta method. These boundary conditions can, however, be implemented consistently when employing the simultaneous approximation term (SAT) method, as was shown in PAPER5.

The force on the structure is calculated from the fluid stress $\boldsymbol{\sigma} = \boldsymbol{\tau} - p\mathbf{1}$ by $\mathbf{T}(\mathbf{x},t) = \boldsymbol{\sigma}\mathbf{n}$. The unit normal can be calculated from the coordinate transformation as illustrated in PAPER5. Since both the flow and structure equations are solved explicitly, no iterations are needed and the present FSI code is easily parallelizable. The time step is determined by the stability condition for the Navier–Stokes equations. The fluid-structure interaction algorithm is summarized below.

1. Generate the initial fluid mesh based on the reference configuration for the structure. $\Rightarrow x^0, \dot{x}^0$.
2. Give initial values for the fluid and the structure. $\Rightarrow F^0, S^0$.

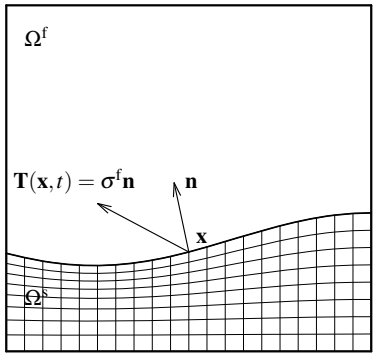

(a) The traction vector $\mathbf{T}(\mathbf{x},t)$ exerted on the structure by the fluid is calculated on the fluid-structure interface as the fluid stress tensor times the outward unit normal.

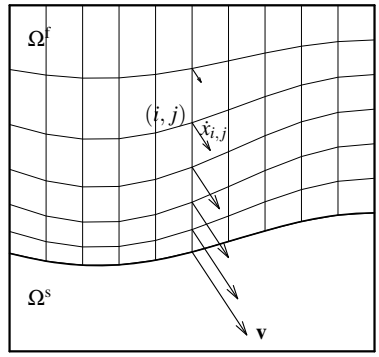

(b) The grid point velocity $\dot{x}_{i,j}$ at grid point (i,j) is interpolated from the given velocity $\mathbf{v}$ of the structure on the interface.

Figure 3: Illustration of fluid-structure interaction algorithm.

3. For time step $n = 1, 2, ...,$ do:

   (a) Calculate the fluid stress on the boundary and calculate the force per unit area, i.e. traction, on the structure via the unit normal. Store the traction vector $\mathbf{T}^n$.

   (b) Take one time step for the fluid: $F^{n+1} = F(x^n, \dot{x}^n)$.

   (c) Calculate the traction force from the fluid on the structure on the boundary, cf. Fig. 3(a). $\Rightarrow \mathbf{T}^{n+1}$.

   (d) Take one time step for the structure using the boundary conditions $\mathbf{T}^n$: $S^{n+1} = S(\mathbf{T}^n)$.

   (e) Recalculate the fluid grid and the grid point velocities based on the new structure solution, cf. Fig. 3(b). $\Rightarrow x^{n+1}, \dot{x}^{n+1}$.

4. Repeat from 3 with time step $n+1$ until the final time is reached.

3 Numerical modeling

3.1 High order finite difference methods

Throughout the history of CFD and computational mechanics, low order methods have held a dominant position, mainly due to the simplicity of computer implementation of these algorithms. In recent years, however, high order methods have gained momentum thanks to their efficiency. For problems where high accuracy is required, and especially in 2D and 3D applications, high order methods outperform their low order counterparts in terms of computer power invested for a given error tolerance.

3.2 Energy method

The energy method is a general technique to prove sufficient conditions for well-posedness of partial differential equations (PDE) and stability of difference methods with general boundary conditions [10].

Consider the solution of the model problem in 1D with

$$u_t = \lambda u_x,\ \lambda > 0,\ 0 \le x \le 1,\ t \ge 0,\ u(x,0) = f(x),\ u(1,t) = g(t). \tag{38}$$

Here, the symbol λ represents a general eigenvalue of the hyperbolic system and should not be confused with the Lamé parameter. Define the L_2 scalar product for real functions v and w on the interval $0 \leq x \leq 1$ as

$$(v,w) = \int_0^1 v(x)w(x)dx \tag{39}$$

which defines a norm of the continuous solution at some time t and an energy $E(t) = ||u(\cdot,t)||^2 = (u,u)$. Using integration by parts $(v,w_x) = v(1,t)w(1,t) - v(0,t)w(0,t) - (v_x,w)$, we get $\frac{dE}{dt} = \frac{d||u||^2}{dt} = (u_t,u) + (u,u_t) = \lambda[(u_x,u) + (u,u_x)] = \lambda[(u_x,u) + [u^2]_0^1 - (u_x,u)] = \lambda[u^2(1,t) - u^2(0,t)]$. If $\lambda > 0$, the boundary condition $u(1,t) = 0$ yields a non-growing solution, i.e. $E(t) \leq E(0) = ||f(x)||^2$. Note that periodic boundary conditions would also yield a non-growing solution. Thus, the energy of the solution is bounded by the energy of the initial data. We know that the solution of (38) exists and is unique. Hence, the problem is well-posed.

3.3 Summation by parts operators

The idea behind the summation by parts technique, cf. e.g. [24, 6, 10], is to use an operator Q to approximate $\partial/\partial x$ and a quadrature rule H to approximate $\int_0^1 ...dx$ in order to satisfy the corresponding discrete property to integration by parts of the continuous function, called the summation by parts (SBP) property. For the numerical solution of (38), we introduce the equidistant grid $x_j = jh$, $j = 0,...,N$, $h = 1/N$, and a solution vector containing the solution at the discrete grid points, $\mathbf{u} = (u_0(t), u_1(t), ..., u_N(t))^{\mathrm{T}}$. The semi-discrete problem can be stated using a difference operator Q approximating the first derivative,

$$\frac{d\mathbf{u}}{dt} = \lambda Q\mathbf{u},\ u_i(0) = f(x_i). \tag{40}$$

We also define a discrete scalar product and corresponding norm and energy by

$$(\mathbf{u},\mathbf{v})_h = h\sum_{i,j} h_{ij}u_iv_j = h\mathbf{u}^{\mathrm{T}}H\mathbf{v}, \quad E_h(t) = ||\mathbf{u}||_h^2 = (\mathbf{u},\mathbf{u})_h, \tag{41}$$

where the symmetric and positive definite quadrature matrix $H = \mathrm{diag}(H_L, I, H_R)$ has components h_{ij}. In order for (41) to define a scalar product, H_L and H_R must be symmetric and positive definite. We say that the scalar product satisfies the summation by parts property (SBP), if

$$(\mathbf{u},Q\mathbf{v})_h = u_Nv_N - u_0v_0 - (Q\mathbf{u},\mathbf{v})_h. \tag{42}$$

It can be seen that this property is satisfied if the matrix $G = HQ$ satisfies the condition that $G + G^{\mathrm{T}} = \mathrm{diag}(-1,0,...,0,1)$. If Q and its corresponding quadrature matrix H satisfy the SBP property (42), then the energy method for the discrete problem yields:

$$\frac{dE_h}{dt} = \frac{d||u||_h^2}{dt} = (u_t,u)_h + (u,u_t)_h = \lambda[(Qu,u)_h + (u,Qu)_h] = \lambda[(Qu,u)_h + u_N^2 - u_0^2 - (Qu,u)_h] = \lambda[u_N^2 - u_0^2]. \tag{43}$$

For diagonal H_L and H_R there exist difference operators Q accurate to order $\mathcal{O}(h^{2s})$ in the interior and $\mathcal{O}(h^s)$ near the boundaries for $s = 1,2,3$ and 4. These operators have an effective order of accuracy $\mathcal{O}(h^{s+1})$ in the entire domain. Explicit forms of such operators Q and norm matrices H were derived by Strand [24].

3.4 Simultaneous approximation terms

Since the term λu_N^2 in (43) is non-negative, strict stability, i.e. $dE_h/dt \leq 0$ here, does not follow when using the injection method for the summation by parts operator, i.e. by using $u_N(t) = g(t)$ for injection affects the operator Q and the SBP property (42). In contrast, the simultaneous approximation term (SAT) method is an approach where a linear combination of the boundary condition and the differential equation is solved at the boundary. This leads to a weak imposition of the physical boundary conditions. The imposition of SAT boundary conditions is accomplished by adding a source term to the derivative operator, proportional to the difference between the value of the discrete

solution u_N and the boundary condition to be fulfilled. The SAT method for the semi-discrete advection equation (40) can be expressed as

$$\frac{d\mathbf{u}}{dt} = \lambda Q\mathbf{u} - \lambda\tau\mathbf{S}(u_N - g(t))$$

where $\mathbf{S} = h^{-1}H^{-1}(0,0,...,0,1)^{\mathrm{T}}$ and τ is a free parameter.

The added term does not alter the accuracy of the scheme, since it vanishes when the analytical solution is substituted. Thus, we can imagine the SAT expression as a modification to the difference operator so that we are effectively solving an equation $\mathbf{u}_t = \lambda\tilde{Q}\mathbf{u}$ with $\tilde{Q} = Q + Q^{\mathrm{sat}}$ without imposing the boundary conditions directly. When H is diagonal, the scheme is only modified at one point on the boundary. We can now show that this scheme is strictly stable for $g(t) = 0$. The energy rate for the solution of the semi-discrete equation is $\frac{dE_h}{dt} = \frac{d||u||_h^2}{dt} = (\mathbf{u}_t,\mathbf{u})_h + (\mathbf{u},\mathbf{u}_t)_h$ $= \lambda[(\mathbf{u},Q\mathbf{u} - \tau\mathbf{S}u_N)_h + (Q\mathbf{u} - \tau\mathbf{S}u_N,\mathbf{u})_h] = \lambda[(\mathbf{u},Q\mathbf{u})_h - \tau(\mathbf{u},\mathbf{S})_h u_N + (Q\mathbf{u},\mathbf{u})_h - \tau(\mathbf{S},\mathbf{u})_h u_N] = \lambda[(1-2\tau)u_N^2 - u_0^2]$ since $(\mathbf{S},\mathbf{u})_h = (\mathbf{u},\mathbf{S})_h = h\mathbf{u}^{\mathrm{T}}Hh^{-1}H^{-1}(0,0,...,0,1)^{\mathrm{T}} = u_N$. The discretization is time stable if $\tau \geq 1/2$.

4 Summary of selected papers

Paper 1

M. Larsson, B. Müller: Numerical simulation of confined pulsating jets in human phonation. Computers and Fluids 38 (2009), 1375–1383.

Using a fixed geometry, the flow field was calculated in a 2D domain representing the airways and the vocal folds. A time dependent flow velocity was imposed at the inlet and non-reflecting boundary conditions were applied at the outlet. The results displayed some similarities to other results published by other researchers but a quantitative comparison was not possible since their results were for axisymmetric flow.

Paper 2

M. Larsson, B. Müller: Numerical Simulation of Fluid-Structure Interaction in Human Phonation. MekIT '09: Fifth national conference on Computational Mechanics, Trondheim 26–27 May 2009, editors Bjørn Skallerud and Helge I. Andersson, Tapir Academic Press, 2009, 261–280.

The 2D compressible Navier–Stokes equations in ALE form were coupled to a structure solver to simulate fluid-structure interaction for the vocal folds. A neo-Hookean material model was used for the structure and a constant pressure difference was imposed across the glottis as driving force. The results captured the self-sustained oscillations of the glottis.

Paper 3

M. Larsson, B. Müller: Numerical Simulation of Fluid-Structure Interaction in Human Phonation: Application, Accepted for Proceedings of ENUMATH 2009 Eighth European Conference on Numerical Mathematics and Advanced Applications, Uppsala, Sweden, to be published by Springer 2010

Paper 3 is a subset of Paper 2. The focus is on the high order finite difference solution of the 2D compressible Navier–Stokes equations and results for the flow field.

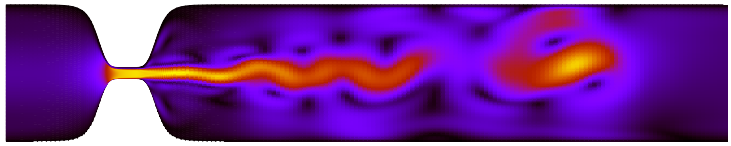

Figure 4: Typical result for fluid-structure interaction. The figure shows the absolute velocity of the velocity vector in the fluid domain.

Paper 4

M. Larsson, B. Müller: Numerical Simulation of Fluid-Structure Interaction in Human Phonation: Verification of Structure Part, Accepted for Proceedings of ICOSAHOM 09 International Conference on Spectral and High Order Methods, Trondheim, Norway, to be published as a special volume of the Lecture Notes in Computational Science and Engineering by Springer, 2010

Paper 4 focuses on the numerical boundary conditions for the structure equations. when using high order summation by parts operators. Simultaneous approximation terms are derived and tested for the 2D linear elastic wave equation.

Paper 5

M. Larsson, B. Müller: Strictly stable high order difference method for the linear elastic wave equation, submitted to CiCP, 2010.

The numerical solution of the linear elastic wave equation, is investigated with regard to boundary and initial conditions with the strictly stable SBP-SAT approach. The traction boundary condition is derived in the SAT framework. Numerical experiments showed that a near 4th order convergence rate can be obtained.

Paper 6

M. Larsson, B. Müller: High order numerical simulation of fluid-structure interaction in human phonation, Proceedings of ECCOMAS CFD 2010 conference, Lisbon, Portugal, 14–17 June 2010.

Paper 6 presents results for fluid-structure interaction with the 2D linear elastic wave equation coupled to the 2D compressible Navier–Stokes equations via the SAT method.

5 Conclusions and outlook

5.1 Conclusions

In this thesis, three different approaches based on ALE methods to 2D fluid-structure interaction have been investigated. In the first approach, the Lagrangian field equations for the nonlinear structure which are partial differential equations of second order in time are transformed to a first order system in time by the introduction of the velocity as an auxilliary variable and then integrated in time with a Runge–Kutta scheme. In this approach, the traction boundary condition can be imposed by enforcing a momentum flux on the fluid-structure boundary. In the spatial discretization, the momentum flux enters the finite-difference stencil at the boundary points. The finite-difference implementation was shown to converge to a reference solution provided by a commercial code but the advantage of a high order method was not evident.

In the second approach, the linear elastic wave equation written as a hyperbolic system in first order form is integrated in time with the Runge–Kutta scheme. Here, a SAT approach was derived and used as an alternative to injection to ensure strict stability of the method for general boundary conditions. A near fourth order convergence was demonstrated for a manufactured solution and an academic IBVP.

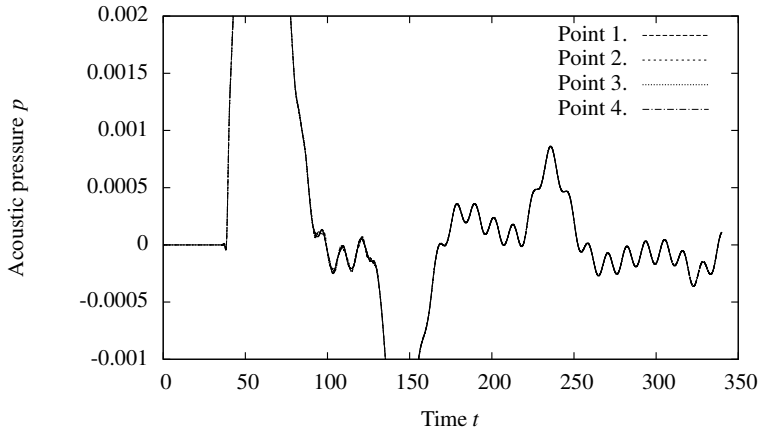

Figure 5: Acoustic pressure sampled at four equidistant points on a line perpendicular to the flow direction near the outflow at $x = 8H$ where H is the channel height, away from the glottis.

In the third approach, the previous method was extended to account for large deformations and nonlinear response of the structure. This was accomplished with the Lagrangian field equations as a starting point by transforming them to a form which reduces to the linear elastic wave equation when the deformations are small. The discretization is then done in the same way except that the coefficient matrices are here dependent upon the gradient of the displacement and the evolution equations for the stress components are nonconservative.

The compressible Navier–Stokes equations are discretized with a high-order finite difference scheme and coupled to the structure equations in a two-way explicit fluid-structure interaction algorithm. Simulations have been performed for the coupled system and results for vortex dynamics in the fluid domain (cf. Fig. 4) have been studied. Preliminary results for the acoustics in the vocal tract have been obtained (cf. Fig. 5).

5.2 Outlook

To move the project further, a handful of options are available. A more detailed study of acoustic data can be made to see the relation between the frequency spectrum of the sound waves in relation to model parameters. A rudimentary result for acoustic pressure data has been plotted in Figure 5. Here, the acoustic pressure $p' = p - p_\infty$ has been plotted as a function of time at four equidistant points on a line situated 8 cm downstream of the glottis, perpendicular to the flow direction. First, the acoustic pressure is zero because the acoustic signal has not yet reached the microphone points. Then a large peak occurs due to the start-up of the flow from zero initial conditions. After this peak, the acoustic pressure oscillates at an approximately constant frequency. There is little variation between the four points, implying that the sound waves travel as plane waves down the channel. The flow field has not yet reached these points and does therefore not interfere with the acoustic field.

Results for fluid-structure interaction with the nonlinear model remain to be published. A comparison between the linear and nonlinear models will show what role nonlinear material response plays in the coupled dynamics.

To make predictions about real phonation, it would be necessary to create a 3D model with a realistic geometry for the vocal folds. In addition, the collision that occurs in every oscillation cycle would need to be taken into account. Contact in particular is difficult to handle in the present model, not only because the coordinate transformation for the fluid domain breaks down when the cell volume goes to zero, but also because contact mechanics is in itself non-trivial and an active field of research. Immersed boundary methods are better suited for complex geometries. When the fluid is treated with an IB method, the collision of the vocal folds poses no problem. However, but a contact model is still needed.

References

[1] F. Alipour, D.A. Berry, and I.R. Titze. A finite-element model of vocal-fold vibration. *J. Acoust. Soc. Am.*, 108(6):3003 – 3012, 2000.

[2] F. Alipour and R.C. Scherer. Vocal fold bulging effects on phonation using a biophysical computer model. *J. Voice*, 14(4):470 – 483, 2000.

[3] F. Alipour and I.R. Titze. *Combined simulation of two-dimensional airflow and vocal fold vibration*. Ed. P. Davis and N. Fletcher, Singular Publishing Group, San Diego, 1996.

[4] F.P.T. Baaijens. A fictitious domain/mortar element method for fluid-structure interaction. *Int. J. Numer. Methods Fluids*, 35(7):743 – 761, 2001.

[5] D.A. Berry and I.R. Titze. Normal modes in a continuum model of vocal fold tissues. *J. Acoust. Soc. Am.*, 100:3345 – 3354, 1996.

[6] M. H. Carpenter, D. Gottlieb, and S. Abarbanel. Time-stable boundary conditions for finite-difference schemes solving hyperbolic systems: Methodology and application to high-order compact schemes. *J. Comp. Phys.*, 111:220 – 236, 1994.

[7] D.D. Cook and L. Mongeau. Sensitivity of a continuum vocal fold model to geometric parameters, constraints, and boundary conditions. *J. Acoust. Soc. Am.*, 121(4):2247 – 2253, 2007.

[8] C. A. Felippa, K. C. Park, and C. Farhat. Partitioned analysis of coupled mechanical systems. *Methods in Applied Mechanics and Engineering*, 190:3247 – 3270, 2001.

[9] J.B. Grotberg and O.E. Jensen. Biofluid mechanics in flexible tubes. *Annu. Rev. Fluid Mech*, 36:121 – 147, 2004.

[10] B. Gustafsson. *High order difference methods for time-dependent PDE*. Springer-Verlag Berlin Heidelberg, 2008.

[11] T.J.R. Hughes, W.K. Liu, and T.K. Zimmermann. Lagrangian-Eulerian finite element formulation in incompressible viscous flows. *Comput. Methods Appl. Mech. Engrg.*, 29:329 – 349, 1981.

[12] C.K. Kleinstreuer. *Biofluid Dynamics, Principles and Selected Applications*. CRC Press, Taylor and Francis Group, 2006.

[13] S. G. Lekhnitskii. *Theory of Elasticity of an Anisotropic Elastic Body*. Holden-Day, San Francisco, 1963.

[14] G. Link, M. Kaltenbacher, M. Breuer, and M. Döllinger. A 2d finite-element scheme for fluid-solid-acoustic interactions and its application to human phonation. *Methods in Applied Mechanics and Engineering*, 198:3321 – 3334, 2009.

[15] H. Luo, R. Mittal, X. Zheng, S.A. Bielamowicz, R.J. Walsh, and J.K. Hahn. An immersed-boundary method for flow - structure interaction in biological systems with application to phonation. *J. Comput. Phys.*, 227:9303 – 9332, 2008.

[16] R. Mittal and G. Iaccarino. Immersed boundary methods. *Annu. Rev. Fluid Mech.*, 37:239 – 261, 2005.

[17] B. Müller. Computation of compressible low Mach number flow, Habilitation Thesis, ETH Zürich, 1996.

[18] R.W. Ogden. *Non-linear elastic deformations*. Ellis Horwood Limited, 1984.

[19] C.S. Peskin. Numerical analysis of blood flow in the heart. *J. Comput. Phys.*, 25:220 – 252, 1977.

[20] H. Viviand R. Peyret. Computation of viscous compressible flows based on the Navier–Stokes equations. *AGARD–AG–***212**, 1975.

[21] P. Šidlof, J. G. Švec, J. Horáček, J. Veselý, I. Klepáček, and R. Havlík. Geometry of human vocal folds and glottal channel for mathematical and biomechanical modeling of voice production. *Journal of Biomechanics*, 41:985 – 995, 2008.

[22] M. Souli, A. Ouahsine, and L. Lewin. ALE formulation for fluid-structure interaction problems. *Comput. Methods Appl. Mech. Engrg.*, 190:659 – 675, 2000.

[23] B.H. Story and I.R. Titze. Voice simulation with a body-cover model of the vocal folds. *J. Acoust. Soc. Am.*, 97:1249 – 1260, 1995.

[24] B. Strand. Summation by parts for finite difference approximations for d/dx. *J. Comput. Phys.*, 110:47 – 67, 1994.

[25] J.C. Tannehill, D. A. Anderson, and R. H. Pletcher. *Computational fluid mechanics and heat transfer, Second Edition*. Taylor & Francis, Philadelphia, 1997.

[26] S.L. Thomson. *Fluid-structure interactions within the human larynx*. PhD thesis, Purdue University, 2004.

[27] I. R. Titze. The human instrument. *Scientific American*, January, 2008.

[28] I.R. Titze. *Principles of voice production*. National Center for Voice and Speech, 2000.

[29] R.J. Zwaan and B.B. Prananta. Fluid/structure interaction in numerical aeroelastic simulation. *Int. J. Non-Linear Mech.*, 37:987 – 1002, 2002.

PAPER 1

M. Larsson, B. Müller: Numerical simulation of confined pulsating jets in human phonation. *Computers and Fluids* **38** (2009), 1375–1383.

Computers & Fluids 38 (2009) 1375–1383

Contents lists available at ScienceDirect

Computers & Fluids

journal homepage: www.elsevier.com/locate/compfluid

Numerical simulation of confined pulsating jets in human phonation

Martin Larsson, Bernhard Müller *

Department of Energy and Process Engineering, Norwegian University of Science and Technology (NTNU), Kolbjørn Hejes vei 2, NO-7491 Trondheim, Norway

ARTICLE INFO

Article history:
Received 10 March 2007
Accepted 23 January 2008
Available online 22 April 2008

ABSTRACT

Confined pulsating jets in simplified two-dimensional models of the larynx are considered to study human phonation. The jets are generated by periodically oscillating inlet velocities in stationary vocal tracts. The jets are computed by solving the 2D compressible Navier–Stokes equations by a high order finite difference method, which has been constructed to be strictly stable for linear hyperbolic and parabolic problems. Vortex dynamics is investigated.

1. Introduction

When we speak or sing, an intermittent air flow through the vocal folds from the trachea into the vocal tract is generated, giving rise to audible sound [1,2]. The pressure of the respiration air forced up the trachea from the lungs will eventually be high enough to open the glottis, pushing the vocal folds apart and forming a starting jet. As air passes through the glottis, the pressure in the glottis decreases. Because of the drop in pressure and due to elastic forces, the vocal folds will close again. The cycle then begins again and a pulsating jet into the air column of the vocal tract is formed. The acoustic waves from this pulsating jet are the main source for human phonation. The various temporal features of the glottal pressure waveform are the prerequisites for how the voice will be perceived by the human ear.

The vocal folds take on three basic shapes during this cycle: converging, uniform and diverging, cf. Fig. 1. The vocal fold tissue can be thought of as a ribbon with multiple normal modes of oscillation where the two sides of the ribbon do not move in phase. The three different glottal shapes are then obtained at different phases of the cycle.

Other sources of sound are turbulence in the glottal airstream, vortex shedding from the moving walls, the interaction of the jet vortices with the ventricular folds and transient sounds produced by sudden onset and offset of phonation.

Recently, numerical simulations of phonation based on the compressible Navier–Stokes equations have been performed [3–5]. Like in direct numerical simulation, high order discretization methods have been preferred for the numerical solution of the compressible Navier–Stokes equations in aeroacoustics, because higher order methods are more efficient for high accuracy requirements than low order methods.

We employ a high order finite difference approach based on summation by parts (SBP) operators [6,7] to solve the compressible Navier–Stokes equations. Opposed to conventional difference approximations, our high order finite difference methods have the advantage of being constructed to be strictly stable for linear hyperbolic and parabolic problems even for non-periodic boundary conditions. The sixth order SBP operator [7], which is third order accurate near the boundaries, is employed to discretize the first derivatives in the 2D compressible Navier–Stokes equations. The operator has previously been used to simulate aeolian tones [8]. The Navier–Stokes equations in conservative form are expressed in perturbation form [9,10,8] to minimize rounding errors caused by cancellation in low Mach number flow computations. Another high order approach relying on residual-based compact schemes has recently been proposed by Lerat and Corre [11,12].

We consider the simplified models of vocal tracts with diverging and converging orifices, i.e. glottises, and similar pulsating inflow conditions as investigated by Zhao et al. [3]. However, instead of axisymmetric flow studied in [3], we simulate 2D flow. That allows us to investigate the differences between axisymmetric and 2D flow and to study flow asymmetries due to the Coanda effect.

The governing equations, i.e. the 2D and axisymmetric compressible Navier–Stokes equations, are presented in perturbation form for coordinate transformations in Section 2. The high order finite difference method is outlined in Section 3. In Section 4, results for numerical simulations of confined pulsating jets are discussed for $Re = 3000$, $M = 0.2$, $Pr = 1$. Conclusions are stated in Section 5.

2. Navier–Stokes equations in perturbation form

The perturbation formulation is used to minimize cancellation errors when discretizing the Navier–Stokes equations for compressible low Mach number flow [9,8]. The 2D and axisymmetric compressible Navier–Stokes equations in conservative form can be expressed in perturbation form as [10]

* Corresponding author.
E-mail address: Bernhard.Muller@ntnu.no (B. Müller).

0045-7930/$ - see front matter © 2008 Elsevier Ltd. All rights reserved.
doi:10.1016/j.compfluid.2008.01.033

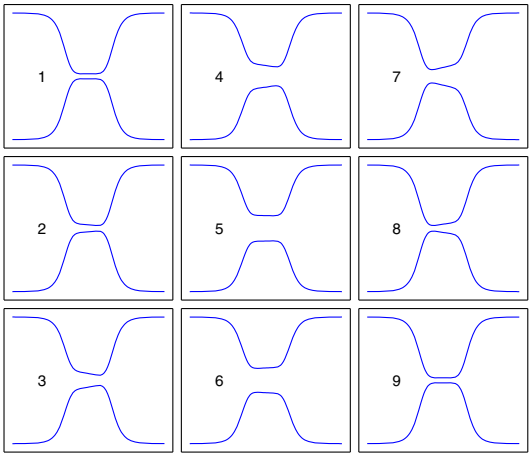

Fig. 1. Characteristic variation of glottis cross-section: 1 & 9 closed, 2 opening, 3 & 4 converging, 5 uniform, 6 & 7 diverging, 8 closing. The air flows from the trachea on the left into the vocal tract on the right.

$$\mathbf{U}'_t + \mathbf{F}^{c'}_x + \mathbf{G}^{c'}_y + \ell\mathbf{H}^{c'} = \mathbf{F}^{v'}_x + \mathbf{G}^{v'}_y + \ell\mathbf{H}^{v'}, \tag{1}$$

where $\ell = 0$ for 2D flow and $\ell = 1$ for axisymmetric flow. The vector $\mathbf{U}'$ denotes the perturbation of the conservative variables with respect to the stagnation values. $\mathbf{U}'$ and the inviscid (superscript c) and viscous (superscript v) flux vectors and axisymmetric source terms are defined by

$$\mathbf{U}' = \begin{pmatrix} \rho' \\ (\rho u)' \\ (\rho v)' \\ (\rho E)' \end{pmatrix}, \quad \mathbf{F}^{c'} = \begin{pmatrix} (\rho u)' \\ (\rho u)'u' + p' \\ (\rho v)'u' \\ (\rho_0 H_0 + (\rho H)')u' \end{pmatrix},$$

$$\mathbf{G}^{c'} = \begin{pmatrix} (\rho v)' \\ (\rho u)'v' \\ (\rho v)'v' + p' \\ (\rho_0 H_0 + (\rho H)')v' \end{pmatrix},$$

$$\mathbf{F}^{v'} = \begin{pmatrix} 0 \\ \tau'_{xx} \\ \tau'_{xy} \\ \tau'_{xx}u' + \tau'_{xy}v' + \kappa T'_x \end{pmatrix}, \quad \mathbf{G}^{v'} = \begin{pmatrix} 0 \\ \tau'_{yx} \\ \tau'_{yy} \\ \tau'_{yx}u' + \tau'_{yy}v' + \kappa T'_y \end{pmatrix},$$

$$\mathbf{H}^{c'} = \frac{1}{y}\begin{pmatrix} (\rho v)' \\ (\rho u)'v' \\ (\rho v)'v' \\ (\rho_0 H_0 + (\rho H)')v' \end{pmatrix}, \quad \mathbf{H}^{v'} = \frac{1}{y}\begin{pmatrix} 0 \\ \tau'_{yx} \\ \tau'_{yy} - \tau'_{\theta\theta} \\ \tau'_{yx}u' + \tau'_{yy}v' + \kappa T'_y \end{pmatrix}.$$

The subscripts in (1) subsequently denote derivatives. We assume perfect gas. The perturbation variables (superscript $'$) are defined with respect to their stagnation values (subscript 0), i.e. $\rho' = \rho - \rho_0$, $(\rho\mathbf{u})' = \rho\mathbf{u}$, $(\rho E)' = \rho E - (\rho E)_0$, $(\rho H)' = (\rho E)' + p'$, $\mathbf{u}' = \frac{(\rho\mathbf{u})'}{\rho_0+\rho'}$, $p' = (\gamma-1)[(\rho E)' - \frac{1}{2}((\rho\mathbf{u})'\cdot\mathbf{u}')]$, $\boldsymbol{\tau}' = \mu(\nabla\mathbf{u}' + (\nabla\mathbf{u}')^{\mathrm{T}}) - \frac{2}{3}\mu\left(\nabla\cdot\mathbf{u}' + \ell\frac{v'}{y}\right)\mathbf{I}$, $\tau'_{\theta\theta} = -\frac{2}{3}\mu(u'_x + v'_y) + \frac{4}{3}\frac{v'}{y}$, $T' = \frac{p'/R - \rho' T_0}{\rho_0+\rho'}$.

t is time, and x and y are the Cartesian coordinates. ρ denotes the density, u and v the x- and y-direction velocities, E the specific total energy, p the pressure, $\gamma = 1.4$ the ratio of specific heats for air, R the specific gas constant, μ viscosity determined from the Sutherland law $\frac{\mu}{\mu_0} = (\frac{T}{T_0})^{1.5}\frac{1+S_c}{\frac{T}{T_0}+S_c}$ with the nondimensional Sutherland constant $S_c = \frac{110}{301.75}$, κ the heat conduction coefficient determined from the constant Prandtl number $Pr = 1$. ρ_0, $(\rho E)_0$ and $(\rho H)_0$ denote the stagnation quantities of density, total energy density and total enthalpy density, respectively. The viscous flux vectors $\mathbf{F}^{v'}$ and $\mathbf{G}^{v'}$ are the same as for the standard conservative form, except for using the temperature perturbation T' instead of temperature T for the heat flux terms. The momentum density and velocity perturbations are taken as the same as their unperturbed counterparts, i.e. $(\rho\mathbf{u})' = \rho\mathbf{u}$ and $\mathbf{u}' = \mathbf{u}$, cf. the definition of $\mathbf{U}'$ with respect to $\mathbf{U}_0 = (\rho_0, 0, 0, (\rho E)_0)^{\mathrm{T}}$ above. The 2D conservative compressible Navier–Stokes equations in perturbation form (1) are written in dimensional form, while their nondimensional form with ρ_0, stagnation speed of sound c_0, and $\rho_0 c_0^2$ as reference values of density, velocity, and pressure, respectively, has actually been used in the computations.

General geometries are treated by a coordinate transformation $x = x(\xi,\eta)$, $y = y(\xi,\eta)$. The transformed 2D conservative compressible Navier–Stokes equations in perturbation form read

$$\widehat{\mathbf{U}}'_t + \widehat{\mathbf{F}}'_\xi + \widehat{\mathbf{G}}'_\eta + \ell\widehat{\mathbf{H}}' = 0, \tag{2}$$

where $\widehat{\mathbf{U}}' = J^{-1}\mathbf{U}'$, $\widehat{\mathbf{F}}' = J^{-1}\xi_x(\mathbf{F}^{c'} - \mathbf{F}^{v'}) + J^{-1}\xi_y(\mathbf{G}^{c'} - \mathbf{G}^{v'})$, $\widehat{\mathbf{G}}' = J^{-1}\eta_x(\mathbf{F}^{c'} - \mathbf{F}^{v'}) + J^{-1}\eta_y(\mathbf{G}^{c'} - \mathbf{G}^{v'})$, $\widehat{\mathbf{H}}' = J^{-1}(\mathbf{H}^{c'} - \mathbf{H}^{v'})$.

The x- and y-derivatives in the viscous flux vectors $\mathbf{F}^{v'}$ and $\mathbf{G}^{v'}$ are expressed using the chain rule, e.g. $u'_x = u'_\xi\xi_x + u'_\eta\eta_x$ and $u'_y = u'_\xi\xi_y + u'_\eta\eta_y$. The Jacobian determinant of the transformation J is determined by $J^{-1} = x_\xi y_\eta - x_\eta y_\xi$, and the metric terms by $J^{-1}\xi_x = y_\eta$, $J^{-1}\xi_y = -x_\eta$, $J^{-1}\eta_x = -y_\xi$, $J^{-1}\eta_y = x_\xi$.

3. High order finite difference method

3.1. Summation by Parts (SBP) Operators

Let $v_j, j = 0,\ldots N$, be an approximation to the exact solution $u(x_j)$ at the grid point $x_j = jh$, where $h = 1/N$. The discrete scalar product and norm are [7]

$$(u,v)_h = hu^{\mathrm{T}}Hv, \quad \|u\|_h^2 = (u,u)_h, \tag{3}$$

where the norm matrix H is diagonal and positive definite.

The *summation by parts* (SBP) property, analogous to integration by parts in the continuous case, is satisfied, if [7]

$$(u,Qv)_h = u_N v_N - u_0 v_0 - (Qu,v)_h \tag{4}$$

for a difference operator Q. Let

$$hQ = H^{-1}B. \tag{5}$$

The SBP property can be rewritten

$$hu^{\mathrm{T}}HQv = u^{\mathrm{T}}\mathrm{diag}(-1,0,\ldots,0,1)v - h(Qu)^{\mathrm{T}}Hv \tag{6}$$

and rearranged to

$$hu^{\mathrm{T}}(HQ + Q^{\mathrm{T}}H)v = u^{\mathrm{T}}\mathrm{diag}(-1,0,\ldots,0,1)v. \tag{7}$$

Now, H was diagonal by definition so $H = H^{\mathrm{T}}$, hence

$$u^{\mathrm{T}}(HhQ + (HhQ)^{\mathrm{T}})v = u^{\mathrm{T}}\mathrm{diag}(-1,0,\ldots,0,1)v. \tag{8}$$

Using (5) and the fact that u and v are arbitrary, we get

$$B + B^{\mathrm{T}} = \mathrm{diag}(-1,0,\ldots,0,1). \tag{9}$$

This defines B under the assumption (5). The difference operator Q is an approximation to the first derivative, i.e. $(Qv)_j \approx \frac{du(x_j)}{dx}$. If Q is accurate of order 2τ in the interior, then there is a diagonal norm matrix H, such that Q is accurate of order τ near the boundaries [7]. When $\tau = 3$ which is the case considered here, there is a one-parameter family of operators Q. One of the elements in the matrix of Q can be set to zero in such a way that the bandwidth of the

matrix is minimized to obtain a unique matrix Q which yields a sixth order accurate operator in the interior. Thus, the global order of accuracy of the present SBP operator Q is $\tau + 1 = 4$ [6].

Second derivatives are approximated by applying the SBP operator Q twice. Alternative discretizations of second derivatives [13,14] are discussed in [8]. Opposed to conventional difference operators, SBP operators allow energy estimates for the discrete problems similar to the ones for the continuous problems, which are approximated. Thus, SBP operators yield strictly stable schemes for general boundary conditions.

If the x-derivative in the convection diffusion equation $u_t + au_x = bu_{xx}$, where a and b are assumed to be constant and $b > 0$, is approximated by a standard central pth order finite difference operator $Q_x^{(p)}$ and the time derivative by an explicit Runge–Kutta method, the von Neumann stability analysis leads to the stability condition $\Delta t(-a\widehat{Q}^{(p)} + b(\widehat{Q}^{(p)})^2) \in S$, where $\widehat{Q}^{(p)}$ is the Fourier transform of $Q_x^{(p)}$ and S the stability domain of the Runge–Kutta method. $\widehat{Q}^{(p)}\frac{\Delta x}{i}$ is the approximate wave number $\tilde{k}\Delta x$. For SBP operators, the stability condition is more restrictive, because $\Delta t\| - aQ_x^{(p)} + b(Q_x^{(p)})^2\| \leqslant R < R_1$ is required, where the open semicircle $\{z \in \mathbb{C} || z| < R_1 \text{ and } \mathrm{Real}(z) < 0\}$ is contained in the stability domain S [15]. In practical computations, however, it has been possible to use von Neumann stability condition with a safety margin. The von Neumann stability condition for the standard central sixth order difference operator $Q_x^{(6)}$ and the classical fourth order explicit Runge–Kutta method reads $\mathrm{CFL} = \frac{|a|\Delta t}{\Delta x} \leqslant 1.783$ for $b = 0$ and $\mathrm{VNN} = \frac{|b|\Delta t}{\Delta x^2} \leqslant 1.124$ for $a = 0$, while $\mathrm{CFL} \leqslant 2.828$ for $b = 0$ and $\mathrm{VNN} \leqslant 2.828$ for $a = 0$ is required for the standard central second order operator $Q_x^{(2)}$. Note that $(Q_x^{(6)}\mathbf{u})_j = \frac{1}{\Delta x}\left(\frac{1}{60}u_{j+3} - \frac{3}{20}u_{j+2} + \frac{3}{4}u_{j+1} - \frac{3}{4}u_{j-1} + \frac{3}{20}u_{j-2} - \frac{1}{60}u_{j-3}\right)$ and $\widehat{Q}^{(6)} = \frac{i}{\Delta x}\left[\frac{3}{2}\sin(k\Delta x) - \frac{3}{10}\sin(2k\Delta x) + \frac{1}{30}\sin(3k\Delta x)\right]$, where k is the wave number in this subsection.

3.2. Approach for Navier–Stokes equations

The transformed 2D compressible Navier–Stokes equations in perturbation form (2) are solved on a rectangle, where $\xi = 1$ and $\xi = j_{\max}$ represent the inlet and outlet boundaries of the vocal tract, respectively, and $\eta = 1$ and $\eta = k_{\max}$ correspond to the lower and upper walls of the vocal tract, respectively. The ξ- and η-derivatives in the metric terms are discretized by Strand's 3–6 SBP operator [7]. The viscous flux vectors are discretized by approximating the first ξ and η derivatives of u', v' and T', by Strand's 3–6 SBP operator. After the flux vectors $\widehat{\mathbf{F}}'$ and $\widehat{\mathbf{G}}'$ are computed at all grid points, $\widehat{\mathbf{F}}'_\xi$ and $\widehat{\mathbf{G}}'_\eta$ are approximated by employing Strand's 3–6 SBP operator once more.

The classical fourth order explicit Runge–Kutta method is used for time integration. Spurious high wave number oscillations are suppressed by a sixth order explicit filter [8].

3.3. Boundary conditions

No-slip adiabatic wall boundary conditions ($u_w = v_w = 0$, $\frac{\partial T_w}{\partial n} = 0$) and the Navier–Stokes Characteristic Boundary Conditions (NSCBC) technique by Poinsot and Lele in [16] are employed. The amplitudes of the characteristic waves.

$$\mathscr{L}_1 = \lambda_1\left(\frac{\partial p}{\partial x} - \rho c\frac{\partial u}{\partial x}\right), \quad \mathscr{L}_2 = \lambda_2\left(c^2\frac{\partial \rho}{\partial x} - \frac{\partial p}{\partial x}\right), \quad \mathscr{L}_3 = \lambda_3\frac{\partial v}{\partial x},$$
$$\mathscr{L}_4 = \lambda_4\left(\frac{\partial p}{\partial x} + \rho c\frac{\partial u}{\partial x}\right)$$

are prescribed for ingoing waves. Non-reflecting boundary conditions can be obtained by setting the ingoing waves to zero. Thus, for reverse flow at the outlet, we set $\mathscr{L}_1 = \mathscr{L}_2 = \mathscr{L}_3 = 0$.

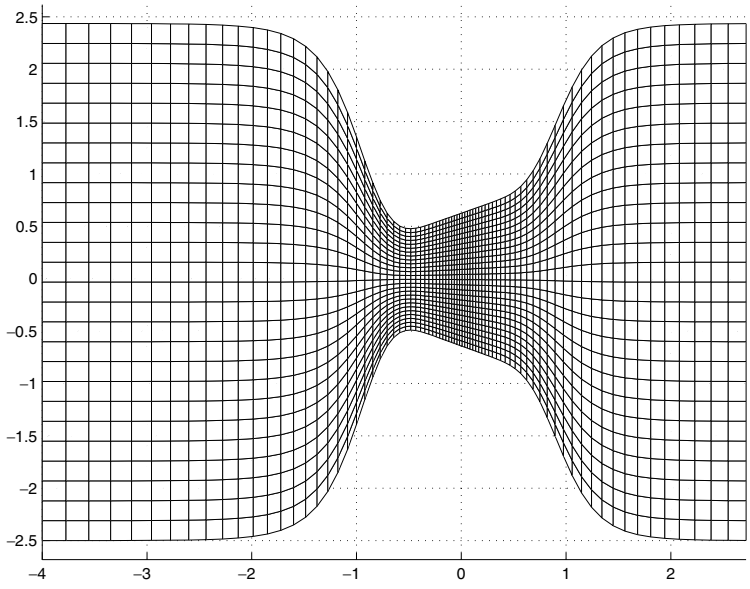

Fig. 2. Close-up of grid near the glottis region (not all points shown for clarity)

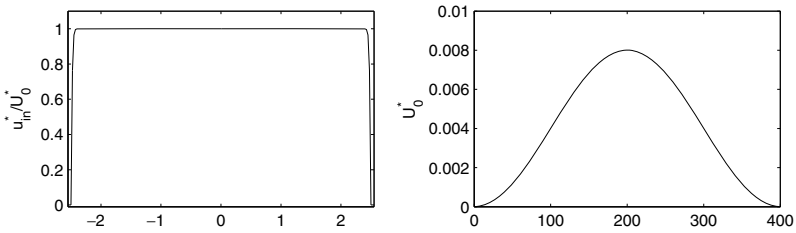

Fig. 3. Velocity profile at inflow boundary (left) and nondimensional forcing function for the first period (right).

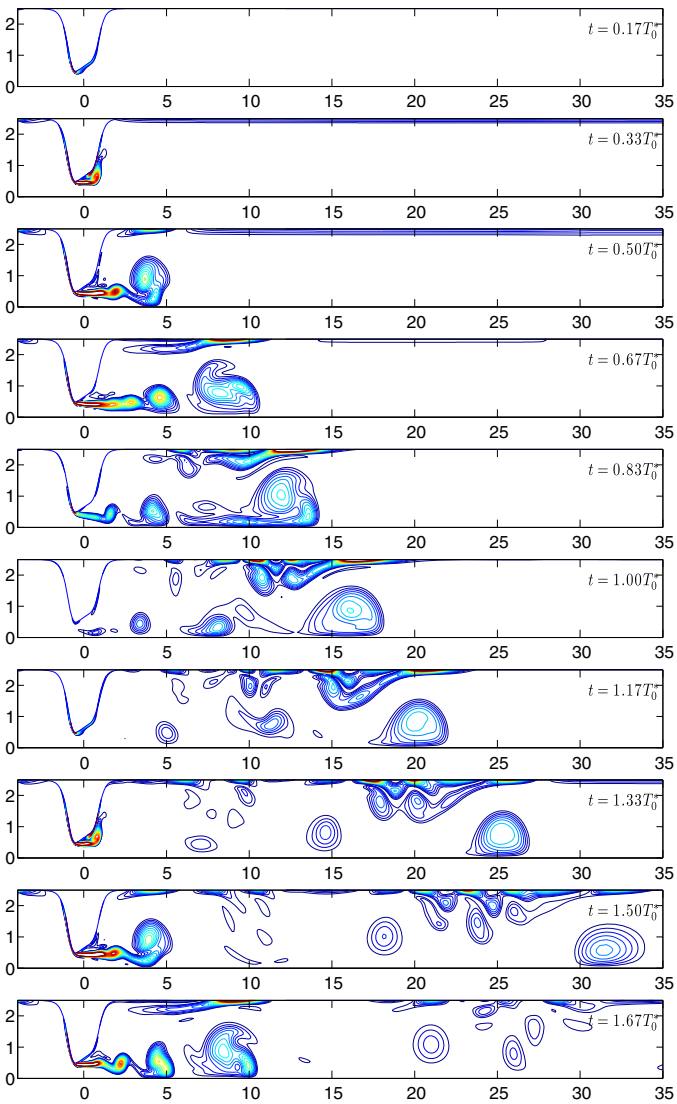

Fig. 4. Vorticity contours for diverging orifice. Min = 0.1, Max = 1.0, Number of contour levels = 20. Top to bottom: $t^* = \frac{1}{6}T^*_0, \frac{2}{6}T^*_0, \ldots, \frac{10}{6}T^*_0$.

4. Results for confined pulsating 2D jets

4.1. Grid

We consider a simplified model of the vocal tract without ventricular folds as proposed by Zhao et al. [3]. The shape of the geometry [3] is defined by

$$r_w(x) = \frac{D_0 - D_g}{4}\tanh(s) + \frac{D_0 + D_g}{4} + \frac{1}{2}\tan(\alpha)(x + cD_g)(1 - \tanh(s)), \tag{10}$$

where D_g is the minimum orifice diameter, $D_0 = 5D_g$ is the diameter of the uniform duct, $b = 1.4$ is a constant and $\alpha = \pm 20^\circ$ is the angle of the orifice. The parameter c and the angle α are chosen as $c = -0.39$ and $\alpha = -20^\circ$ for the converging orifice and $c = 0.39$ and $\alpha = 20^\circ$ for the diverging orifice. The symmetric function $s = s(x)$ reads

$$s = \frac{b|x|}{D_g} - \frac{bD_g}{|x|}. \tag{11}$$

As $x \to 0$, $s \to -\infty$ so $\tanh(s) \to -1$ and as $x \to \infty$, $s \to \infty$ so $\tanh(s) \to 1$.

The spacing of the grid points was chosen such that the resolution is best in the region near the glottis where the flow is expected to have the most complex structures. A close-up of the grid near the glottis region is shown in Fig. 2.

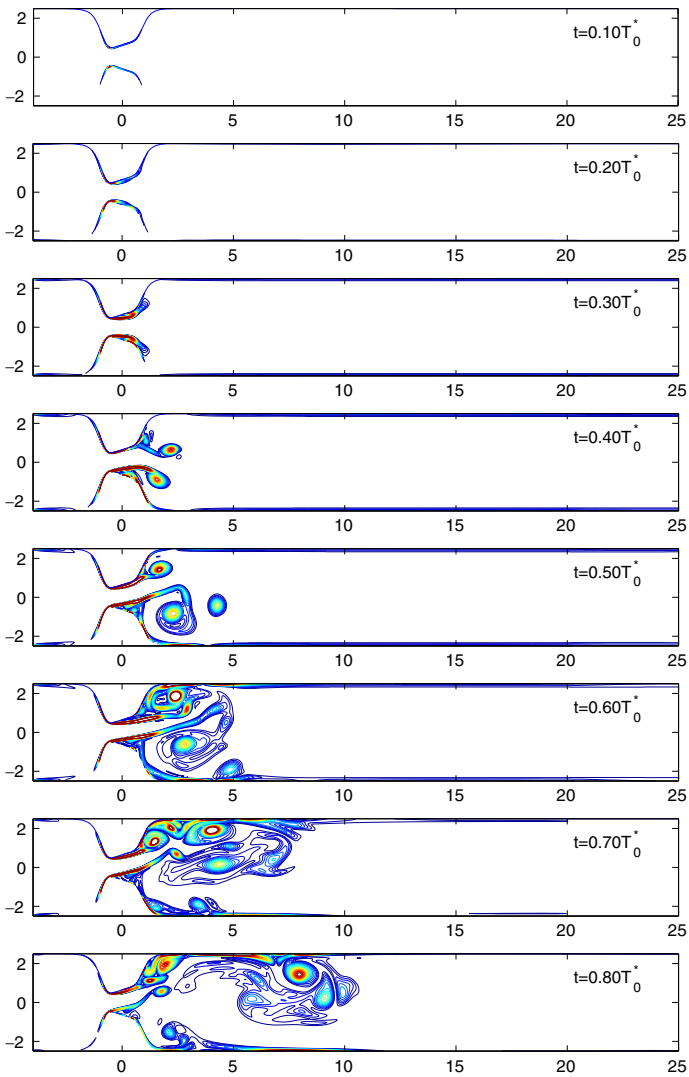

Fig. 5. Vorticity contours for diverging orifice with imposed asymmetry. Min = 0.1, Max = 1.0, Number of contour levels = 20. Top to bottom: $t^* = \frac{1}{10}T_0^*, \frac{2}{10}T_0^*, \ldots, \frac{8}{10}T_0^*$.

4.2. Inflow conditions

At the inflow, the velocity in the x-direction is specified similarly to Zhao et al. [3] by

$$u_{\text{in}}(y,t) = U_0(t)\tanh[40(D_0/2 - |y|)/D_g], \tag{12}$$

which is an almost uniform profile but zero at the boundaries $y = \pm D_0/2$. $D_g = 4$ mm is the minimum orifice diameter and $D_0 = 5D_g$ is the duct diameter. The time-varying maximum $U_0(t)$ is given by Zhao et al. [3]

$$U_0(t) = 0.02004U_M - 0.02U_M\cos(2\pi f_0 t), \tag{13}$$

where $U_M = 40$ m/s is the maximum expected velocity at the throat and $f_0 = 125$ l/s is the forcing frequency.

Dimensionless quantities for length, velocity and time are defined with respect to D_g, the stagnation speed of sound c_0 and D_g/c_0, respectively, hence

$$x^* = \frac{x}{D_g}, \quad y^* = \frac{y}{D_g}, \quad u^* = \frac{u}{c_0}, \quad v^* = \frac{v}{c_0}, \quad t^* = \frac{c_0 t}{D_g}. \tag{14}$$

The stagnation speed of sound was artificially changed from 340 m/s to $c_0 = 200$ m/s in this study to increase the computational efficiency. Thus, the maximum expected velocity corresponds to the Mach number $M = 0.2$ as in [3]. For subsonic flows at low Mach numbers, this change is expected to have negligible effect [3].

The dimensionless forcing period is $T_0^* = 1/f_0^* = c_0/D_g f_0 = 400$. The time-independent velocity profile $u_{\text{in}}^*(y^*,t^*)/U_0^*(t^*)$ and the time-dependent forcing function $U_0^*(t^*)$ are shown in Fig. 3.

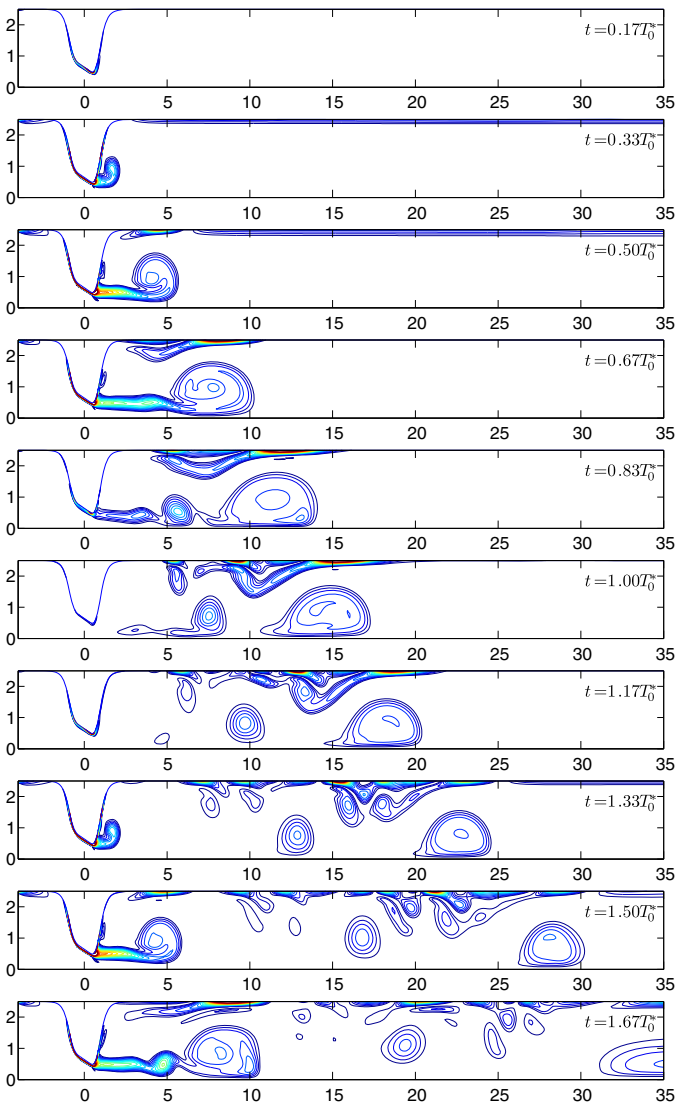

Fig. 6. Vorticity contours for converging orifice. Min = 0.1, Max = 1.0, Number of contour levels = 20. Top to bottom: $t^* = \frac{1}{6}T_0, \frac{2}{6}T_0, \ldots, \frac{10}{6}T_0$.

The parameters 0.02004 and 0.02 in (13) are those given by Zhao et al. [3] for an axisymmetric jet, and they are chosen to get a maximum velocity of $U_M = 40$ m/s in the orifice. For the 2D simulations here (not considered by Zhao et al. [3]), these parameters were changed so that the maximum velocity in the orifice would be U_M also for the 2D case. The velocity in a duct will in general be smaller for the 2D case than in the axisymmetric case because the cross-section area scales as y^2 for the axisymmetric case but only as y for the 2D case. Comparison with the velocity profile (Figure 4 in [3]) has led to the following nondimensional forcing function for the 2D case

$$U^*_{0,2D}(t^*) = \frac{40}{200}[0.0835 - 0.0833\cos(2\pi t^*/400)]. \quad (15)$$

The Reynolds number based on U_M and D_g was set to $Re = 3000$ as in [3] in order to be able to compare results.

The Prandtl number was set to $Pr = 1.0$ as in [3]. More details may be found in [17].

4.3. Diverging geometry

For the diverging geometry, α is set to $+20^\circ$ in (10). The computational domain was set to reach from -4 to 35 in the x-direction and -2.5 to 2.5 in the y-direction.

The grid was generated with 361×121 points. The minimum x-spacing in the middle of the orifice was 0.0325 and the maximum x-spacing at the end of the domain was 0.7146. The uniform y-spacing in the middle of the glottis was 0.0082 and increased to 0.0417 at the end of the domain. An exit zone was used at the end of the domain.

The solution was marched from time $t^* = 0$ with zero initial conditions for $\mathbf{U}'$ to $t^* = 8T^*_0/3$ where T^*_0 is the forcing period of the pulsating inflow. A variable time step technique was employed so that the CFL number remained a constant equal to 1 during the entire simulation. The maximum time step based on this CFL criterion was 0.00539.

Results for the vorticity[1] (z-component) are shown in Fig. 4. Only the top half of the domain is shown. The solution is symmetric w.r.t. the x-axis. The nondimensional vorticity is

$$(\nabla^* \times \mathbf{u}^*)_z = \frac{\partial v^*}{\partial x^*} - \frac{\partial u^*}{\partial y^*}. \quad (16)$$

A leading vortex is shed from the orifice at approximately $t^* = T^*_0/3$. It is convected downstream and grows in size as the absolute value of vorticity is successively decreased in the center of the vortex. It leaves a trail of vorticity and two new vortices are created inside the trail at approximately $t^* = 4T^*_0/6$. A smaller fourth vortex is shed at $t^* = 5T^*_0/6$.

The process then repeats itself. A new vortex is shed one period of time after the first leading vortex left the orifice, and the contours at later times are indeed very similar to the corresponding contours at times one period earlier. This suggests that the influence of initial data is small.

The leading vortex is convected out of the domain but the smaller ones get dissipated and only leave weak trails.

A profile of the velocity in the x-direction u through the center vortex at position $x^* = 0.799$ and time $t^* = T^*_0/3$ is shown in Fig. 7.

4.4. Coanda effect

Experimental investigations of the vortex dynamics in a mechanical model of the vocal folds suggest asymmetries in the jets [18]. Thus, for the diverging orifice, a study of asymmetries in the flow was conducted. Instead of an adiabatic wall, the isothermal boundary condition $T_w = T_0$ was used in this study. The asymmetry was imposed by changing the no-slip boundary condition at the wall to one where a nonzero tangential velocity is given on the boundary for a short period of time.

A grid with 481×161 points was selected for a geometry extending from -4 to 25 in the x-direction and from -2.5 to 2.5 in the y-direction. An exit zone at the outflow was introduced. The minimum x-spacing in the middle of the orifice was 0.0136, the uniform x-spacing between the orifice and the exit zone was 0.073 and the maximum x-spacing at the end of the exit zone was 0.386. The uniform y-spacing was 0.0061 in the orifice and 0.0312 near the outflow. The asymmetry was imposed between times $t^* = 0.30T^*_0$ to $t^* = 0.45T^*_0$ by gradually increasing and then decreasing the tangential velocity at the upper boundary between $x^* = -1$ and $x^* = 1$, reaching a maximum value of 0.2 which corresponds to the maximum Mach number of the flow.

Fig. 5 shows results for the vorticity contours at times $t^* = 0.1T^*_0, 0.2T^*_0, \ldots, 0.8T^*_0$. The leading vortex starts to be shed at approximately $t^* = 0.30T^*_0$ and then the asymmetry starts to build up. Even after the asymmetry has been turned off, the flow stays very asymmetric, suggesting that only a small perturbation is required for the flow to remain asymmetric at later times.

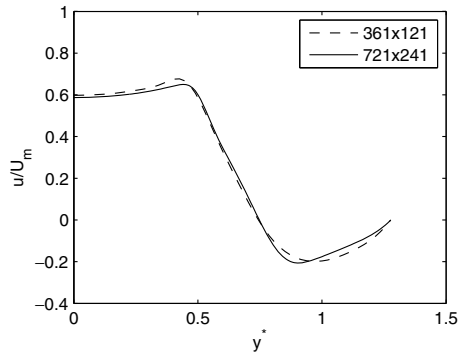

Fig. 7. Velocity profiles through the center of the leading vortex at $x^* = 0.799$ for the diverging orifice.

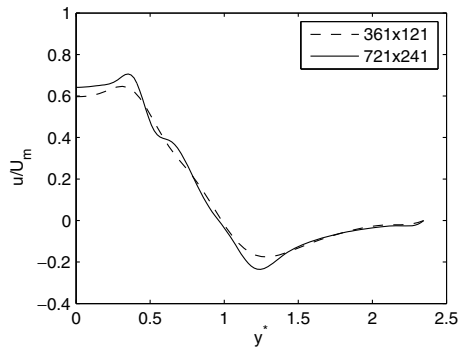

Fig. 8. Velocity profiles through the center of the leading vortex at $x^* = 1.593$ for the converging orifice.

[1] In all contour plots here, the horizontal axis is x and the vertical axis is y.

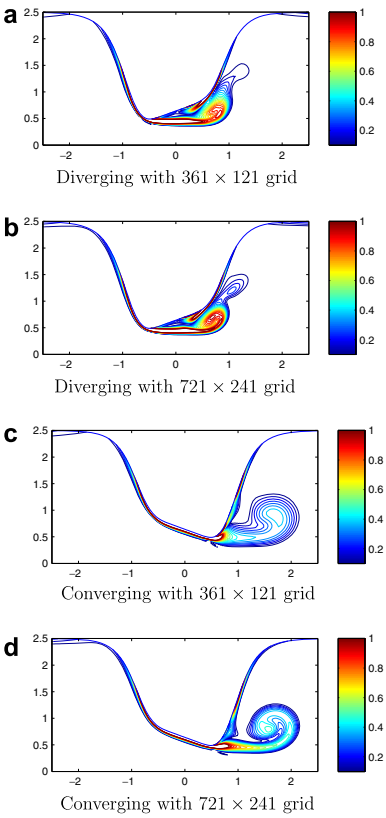

Fig. 9. Close-up of vorticity contours for converging and diverging orifice at $t^* = T_0^*/3$. (a) Diverging with 361 × 121 grid. (b) Diverging with 721 × 241 grid. (c) Converging with 361 × 121 grid. (d) Converging with 721 × 241 grid.

4.5. Converging geometry

The parameters α and c in (10) were set to -20° and -0.39, respectively, and a simulation was set up with otherwise the same conditions as for the diverging case.

Results for the vorticity contours are shown in Fig. 6.

A few differences and similarities as compared to the diverging case can be pointed out. The leading vortex is created at the same time and convected in the same way. But only one additional vortex is created within its trail during the first period. The absolute value of vorticity in the leading vortex is smaller than that in the diverging case. Also in this case, the process repeats itself after one period, and the effect of initial data is small.

A profile of the velocity in the x-direction u through the center vortex at position $x^* = 1.593$ and time $t^* = T_0^*/3$ is shown in Fig. 8.

The reason for the leading vortices in the two cases to be at different locations is that the shedding point is not the same. Assuming that shedding occurs at some critical velocity, the vortex in the converging case will have a head start as the shedding point is further to the right.

4.6. Verification

For the converging orifice, a comparison with Figure 6 in [3] can be made. Whereas their dimensionless velocity is defined w.r.t. the maximum expected velocity in the orifice U_M, the velocities in this study are nondimensionalized w.r.t. the stagnation speed of sound c_0. Thus, the nondimensional velocity and vorticity in [3] are a factor of $c_0/U_M = 5$ larger than ours.

For example, the vorticity of Figure 6 in [3] should be compared to Fig. 6 here. The absolute value of the dimensional vorticity within the leading vortex at $t_0^* = \frac{2}{6}T_0^*$ in the axisymmetric study [3][2] is three times larger than in the present 2D investigation. The qualitative appearance of the vorticity contours look the same as in [3] but their high levels of vorticity are not reached here.

A similar difference between the axisymmetric results of Figure 5 in [3] and the present 2D results in Fig. 4 are observed for the diverging orifice.

The velocity profile u/U_M of Fig. 4 in [3] (lower subplot) shows similar features as the corresponding profile in Fig. 7. Grid refinement indicates that the general features of the pulsating jets are well captured with the 361 × 121 grids, whereas the resolution of details in the vortex structures requires finer grids like the 721 × 241 grids used for comparison in Figs. 7–9a–d.

5. Conclusions

The 2D compressible Navier–Stokes equations in perturbation form are solved by a strictly stable fourth order difference method to simulate confined pulsating jets at $Re = 3000$, $M = 0.2$ in simplified 2D models of the human vocal tract. The vortex dynamics is investigated and compared to axisymmetric results by Zhao et al. [3] indicating lower vorticity for 2D than axisymmetric flow.

Acknowledgement

The introduction to phonation by Christoph Brücker, Michael Triep (both now at TU Freiberg, Germany), and Malte Kob (Universitätsklinikum Aachen, Germany) during a sabbatical at the Institute of Aerodynamics, RWTH Aachen, are gratefully acknowledged by the second author.

The parallelization of the Navier–Stokes code using OpenMP by our colleague Jarmo Rantakokko, Uppsala University, Sweden, is gratefully acknowledged.

References

[1] Fant G. Acoustic theory of speech production. Mouton, The Hague; 1960.
[2] Stevens KN. Acoustic phonetics. Cambridge, (MA): MIT Press; 1998.
[3] Zhao W, Frankel SH, Mongeau L. Numerical simulations of sound from confined pulsating axisymmetric jets. AIAA J 2001;39(10):1868–74.
[4] Zhao W, Zhang C, Frankel SH, Mongeau L. Computational aeroacoustics of phonation, Part I: computational methods and sound generation mechanisms. J Acoust Soc Am 2002;112(5):2134–46.
[5] Zhang C, Zhao W, Frankel SH, Mongeau L. Computational aeroacoustics of phonation, Part II: effects of flow parameters and ventricular folds. J Acoust Soc Am 2002;112(5):2147–54.
[6] Gustafsson B, Kreiss H-O, Oliger J. Time dependent problems and difference methods. New York: John Wiley & Sons; 1995.
[7] Strand B. Summation by parts for finite difference approximations for d/dx. J Comput Phys 1994;110:47–67.
[8] Müller B. High order numerical simulation of aeolian tones. Comput Fluids 2008;37(4):450–62.
[9] Sesterhenn J, Müller B, Thomann H. On the cancellation problem in calculating compressible low Mach number flows. J Comput Phys 1999;151:597–615.
[10] Müller B. Computation of compressible low Mach number flow. Habilitation thesis, ETH Zürich; 1996.
[11] Lerat A, Corre C. A residual-based compact scheme for the compressible Navier–Stokes equations. J Comput Phys 2001;170(2):642–75.
[12] Corre C, Lerat A. High-order residual-based compact schemes for advection–diffusion problems. Comput Fluids 2008;37(5):505–19.
[13] Mattsson K, Nordström J. Finite difference approximations of second derivatives on summation by parts form. J Comput Phys 2004;199:503–40.
[14] Kormann K, Kronbichler M. High order finite difference approximations for parabolic and hyperbolic-parabolic problems with variable coefficients.

[2] obtained by counting contour levels.

Project report, Department of Information Technology, Uppsala University; 2006.
[15] Kreiss H-O, Wu L. On the stability definition of difference approximations for the initial boundary value problem. Appl Numer Math 1993;12:213–27.
[16] Poinsot TJ, Lele SK. Boundary conditions for direct simulations of compressible viscous flows. J Comput Phys 1992;101:104–29.
[17] Larsson M. Numerical simulation of human phonation. Master's thesis in engineering physics, Uppsala University; 2007.
[18] Bruecker C, Triep M, Kob M. Study of the vortex dynamics in a mechanical model of the vocal folds using particle-image velocimetry. In: International conference on voice physiology and biomechanics, Marseille, France; 2004 Available from: http://icv2004.free.fr/download/bruecker.pdf.

PAPER 2

M. Larsson, B. Müller: Numerical Simulation of Fluid-Structure Interaction in Human Phonation. *MekIT '09: Fifth national conference on Computational Mechanics*, Trondheim 26–27 May 2009, editors Bjørn Skallerud and Helge I. Andersson, Tapir Academic Press, 2009, 261–280.

Numerical Simulation of Fluid-Structure Interaction in Human Phonation

Martin Larsson* **and Bernhard Müller**
Department of Energy and Process Engineering, Faculty of Engineering Science
The Norwegian University of Science and Technology
e–mail: martin.larsson@ntnu.no, bernhard.muller@ntnu.no

Summary Fluid-structure interaction in a simplified two-dimensional model of the larynx is considered to study human phonation. The flow is driven by an imposed pressure gradient across the glottis and interacts with the moving vocal folds in a self-sustained oscillation. The flow is computed by solving the 2D compressible Navier–Stokes equations using a high order finite difference method, which has been constructed to be strictly stable for linear hyperbolic and parabolic problems. The motion of the vocal folds is obtained by integrating the elastodynamic equations with a neo-Hookean constitutive model. Fluid and structure interact in a two-way coupling using a similar high order difference method. In each time step at the fluid-structure interface, the structure provides the fluid with new no-slip boundary conditions and new grid velocities, and the fluid provides the structure with new traction boundary conditions. The frequency obtained in our simulation is close to values observed in human phonation.

Introduction

Fluid-structure interaction (FSI) occurs when a flexible structure interacts with a fluid. The fluid flow exerts a stress on the structure which causes it to deform and thereby generate a new geometry for the fluid flow. This interaction is responsible for a wide range of phenomena which are crucial in engineering applications such as aircraft design and bridge construction, where structural motion is undesirable. The coupling between fluid flow and structural motion also plays an important role in many biological systems such as the cardiovascular and respiratory systems. The pulsatile blood flow in viscoelastic arteries and the transient airflow in the upper airways are the prime examples. Numerically simulating FSI in such systems can help to better understand the underlying biological mechanisms and potentially advance medical treatments [7].

A direct consequence of FSI in the vocal tract is voice generation, where the motion of the soft tissue of the vocal folds (cf. fig. 1) interacts dynamically with the glottal airflow to produce sound. The self-sustained oscillation of the vocal folds can be explained by the Bernoulli principle which states that in the absence of gravity for inviscid incompressible steady flow, the velocity v, pressure p and density ρ are related by $p + \rho v^2/2 = \text{const}$. The vocal folds being closed in their equilibrium position, initially at rest, are forced apart by the increasing lung pressure. As the air starts flowing, the velocity in the glottis increases and thus the pressure must decrease according to the Bernoulli principle. The pressure drop together with restoring elastic forces results in a closure of the vocal folds and a build-up of pressure. This cycle then repeats itself, driven only by the lung pressure. The computational challenge in aeroelastic simulations lies in dealing with unsteady flows at high Reynolds numbers, large deformations, moving interfaces, fluid-structure interaction and intrinsically 3D motion [7].

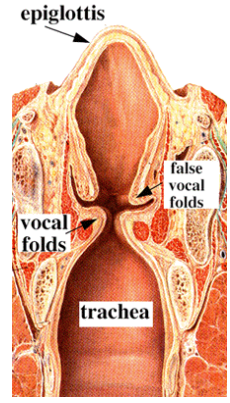

Figure 1: Cross section of larynx.

Fluid-structure interaction modelling

When solving FSI problems one has to consider the two-way coupling between the distinct physical models, i.e. fluid and structural mechanics. This can be accomplished in two ways: either *direct* or *sequential* multidisciplinary approaches. In the direct coupled field analysis approach, one solves for all the degrees of freedom of the system in one single sweep, whereas in the sequential coupling approach, the results of one solver iteration (e.g. fluid motion) is passed on as loads (traction) to the next one. Treating the flow and structural equations as one monolithic system (*direct* coupling) seems like an attractive approach from a modeling point of view. In doing so, however, one has to sacrifice efficiency and restrict to smaller-scale aeroelastic problems [35]. Historically, solution techniques for the different physical fields have evolved separately and naturally one seeks to make use of the matured techniques already available in the separate fields. Therefore, sequential coupling procedures are usually preferred, since they do not require a dedicated code [5].

Numerical models of phonation with fluid-structure interaction

The vibratory properties of the vocal folds are mainly attributed to the *lamina propria* (cf. figure 2) which is the main constituent in the mucous membranes that line various tubes in the body, particularly in the vocal tract. The lamina propria by itself is a thin layer of loose connective tissues which together with the epithelium constituate the mucosa. The functional layers of the vocal fold, with respect to phonation, can be divided into the vocal fold cover (mucosa) and the vocal fold ligament.

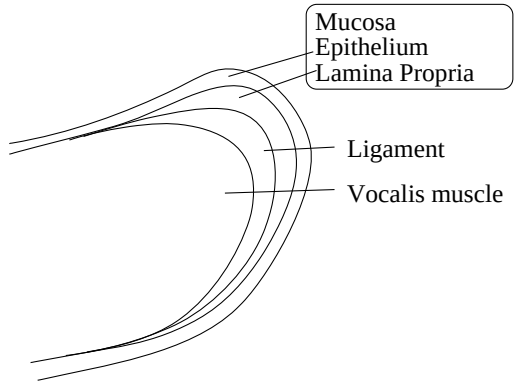

Figure 2: Sketch of the layered structure of the vocal fold. The mucosa (cover) consists of the epithelium and the lamina propria. The ligament is between the cover and the vocalis muscle.

Self-oscillating computational models for the vocal folds, driven by the pressure predicted from the Bernoulli relation were first developed in the late 1960s by Flanagan [6]. These basic models for the vocal folds comprise one or two masses coupled to a spring forming an oscillating mass-spring system. These simple but elegant models successfully captured the self-sustained vibration of the vocal folds. Multi-mass models were subsequentially developed by Titze in the mid-1970s [29] and similar models were used with variations until the mid-1990s when a body-cover model for the two-mass model was developed by Story and Titze [27] to incorporate the multi-layered nature of the vocal folds. Even though the early lumped mass models were elegant in concept, there is considerable doubt whether they represent the actual geometry and viscoelastic properties of the vocal folds adequately enough to identify voice disorders and special voice qualities [1].

In the mid-1990s, more elaborate models for the vocal folds were developed based on continuum models. A finite element method was used by Alipour and Titze [3] to model the vocal fold deformation, coupled to the flow field obtained through a Navier–Stokes solver. Finite element methods proved much higher accuracy and predictive power than lumped multi-mass models, and were also more suited for handling complex geometries and driving forces. More elaborate models were developed [1, 2], accounting for the transverse isotropy and layered structure of

the vocal folds, still assuming small deformations. In 2003, the presence of the false vocal folds was investigated in [23] using a finite element model. Recently, a sharp-interface immersed-boundary method was developed in [15] to simulate the fluid-structure interaction between an incompressible fluid flow and vocal folds with a linear viscoelastic model.

Recently, numerical simulations of phonation based on the compressible Navier–Stokes equations have been performed [33, 34, 32]. Like in direct numerical simulation, high order discretization methods have been preferred for the numerical solution of the compressible Navier–Stokes equations in aeroacoustics, because higher order methods are more efficient for high accuracy requirements than low order methods.

In this paper, we employ a high order finite difference approach based on summation by parts (SBP) operators [28, 9, 8] to solve the compressible Navier–Stokes equations. The compressible Navier–Stokes equations have been chosen to simulate not only the dynamics of the fluid motion but also the generation and propagation of sound waves [31]. A high-order method was chosen because of high accuracy requirements in fluid simulation of sound generation [31]. Opposed to conventional difference approximations, our high order finite difference methods have the advantage of being constructed to be strictly stable for linear hyperbolic and parabolic problems even for non-periodic boundary conditions. The sixth order SBP operator [28], which is third order accurate near the boundaries, is employed to discretize the first derivatives in the 2D compressible Navier–Stokes equations. The second derivatives in the compressible Navier–Stokes equations and the elastodynamic equations are approximated by applying the SBP operator for the first derivatives twice. The SBP operator has previously been used to simulate aeolian tones [19]. The Navier–Stokes equations in conservative form are expressed in perturbation form [25, 18, 19] to minimize rounding errors caused by cancellation in low Mach number flow computations.

Utilizing similar high order finite difference methods, we have also developed an explicit solver for the Lagrangean field equations of structural mechanics and coupled it to our solver for the compressible Navier–Stokes equations in an ALE formulation. Since during phonation, the vocal folds undergo large displacements from their equilibrium configuration, a finite-strain model is needed to model the structure accurately. Our implementation for the structure solver can solve for the dynamic response of the structure due to external loads such as the traction force from a fluid flow. It differs from typical finite-element implementations, in particular with regard to the traction boundary condition which is not trivial to impose in a strong formulation. This issue is elaborated upon below. The advantage of this approach over unstructured methods is that we can have structured grids in both domains (fluid and structure) and matching grid points on the interface without need for interpolation, which increases the accuracy of the computation. Finite element and Cartesian grid immersed-boundary methods have the advantage over structured finite difference methods of handling complex domains better. In this study, we only consider simple domains in 2D. P. Šidlof [26] notes that the vortex dynamics in 2D and 3D are substantially different and that only the 3D simulation can yield reliable results. Nevertheless, 2D numerical methods are prerequisites for the development of 3D ones.

This paper is organized as follows: We start by describing finite strain theory of structural mechanics and continue to present the Navier–Stokes equations of fluid dynamics in perturbation formulation. Then the explicit fluid-structure coupling scheme is outlined. In the next chapter, we present the high order finite difference method and the explicit Runge–Kutta time integration scheme. Results and conclusions are stated at the end.

Finite strain theory

Notation

Finite strain theory is well developed, but the different notations found in the literature can be confusing and sometimes misleading. Therefore, a thorough explanation of basic quantities is warranted here. Let a deformable body occupy some region Ω_0 in space (cf. figure 3). With every particle in the body a coordinate vector $\mathbf{X} = (X, Y, Z)$ called the reference coordinate of the particle is associated. The set Ω_0 is called the reference configuration of the body. As the body translates, rotates and deforms through space, the particle originally at position $\mathbf{X}$ is now at a new position $\mathbf{x} = (x, y, z)$ in the current configuration of the body Ω. A mapping can be defined that associates each reference coordinate with the current coordinate, $\mathbf{x} = \tilde{\boldsymbol{\phi}}(\mathbf{X}, t)$. The displacement from the reference configuration is then $\boldsymbol{\phi}(\mathbf{X}, t) = \tilde{\boldsymbol{\phi}}(\mathbf{X}, t) - \mathbf{X}$. A small line element in the reference configuration $d\mathbf{X}$ transforms to $dx_i = (\partial x_i/\partial X_\alpha)dX_\alpha = F_{i\alpha}dX_\alpha$, where $\mathbf{F} = \nabla_{\mathbf{X}}\tilde{\boldsymbol{\phi}}(\mathbf{X}, t)$ is the deformation gradient. For later convenience, also define $\mathbf{B} = \mathbf{F}^{-\mathrm{T}}$ so that $B_{i\alpha} = \partial X_\alpha/\partial x_i$. Tensor notation provides a compact way to write the equations. Here, use will be made of both tensor and index notation.

Governing equations

Neglecting external forces, the Lagrangean field equations [20] which describe the motion of the body, expressed in terms of the nominal stress tensor $\mathbf{S}$ are

$$\frac{\partial S_{\alpha i}}{\partial X_\alpha} = \rho_0 \ddot{\phi}_i. \tag{1}$$

Here, ρ_0 is the density of the body in the reference configuration. Superscript dots denote Lagrangean time derivatives at fixed $\mathbf{X}$, also known as material time derivatives, i.e.

$$\dot{\boldsymbol{\phi}} \equiv \left.\frac{\partial \boldsymbol{\phi}(\mathbf{X}, t)}{\partial t}\right|_{\mathbf{X}} \equiv \frac{\partial \boldsymbol{\phi}}{\partial t}.$$

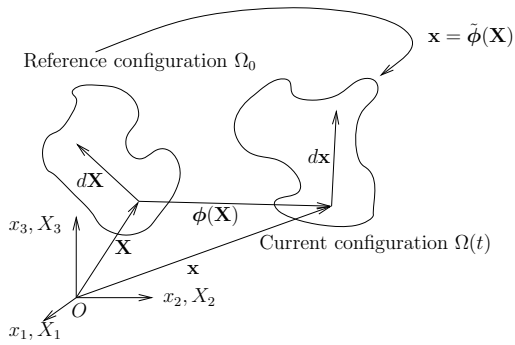

Figure 3: Variables in continuum deformation

Constitutive relations

Define the right Cauchy–Green deformation tensor as $\mathbf{C} = \mathbf{F}^{\mathrm{T}}\mathbf{F}$ and the Green strain tensor $\mathbf{E} = \frac{1}{2}(\mathbf{C} - \mathbf{1})$ where $\mathbf{1}$ is the identity tensor. It is often convenient to consider the elastic properties of a homogeneous material to be derived from a strain energy function $W(\mathbf{E})$ depending on the Green strain tensor only. Such a material is called hyperelastic and this assumption is frequently used in modeling of biological tissues. With this functional dependence, objectivity is asserted [21], i.e. the stored elastic energy is unaffected by superimposed rigid translations and rotations. When there is no deformation, i.e. $\mathbf{F} = \mathbf{1}$ and $\mathbf{E} = \mathbf{0}$ the strain energy must reduce to zero, so that $W(\mathbf{0}) = 0$. The second Piola–Kirchhoff stress tensor (2PK for short) in hyperelasticity is

$$\boldsymbol{\Sigma} = \frac{\partial W(\mathbf{E})}{\partial \mathbf{E}} = 2\frac{\partial W(\mathbf{C})}{\partial \mathbf{C}} \tag{2}$$

where the partial derivative is to be interpreted as $\Sigma_{ij} = \partial W/\partial E_{ij}$. The nominal stress is in turn obtained by $\mathbf{S} = \boldsymbol{\Sigma}\mathbf{F}^{\mathrm{T}}$. The constitutive model for the material is in the functional form of W

which can be an explicit expression for the components of $\mathbf{E}$ (strain-based formulation), but it is often easier to define a material model in terms of the principal invariants of the Cauchy-Green tensor $\mathbf{C}$ (invariant-based formulation), namely $W = W(\mathbf{C}) = W(I_1(\mathbf{C}), I_2(\mathbf{C}), I_3(\mathbf{C}))$ where

$$I_1(\mathbf{C}) = \mathrm{tr}(\mathbf{C}), \quad I_2(\mathbf{C}) = \frac{1}{2}(I_1(\mathbf{C})^2 - \mathrm{tr}(\mathbf{C}^2)) \quad \text{and} \quad I_3(\mathbf{C}) = \det \mathbf{C}.$$

In the invariant-based framework, the derivatives of the invariants with respect to the symmetric deformation tensor are

$$\frac{\partial I_1(\mathbf{C})}{\partial \mathbf{C}} = \mathbf{1}, \quad \frac{\partial I_2(\mathbf{C})}{\partial \mathbf{C}} = \mathrm{tr}(\mathbf{C})\mathbf{1} - \mathbf{C} \quad \text{and} \quad \frac{\partial I_3(\mathbf{C})}{\partial \mathbf{C}} = \mathbf{C}^{-1} \det \mathbf{C}. \tag{3}$$

The recipe for obtaining the nominal stress in the body for a given deformation $\mathbf{F}$ is then $\mathbf{F} \rightarrow \mathbf{C} \rightarrow I_{1,2,3}/\mathbf{E} \rightarrow W \rightarrow \mathbf{\Sigma} \rightarrow \mathbf{S}$.

Invariant-based formulations

Consider the neo-Hookean type strain energy function given as $W(\mathbf{C}) = W(I_1(\mathbf{C}), I_3(\mathbf{C})) = \frac{\mu}{2}(I_1 - 3) - \frac{\mu}{2}\ln I_3 + \frac{\lambda}{8}(\ln I_3)^2$. To obtain The 2PK stress for this model, use the definition (2) and the invariant derivatives (3) to obtain

$$\mathbf{\Sigma} = 2\frac{\partial W}{\partial \mathbf{C}} = 2\frac{\partial W}{\partial I_1}\frac{\partial I_1}{\partial \mathbf{C}} + 2\frac{\partial W}{\partial I_3}\frac{\partial I_3}{\partial \mathbf{C}} = \mu\mathbf{1} + \left(\frac{\lambda}{2}\ln\det\mathbf{C} - \mu\right)\mathbf{C}^{-1}. \tag{4}$$

For a rigid body motion, the deformation gradient is a an orthogonal tensor which implies that $\mathbf{C}$ is the identity tensor. So, for this model, $\mathbf{\Sigma}(\mathbf{C} = \mathbf{1}) = \mathbf{0}$ and $W(\mathbf{C} = \mathbf{1}) = 0$, as expected.

Boundary conditions

(i) Displacement boundary condition

On a boundary Γ_1 where the body is fixed in space, the boundary condition is given directly for the unknown displacements $\boldsymbol{\phi}(\mathbf{X}, t) = \mathbf{f}(\mathbf{X})$, a given function of space. A commonly used boundary condition is that the body should be fixed to its reference configuration on a part of the boundary, in which case one would have $\mathbf{f}(\mathbf{X}) = \mathbf{0}$.

(ii) Condition of traction

If the body experiences traction on a boundary Γ_2 (typically from a surrounding material, e.g. a fluid), a traction condition must be specified on that boundary. In general, this condition can be expressed as $\mathbf{S}^{\mathrm{T}}\mathbf{N} = \mathbf{T}$ where $\mathbf{S}$ is the nominal stress, $\mathbf{N}$ the outward unit normal and $\mathbf{T}$ a given force per unit area on the boundary in the reference configuration.

As an example, consider the case of a static fluid pressure acting on the body. Naturally, the fluid around the body does not recognize anything else than the current configuration Ω of the body, which has some unit outward normal $\mathbf{n}$. The force $\mathbf{t}$ exerted by the fluid on a small area element da on the boundary of the body is then $\mathbf{t} = -p\mathbf{n}da$, where p is the static fluid pressure. According to Nanson's formula [20], the directed area element $\mathbf{n}da$ in Ω is related to a corresponding element $\mathbf{N}dA$ in Ω_0 through $\mathbf{n}da = \det(\mathbf{F})\mathbf{B}\mathbf{N}dA$ with $\mathbf{B} = \mathbf{F}^{-\mathrm{T}}$. Thus, the force per unit area in the reference configuration can be written as $\mathbf{T} = \mathbf{t}/dA = -p\det(\mathbf{F})\mathbf{B}\mathbf{N}$. Extension from static pressure to shear stress from a viscous fluid flow is now straightforward. A fluid with stress tensor $\boldsymbol{\sigma}^{\mathrm{f}}$ exerts a force $\mathbf{t} = \boldsymbol{\sigma}^{\mathrm{f}}\mathbf{n}da$ on an area element da. Using Nanson's formula again, the force per unit area in the reference configuration can be written

$$\mathbf{T} = \det(\mathbf{F})\boldsymbol{\sigma}^{\mathrm{f}}\mathbf{B}\mathbf{N}. \tag{5}$$

This formula also includes the static fluid pressure case, for which $\boldsymbol{\sigma}^{\mathrm{f}} = -p\mathbf{1}$. Furthermore, in a compressible viscous fluid, the stress is

$$\boldsymbol{\sigma}^{\mathrm{f}} = \left(-p - \frac{2}{3}\mu^{\mathrm{f}}\nabla\cdot\mathbf{u}^{\mathrm{f}}\right)\mathbf{1} + \mu^{\mathrm{f}}\left(\nabla\mathbf{u}^{\mathrm{f}} + \left(\nabla\mathbf{u}^{\mathrm{f}}\right)^{\mathrm{T}}\right) \tag{6}$$

where μ^{f} is the fluid viscosity and $\mathbf{u}^{\mathrm{f}}$ is the fluid velocity.

Transformation

In order to transform the reference configuration to a computational domain, a set of computational coordinates ξ, η is introduced. The coordinates in the reference configuration can then be written $X = X(\xi,\eta), Y = Y(\xi,\eta)$. Since the transformation is invertible, the opposite relations $\xi = \xi(X,Y), \eta = \eta(X,Y)$ hold as well. Differentiating these transformations yields two vector equations for the Jacobian matrices where one must be the inverse of the other, hence the metric identities are $J^{-1}\xi_X = Y_\eta$, $J^{-1}\xi_Y = -X_\eta$, $J^{-1}\eta_X = -Y_\xi$, $J^{-1}\eta_Y = X_\xi$ where

$$J^{-1} = X_\xi Y_\eta - X_\eta Y_\xi \tag{7}$$

is the Jacobian determinant of the transformation. Transforming the Lagrangean field equations to computational coordinates gives

$$\begin{aligned} J^{-1}\rho_0\ddot{\boldsymbol{\phi}} = {} & (J^{-1}\xi_X\mathbf{S}_1 + J^{-1}\xi_Y\mathbf{S}_2)_\xi + (J^{-1}\eta_X\mathbf{S}_1 + J^{-1}\eta_Y\mathbf{S}_2)_\eta \\ & - \mathbf{S}_1[(J^{-1}\xi_X)_\xi + (J^{-1}\eta_X)_\eta] - \mathbf{S}_2[(J^{-1}\xi_Y)_\xi + (J^{-1}\eta_Y)_\eta], \end{aligned} \tag{8}$$

where the notation $S_{\alpha i} = (\mathbf{S}_\alpha)_i$ has been used, i.e. $\mathbf{S}_1$ and $\mathbf{S}_2$ viewed as column vectors are the columns of $\mathbf{S}^{\mathrm{T}}$. The terms in square brackets cancel because of the metric identities and the fact that the partial derivatives commute. What remains is

$$\ddot{\boldsymbol{\phi}} = \frac{1}{J^{-1}\rho_0}\left[(\widehat{\mathbf{S}_1})_\xi + (\widehat{\mathbf{S}_2})_\eta\right] \tag{9}$$

where $\widehat{\mathbf{S}_1} = J^{-1}\mathbf{S}^{\mathrm{T}}\nabla\xi$ and $\widehat{\mathbf{S}_2} = J^{-1}\mathbf{S}^{\mathrm{T}}\nabla\eta$ are transformed momentum flux vectors. Finally, the transformed equations of motion (9) are rewritten as a system of equations with only first time derivatives. Defining $\boldsymbol{\psi} = \dot{\boldsymbol{\phi}}$, the system becomes

$$\begin{cases} \dot{\boldsymbol{\psi}} = \frac{1}{J^{-1}\rho_0}\left[(\widehat{\mathbf{S}_1})_\xi + (\widehat{\mathbf{S}_2})_\eta\right] \\ \dot{\boldsymbol{\phi}} = \boldsymbol{\psi} \end{cases} \tag{10}$$

where the unknowns are the displacements $\boldsymbol{\phi}$ and the velocities $\boldsymbol{\psi}$. This system has 4 unknowns in 2D.

Compressible Navier–Stokes equations

The perturbation formulation is used to minimize cancellation errors when discretizing the Navier–Stokes equations for compressible low Mach number flow [25, 18]. The 2D compressible Navier–Stokes equations in conservative form can be expressed in perturbation form as [19, 14]

$$\mathbf{U'}_t + \mathbf{F}^{c\prime}{}_x + \mathbf{G}^{c\prime}{}_y = \mathbf{F}^{v\prime}{}_x + \mathbf{G}^{v\prime}{}_y, \tag{11}$$

where the vector $\mathbf{U}'$ denotes the perturbation of the conservative variables with respect to the stagnation values. $\mathbf{U}'$ and the inviscid (superscript c) and viscous (superscript v) flux vectors are defined by

$$\mathbf{U}' = \begin{pmatrix} \rho' \\ (\rho u)' \\ (\rho v)' \\ (\rho E)' \end{pmatrix}, \; \mathbf{F}^{c\prime} = \begin{pmatrix} (\rho u)' \\ (\rho u)'u' + p' \\ (\rho v)'u' \\ (\rho_0 H_0 + (\rho H)')u' \end{pmatrix}, \; \mathbf{G}^{c\prime} = \begin{pmatrix} (\rho v)' \\ (\rho u)'v' \\ (\rho v)'v' + p' \\ (\rho_0 H_0 + (\rho H)')v' \end{pmatrix},$$

$$\mathbf{F}^{v\prime} = \begin{pmatrix} 0 \\ \tau'_{xx} \\ \tau'_{xy} \\ \tau'_{xx}u' + \tau'_{xy}v' + \kappa T'_x \end{pmatrix}, \; \mathbf{G}^{v\prime} = \begin{pmatrix} 0 \\ \tau'_{yx} \\ \tau'_{yy} \\ \tau'_{yx}u' + \tau'_{yy}v' + \kappa T'_y \end{pmatrix}.$$

The subscripts in (11) subsequently denote derivatives. We assume perfect gas. The perturbation variables (superscript $'$) are defined with respect to their stagnation values (subscript $_0$), i.e. $\rho' = \rho - \rho_0$, $(\rho\mathbf{u})' = \rho\mathbf{u}$, $(\rho E)' = \rho E - (\rho E)_0$, $(\rho H)' = (\rho E)' + p'$, $\mathbf{u}' = \frac{(\rho\mathbf{u})'}{\rho_0+\rho'}$, $p' = (\gamma-1)[(\rho E)' - \frac{1}{2}((\rho\mathbf{u})'\cdot\mathbf{u}')]$, $\tau' = \mu(\nabla\mathbf{u}' + (\nabla\mathbf{u}')^T) - \frac{2}{3}\mu(\nabla\cdot\mathbf{u}')\mathbf{I}$, $T' = \frac{p'/R - \rho' T_0}{\rho_0+\rho'}$. Time is t, and x and y are the Cartesian coordinates. Denoted by ρ is the density, u and v the x- and y-direction velocities, E the specific total energy, p the pressure, $\gamma = 1.4$ the ratio of specific heats for air, R the specific gas constant, μ viscosity determined from the Sutherland law $\frac{\mu}{\mu_0} = (\frac{T}{T_0})^{1.5}\frac{1+S_c}{\frac{T}{T_0}+S_c}$ with the nondimensional Sutherland constant $S_c = \frac{110}{301.75}$ and κ the heat conduction coefficient determined from the constant Prandtl number $\mathrm{Pr} = 1$. The quantities ρ_0, $(\rho E)_0$ and $(\rho H)_0$ denote the stagnation quantities of density, total energy density and total enthalpy density, respectively. The viscous flux vectors $\mathbf{F}^{v\prime}$ and $\mathbf{G}^{v\prime}$ are the same as for the standard conservative form, except for using the temperature perturbation T' instead of temperature T for the heat flux terms. The momentum density and velocity perturbations are taken as the same as their unperturbed counterparts, i.e. $(\rho\mathbf{u})' = \rho\mathbf{u}$ and $\mathbf{u}' = \mathbf{u}$, cf. the definition of $\mathbf{U}'$ with respect to $\mathbf{U}_0 = (\rho_0, 0, 0, (\rho E)_0)^T$ above. The 2D conservative compressible Navier–Stokes equations in perturbation form (11) are written in dimensional form, while their nondimensional form with ρ_0, stagnation speed of sound c_0, and $\rho_0 c_0^2$ as reference values of density, velocity, and pressure, respectively, has actually been used in the computations.

General moving geometries are treated by a time dependent coordinate transformation $\tau = t$, $\xi = \xi(t,x,y)$, $\eta = \eta(t,x,y)$. The transformed 2D conservative compressible Navier–Stokes equations in perturbation form read

$$\hat{\mathbf{U}}'_\tau + \hat{\mathbf{F}}'_\xi + \hat{\mathbf{G}}'_\eta = 0\,, \tag{12}$$

where $\hat{\mathbf{U}}' = J^{-1}\mathbf{U}'$, $\hat{\mathbf{F}}' = J^{-1}(\xi_\tau\mathbf{U}' + \xi_x(\mathbf{F}^{c\prime} - \mathbf{F}^{v\prime}) + \xi_y(\mathbf{G}^{c\prime} - \mathbf{G}^{v\prime}))$ and $\hat{\mathbf{G}}' = J^{-1}(\xi_\tau\mathbf{U}' + \eta_x(\mathbf{F}^{c\prime} - \mathbf{F}^{v\prime}) + \eta_y(\mathbf{G}^{c\prime} - \mathbf{G}^{v\prime}))$. The x- and y-derivatives in the viscous flux vectors $\mathbf{F}^{v\prime}$ and $\mathbf{G}^{v\prime}$ are expressed using the chain rule, e.g. $u'_x = u'_\xi\xi_x + u'_\eta\eta_x$ and $u'_y = u'_\xi\xi_y + u'_\eta\eta_y$. The Jacobian determinant of the transformation J is determined by $J^{-1} = x_\xi y_\eta - x_\eta y_\xi$, and the metric terms by $J^{-1}\xi_x = y_\eta$, $J^{-1}\xi_y = -x_\eta$, $J^{-1}\eta_x = -y_\xi$, $J^{-1}\eta_y = x_\xi$.

Fluid-structure interaction

ALE formulation for fluid solver

The displacement of the structure interface determines the shape of the fluid domain and the structure velocity at the interface determines the internal grid point velocities in the fluid domain. The right and left boundaries of the fluid domain are the out- and inflow, respectively. The top and bottom parts of the fluid domain are bounded by the flexible vocal folds and the inner wall of the airpipe which is assumed to be rigid. We do not assume symmetry; the motion of the two vocal folds are solved for individually. In our ALE formulation, the positions and velocities of the grid points in the fluid domain are a linear interpolation of the positions and velocities of the structure at the interface. Figure 4 shows the given structure veolcity with a bold arrow and the interpolated grid point velocities $\dot{x}, \dot{y}$ (thin arrow) for three grid lines.

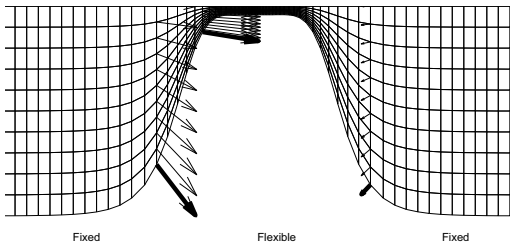

Figure 4: The boundary of the fluid domain consists of fixed and flexible parts. The velocity at the boundary of the flexible part determines the internal grid point velocity. Only half domain shown.

To obtain the time derivative of J^{-1} as needed in (12), a geometric invariant [30] is used. This geometric conservation law states that $(J^{-1})_\tau + (J^{-1}\xi_t)_\xi + (J^{-1}\eta_t)_\eta = 0$. The time derivatives of the computational coordinates ξ, η can here be obtained from the grid point velocities $\dot{x}, \dot{y}$ as $\xi_t = -(\dot{x}\xi_x + \dot{y}\xi_y)$, $\eta_t = -(\dot{x}\eta_x + \dot{y}\eta_y)$ which can be seen by differentiating the transformation with respect to τ.

Traction boundary condition in transformed coordinates

The traction boundary condition is somewhat strange, because it does not directly give a relation for the unknowns that must be satisfied, unlike the displacement boundary condition. Rather, as will be shown, it specifies the flux of momentum on the boundary. As can be seen in equation (5), the unit normal is needed for the boundary condition. This can easily be constructed from the coordinate transformation. For example, a coordinate line where $\eta = \mathrm{const}$ is a level curve for the function $\eta(X, Y)$. Hence, the gradient $\nabla_{\mathbf{X}}\eta$ is perpendicular to this line and the unit normal is then simply $\mathbf{N} = \nabla\eta/|\nabla\eta|$ (where the subscript $\mathbf{X}$ has been dropped for convenience), pointing in the direction of increasing η. A boundary condition for viscous fluid stress on a boundary where $\eta = \eta_{\max}$ is then obtained by inserting the unit normal into $\mathbf{S}^{\mathrm{T}}\mathbf{N} = \mathbf{T}$, with $\mathbf{T}$ given by eq. (5), hence $\mathbf{S}^{\mathrm{T}}\nabla\eta = \det(\mathbf{F})\boldsymbol{\sigma}^{\mathrm{f}}\mathbf{B}\nabla\eta$. Since $\mathbf{B}$ is just the inverse of a 2-by-2 matrix, it can be explicitly calculated in terms of the deformation gradient components. Furthermore, multiply both sides by J^{-1} to get the final expression for the momentum flux in the η-direction,

$$\widehat{\mathbf{S}_2} \equiv J^{-1}\mathbf{S}^{\mathrm{T}}\nabla\eta \stackrel{!}{=} J^{-1}\boldsymbol{\sigma}^{\mathrm{f}} \begin{pmatrix} F_{22} & -F_{21} \\ -F_{12} & F_{11} \end{pmatrix} \nabla\eta. \tag{13}$$

This is the boundary condition that must be fulfilled, i.e. when calculating the η-derivative in (9), we use the value (13) at the boundary. A boundary condition for the ξ-direction can be constructed similarly if needed.

Description of fluid-structure interaction algorithm

First, we construct the fixed reference configuration for the structure, set the initial displacements and velocities to zero. The initial fluid domain is then uniquely determined by the reference boundary of the structure. Initially, the fluid grid points have zero velocity and the wall

does not move. We then take one time step for the fluid with imposed pressure boundary conditions at the inflow, zero initial conditions for the perturbation variables $\mathbf{U}'$ and adiabatic no-slip conditions, i.e. $\mathbf{u} = 0$ and $\partial T/\partial n = 0$ on the wall. After the first fluid time step, the viscous fluid stress on the wall is calculated based on the new fluid velocities and pressures using (6). These fluid stresses are passed on to the structure via the traction boundary condition (13). With this boundary condition imposed, one time step is taken for the structure. The solution for the structure gives the velocity and displacement on the boundary (and all internal points) and these are then used to generate the new fluid mesh and internal grid point velocities. This procedure is then repeated for as many time steps as required.

High order finite difference method

Summation by parts operators

Let $v_j, j = 0, \ldots N$, be an approximation to the exact solution $u(x_j)$ at the grid point $x_j = jh$ where $h = 1/N$. The discrete scalar product and norm are [28] $(u, v)_h = hu^T Hv, \quad ||u||_h^2 = (u, u)_h$ where the norm matrix H is diagonal and positive definite. The *summation by parts* (SBP) property, analogous to integration by parts in the continuous case, is satisfied, if $(u, Qv)_h = u_N v_N - u_0 v_0 - (Qu, v)_h$ for a difference operator Q. Let the operator Q be defined in terms of B as $hQ = H^{-1}B$. The SBP property can be rewritten as $hu^T HQv = u^T \mathrm{diag}(-1, 0, \ldots, 0, 1)v - h(Qu)^T Hv$ and rearranged to $hu^T(HQ + Q^T H)v = u^T \mathrm{diag}(-1, 0, \ldots, 0, 1)v$. Now, H is diagonal by definition so $H = H^T$, hence $u^T(HhQ + (HhQ)^T)v = u^T \mathrm{diag}(-1, 0, \ldots, 0, 1)v$. Using the definition of Q and the fact that u and v are arbitrary, we get $B + B^T = \mathrm{diag}(-1, 0, \ldots, 0, 1)$.

The difference operator Q is an approximation to the first derivative, i.e. $(Qv)_j \approx \frac{du(x_j)}{dx}$. If Q is accurate of order 2τ in the interior, then there is a diagonal norm matrix H, such that Q is accurate of order τ near the boundaries [28]. When $\tau = 3$ which is the case considered here, there is a one-parameter family of operators Q. One of the elements in the matrix of Q can be set to zero in such a way that the bandwidth of the matrix is minimized to obtain a unique matrix Q which yields a 6th order accurate operator in the interior. Thus, the global order of accuracy of the present SBP operator Q is $\tau + 1 = 4$ [9, 8].

Second derivatives are approximated by applying the SBP operator Q twice. Alternative discretizations of second derivatives [16, 11] are discussed in [19]. Opposed to conventional difference operators, SBP operators allow energy estimates for the discrete problems similar to the ones for the continuous problems, which are approximated. Thus, SBP operators yield strictly stable schemes for general boundary conditions.

If the x-derivative in the convection diffusion equation $u_t + au_x = bu_{xx}$, where a and b are assumed to be constant and $b > 0$, is approximated by a standard central pth order finite difference operator $Q_x^{(p)}$ and the time derivative by an explicit Runge-Kutta method, the von Neumann stability analysis leads to the stability condition $\Delta t(-a\hat{Q}^{(p)} + b(\hat{Q}^{(p)})^2) \in S$, where $\hat{Q}^{(p)}$ is the Fourier transform of $Q_x^{(p)}$ and S the stability domain of the Runge–Kutta method. $\hat{Q}^{(p)} \frac{\Delta x}{i}$ is the approximate wave number $\tilde{k}\Delta x$. For SBP operators, the stability condition is more restrictive, because $\Delta t \parallel -aQ_x^{(p)} + b(Q_x^{(p)})^2 \parallel \leq R < R_1$ is required, where the open semicircle $\{z \in \mathbb{C} \mid |z| < R_1 \text{ and } \mathrm{Real}(z) < 0\}$ is contained in the stability domain S [12]. In practical computations, however, it has been possible to use von Neumann stability condition with a safety margin. The von Neumann stability condition for the standard central sixth order difference operator $Q_x^{(6)}$ and the classical fourth order explicit Runge-Kutta method reads $CFL = \frac{|a|\Delta t}{\Delta x} \leq 1.783$ for $b = 0$ and $VNN = \frac{|b|\Delta t}{\Delta x^2} \leq 1.124$ for $a = 0$, while $CFL \leq 2.828$ for

$b = 0$ and $VNN \leq 2.828$ for $a = 0$ is required for the standard central second order operator $Q_x^{(2)}$. Note that $(Q_x^{(6)}\mathbf{u})_j = \frac{1}{\Delta x}(\frac{1}{60}u_{j+3} - \frac{3}{20}u_{j+2} + \frac{3}{4}u_{j+1} - \frac{3}{4}u_{j-1} + \frac{3}{20}u_{j-2} - \frac{1}{60}u_{j-3})$ and $\hat{Q}^{(6)} = \frac{i}{\Delta x}[\frac{3}{2}\sin(k\Delta x) - \frac{3}{10}\sin(2k\Delta x) + \frac{1}{30}\sin(3k\Delta x)]$, where k is the wave number in this subsection. With this information, the stability condition of a second order central method for the compressible Navier–Stokes equations in [17] can be easily generalized for the present high order method.

Approach for compressible Navier–Stokes equations

The transformed 2D compressible Navier–Stokes equations in perturbation form (12) are solved on a rectangle, where $\xi = 1$ and $\xi = jmax$ represent the inlet and outlet boundaries of the vocal tract, respectively, and $\eta = 1$ and $\eta = kmax$ correspond to the lower and upper walls of the vocal tract, respectively. The ξ- and η-derivatives in the metric terms are discretized by Strand's 3-6 SBP operator [28]. The viscous flux vectors are discretized by approximating the first ξ and η derivatives of u', v' and T', by Strand's 3-6 SBP operator. After the flux vectors $\hat{\mathbf{F}}'$ and $\hat{\mathbf{G}}'$ are computed at all grid points, $\hat{\mathbf{F}}'_\xi$ and $\hat{\mathbf{G}}'_\eta$ are approximated by employing Strand's 3-6 SBP operator once more. The classical fourth order explicit Runge-Kutta method is used for time integration (see below). Spurious high wave number oscillations are suppressed by a sixth order explicit filter [19].

Boundary conditions

No-slip adiabatic wall boundary conditions and the Navier–Stokes Characteristic Boundary Conditions (NSCBC) technique by Poinsot and Lele in [22] are employed.

At the inflow, pressure, temperature and velocity in the y-direction are imposed as $p = p_{\mathrm{atm}} + \Delta p, T = T_0 = 310\,\mathrm{K}$, and $v = 0$, respectively. The x-velocity u at the inflow and the pressure p at the solid walls are taken from the Navier–Stokes solution at those boundaries. At the outflow, the amplitudes of the characteristic waves $\mathcal{L}_1 = \lambda_1\,(p_x - \rho c u_x)$, $\mathcal{L}_2 = \lambda_2\,(c^2\rho_x - p_x)$, $\mathcal{L}_3 = \lambda_3 v_x$, $\mathcal{L}_4 = \lambda_4\,(p_x + \rho c u_x)$ are set to zero for ingoing waves. Imposing the atmospheric pressure p_{atm} at the outlet would lead to a well-posed problem but at the cost of numerical reflections. To keep numerical reflections low and the pressure close to atmospheric pressure, the amplitude of the ingoing wave is set to $\mathcal{L}_1 = K(p - p_{\mathrm{atm}})$ where the constant K, proposed by Rudy and Strikwerda [24] is taken as $K = \sigma(1 - M^2)c/L$. Here, σ is a constant, M is the maximum Mach number, c the speed of sound and L a characteristic size of the domain. The choice $\sigma = 0$ corresponds to a perfectly non-reflecting case but without information about the atmospheric pressure. The value 0.25 was used in this study [22]. For reverse flow (i.e. negative x-velocity) at the outlet, we set $\mathcal{L}_1 = \mathcal{L}_2 = \mathcal{L}_3 = 0$.

Approach for the Langrangean field equations

The transformed 2D Lagrangean field equations (10) are discretized in the same way as the Navier–Stokes equations. The deformation gradient $\mathbf{F}$ and the derivatives of the flux vectors are approximated at all grid points using Strand's 3-6 SBP operator alike.

The computation of the right-hand side (9) for an internal grid point (i, j) is detailed below. At and near boundaries, the corresponding coefficients of the SBP operator $Q^{(6)}$ are used.

1. Given the displacement field $\boldsymbol{\phi} = (\phi^1, \phi^2)^T$, calculate the derivative with respect to the computational coordinate ξ using the high-order finite difference scheme $Q = Q^{(6)}$

$$\left(\frac{\partial \phi^k}{\partial \xi}\right)_{i,j} \approx Q_\xi \phi^k_{i,j} = -\frac{1}{60}\phi^k_{i-3,j} + \frac{3}{20}\phi^k_{i-2,j} - \frac{3}{4}\phi^k_{i-1,j} + \frac{3}{4}\phi^k_{i+1,j} - \frac{3}{20}\phi^k_{i+2,j} + \frac{1}{60}\phi^k_{i+3,j}$$

for both components k of the displacement. Approximate the η derivative similarly. The components of the deformation gradient at point (i,j)

$$(F_{k\alpha})_{i,j} = \left(\frac{\partial x_k}{\partial X_\alpha}\right)_{i,j} = \delta_{k\alpha} + \left(\frac{\partial \phi^k}{\partial X_\alpha}\right)_{i,j} = \\ \delta_{k\alpha} + \left(\frac{\partial \phi^k}{\partial \xi}\right)_{i,j}\left(\frac{\partial \xi}{\partial X_\alpha}\right)_{i,j} + \left(\frac{\partial \phi^k}{\partial \eta}\right)_{i,j}\left(\frac{\partial \eta}{\partial X_\alpha}\right)_{i,j}.$$

are then approximated by using the approximation of $(\partial\phi^k/\partial\xi)_{i,j}$ etc. above and by also discretizing the metric terms $(\partial\xi/\partial X_\alpha)_{i,j}$ etc. by the 6th order SBP operator.

2. Evaluate the components of the right Cauchy–Green deformation tensor according to $(C_{\alpha\beta})_{i,j} = (F_{k\alpha})_{i,j}(F_{k\beta})_{i,j}$.

3. Form the necessary functions of $\mathbf{C}$ as required by the material model, e.g. $(\det(\mathbf{C}))_{i,j} = (C_{11})_{i,j}(C_{22})_{i,j} - (C_{12})_{i,j}(C_{21})_{i,j}$.

4. Calculate the components of the 2PK stress using the material model, e.g. $(\Sigma_{\alpha\beta})_{i,j} = \mu_{i,j}\delta_{\alpha\beta} + (\lambda_{i,j}\ln(\det\mathbf{C})_{i,j}/2 - \mu_{i,j})(\mathbf{C}^{-1})_{\alpha\beta}$ where the space-dependent Lamé parameters λ and μ are evaluated at grid point (i,j), i.e. $\lambda_{i,j} = \lambda(\mathbf{X}_{i,j})$.

5. Evaluate the components of the nominal stress as $(S_{\alpha k})_{i,j} = (\Sigma_{\alpha\beta})_{i,j}(F_{k\beta})_{i,j}$.

6. Determine the momentum fluxes in the ξ and η directions,

$$\left(\widehat{\mathbf{S}_1}\right)_{i,j} = (J^{-1})_{i,j}\begin{bmatrix} (S_{11})_{i,j}(\partial\xi/\partial X)_{i,j} + (S_{21})_{i,j}(\partial\xi/\partial Y)_{i,j} \\ (S_{12})_{i,j}(\partial\xi/\partial X)_{i,j} + (S_{22})_{i,j}(\partial\xi/\partial Y)_{i,j} \end{bmatrix},$$

$$\left(\widehat{\mathbf{S}_2}\right)_{i,j} = (J^{-1})_{i,j}\begin{bmatrix} (S_{11})_{i,j}(\partial\eta/\partial X)_{i,j} + (S_{21})_{i,j}(\partial\eta/\partial Y)_{i,j} \\ (S_{12})_{i,j}(\partial\eta/\partial X)_{i,j} + (S_{22})_{i,j}(\partial\eta/\partial Y)_{i,j} \end{bmatrix},$$

where again we use the discrete metric terms. The discrete Jacobian $(J^{-1})_{i,j}$ is calculated from the discrete metric terms as shown earlier in (7).

7. The derivatives of the flux vectors with respect to the computational coordinates are obtained with the 6th order central scheme, e.g. for the ξ-derivative,

$$\left(\frac{\partial\widehat{\mathbf{S}_1}}{\partial\xi}\right)_{i,j} \approx (Q_\xi\widehat{\mathbf{S}_1})_{i,j} = -\frac{1}{60}(\widehat{\mathbf{S}_1})_{i-3,j} + \frac{3}{20}(\widehat{\mathbf{S}_1})_{i-2,j} - \frac{3}{4}(\widehat{\mathbf{S}_1})_{i-1,j} + \\ \frac{3}{4}(\widehat{\mathbf{S}_1})_{i+1,j} - \frac{3}{20}(\widehat{\mathbf{S}_1})_{i+2,j} + \frac{1}{60}(\widehat{\mathbf{S}_1})_{i+3,j}.$$

8. The right hand side of the momentum equation is calculated as

$$\dot{\boldsymbol{\psi}}_{i,j} = \frac{1}{(J^{-1})_{i,j}\rho_0}\left[(Q_\xi\widehat{\mathbf{S}_1})_{i,j} + (Q_\eta\widehat{\mathbf{S}_2})_{i,j}\right].$$

Time integration

Both the Navier–Stokes (12) and the Lagrangean field equations (10) can be written in the form $\dot{\mathbf{\Phi}}^i = \mathbf{f}^i(t, \mathbf{\Phi}^i)$ with $\mathbf{\Phi}^{\mathrm{s}} = (\boldsymbol{\phi}, \boldsymbol{\psi})$ and $\mathbf{\Phi}^{\mathrm{f}} = \hat{\mathbf{U}}'$, where $i = \mathrm{s}$ and $i = \mathrm{f}$ stand for structure and fluid, respectively. The semi-discrete equations can be formulated as a 4th order explicit Runge–Kutta scheme for both fields with a time step Δt as

$$\begin{aligned}
\mathbf{k}_1 &= \mathbf{f}^i(t_n, \mathbf{\Phi}^{i,n}) \\
\mathbf{k}_2 &= \mathbf{f}^i\left(t_n + \frac{\Delta t}{2}, \mathbf{\Phi}^{i,n} + \frac{\Delta t}{2}\mathbf{k}_1\right) \\
\mathbf{k}_3 &= \mathbf{f}^i\left(t_n + \frac{\Delta t}{2}, \mathbf{\Phi}^{i,n} + \frac{\Delta t}{2}\mathbf{k}_2\right) \\
\mathbf{k}_4 &= \mathbf{f}^i(t_n + \Delta t, \mathbf{\Phi}^{i,n} + \Delta t\mathbf{k}_3) \\
\mathbf{\Phi}^{i,n+1} &= \mathbf{\Phi}^{i,n} + \frac{\Delta t}{6}(\mathbf{k}_1 + 2\mathbf{k}_2 + 2\mathbf{k}_3 + \mathbf{k}_4)
\end{aligned}$$

where $\mathbf{\Phi}^{i,n}$ is the solution at the old time level n for field i.

Verification of structure method

Method of manufactured solution

An analytical test case for time-dependent problems in hyperelasticity is hard to find. Thus, for verification of the implemented techniques, the method of manufactured solution is used. The idea of the method is to construct a solution somewhat arbitrarily and insert it into the equations to be solved, without any boundary conditions. Since the constructed solution does not, in general, satisfy the equations, one ends up with a nonzero source term. If this source term is included in the original equations, the constructed solution must satisfy the original equation with the source term. To see how this works, rewrite the field equations (1) as

$$\ddot{\boldsymbol{\phi}} - \mathbf{Div}(\mathbf{S}(\boldsymbol{\phi}))/\rho_0 = 0 \tag{14}$$

where $\mathbf{Div}$ is the divergence in reference coordinates. Now construct explicitly an arbitrary solution $\boldsymbol{\varphi}(\mathbf{X}, t)$ and insert it into the left hand side of (14) to obtain $\ddot{\boldsymbol{\varphi}} - \mathbf{Div}(\mathbf{S}(\boldsymbol{\varphi}(\mathbf{X}, t))) = \mathbf{R}(\mathbf{X}, t)$ where $\mathbf{R}$ is a residual source term. Thus, $\boldsymbol{\varphi}$ satisfies the PDE

$$\ddot{\boldsymbol{\phi}} - \mathbf{Div}(\mathbf{S}(\boldsymbol{\phi}))/\rho_0 = \mathbf{R}(\mathbf{X}, t). \tag{15}$$

The source term $\mathbf{R}$ can be evaluated analytically for a given deformation $\boldsymbol{\varphi}$ by means of a symbolic mathematical tool such as Maple.

Test cases

The manufactured solution can be chosen in many different ways, but on physical grounds, it is reasonable to require that $\det \mathbf{F} > 0$ so that the physical domain (current configuration) does not overlap itself. Keeping this requirement in mind, the following test case is considered:

The reference configuration $\mathbf{X}$ is a square occupying the region $-1 \leq X, Y \leq 1$. The deformation is chosen such that the square changes size according to $\varphi(\mathbf{X}, t) = \frac{\mathbf{X}}{2}\sin \omega t$, i.e. at $\omega t = \pi/2$, the square has increased its size to $-3/2 \leq x, y \leq 3/2$ where $(x, y) = (X, Y) + \boldsymbol{\varphi}$. The neo-Hookean material (4) model is used.

Error analysis

Define the error in the discrete solution $\boldsymbol{\phi}_{i,j}$, at a certain time level, as the l_2 norm of the error

$$e = \left[\sum_{i,j} \Delta A_{i,j} |\boldsymbol{\phi}_{i,j} - \boldsymbol{\varphi}_{i,j}|^2 \right]^{1/2}$$

where $\boldsymbol{\varphi}_{i,j} = \boldsymbol{\varphi}(\mathbf{X}_{i,j}, t)$ is the analytical (constructed) solution evaluated at grid point (i, j) and $\Delta A_{i,j}$ is the cell volume (area) J^{-1} associated with grid point (i, j) in the reference configuration.

Verification of time integration

The source term for the test case with given deformation is $\mathbf{R}(\mathbf{X}, t) = -\omega^2 \frac{\mathbf{X}}{2} \sin(\omega t)$. It can be shown that the contribution from the stress tensor vanishes for the neo-Hookean material. The divergence of the stress in the material also vanishes, so the equation being solved is in fact just $\ddot{\boldsymbol{\phi}} = R(\mathbf{X}, t)$. Choosing $\omega = \pi$ and evaluating the solution at $t = 1$ where the analytical solution is $\boldsymbol{\phi}(\mathbf{X}, t = 1) = \boldsymbol{\varphi}(\mathbf{X}, t = 1) = \mathbf{0}$ for different time steps yields the results shown in table 1. The 4th order convergence of the Runge–Kutta scheme is evident. The grid spacing is insignificant here, since each point is decoupled from the others.

Comparison with Abaqus/Explicit

The test case only verified the time integration. To verify the space discretization and the boundary conditions, we consider a square reference domain $-1/2 \leq X, Y \leq 1/2$ for a body where three segments of the boundary are fixed in space and the fourth (top) is subjected to a time-dependent fluid pressure load, see fig. 5(a). When simulating this simple test case, one can ask, for example, what is the y-displacement of the midpoint on the top boundary, as a function of time? This question was investigated using both the previously described finite difference method and Abaqus, a commercial finite-element analysis package developed by Simulia [4].

Δt	e	Order
$1/32$	9.1143×10^{-9}	
$1/64$	5.6952×10^{-10}	4.0003
$1/128$	3.5593×10^{-11}	4.0001
$1/256$	2.2244×10^{-12}	4.0001
$1/512$	1.3921×10^{-13}	3.9981
$1/1024$	8.8033×10^{-15}	3.9831
$1/2048$	6.2144×10^{-16}	3.8244

Table 1: Error as a function of time step for the pulsating square case at time $t = 1$ and $\omega = \pi$.

The material model was the neo-Hookean material (4) with dimensionless Lamé parameters $\mu = 1, \lambda = 1$ and density $\rho = 1$. The time-dependent pressure on the top boundary was $P(t) = \sin^2(\pi t/4)$. The input parameters for Abaqus need to be given in the form $C_{10} = \mu/2$ and $D_1 = 2/\kappa$ where $\kappa = (3\lambda + 2\mu)/3$. For the finite-difference simulation, a 121×121 grid was used and a sufficiently small time step so that time integration errors were not dominant. For Abaqus, an unstructured mesh with 3206 linear plane-stress triangular elements was used. The results shown in figure 5(c) indicate a good agreement between the two analyses. The time-dependent behaviour of the displacement is captured well, both in terms of amplitude and phase. This indicates that the traction boundary condition (13) is handled correctly.

Additionally, as a test for the coordinate transformation, a more general domain was considered. For the case of a simple square, the coordinate transformation was $X = \xi - 1/2, Y = \eta - 1/2$ where ξ and η are computational coordinates $0 \leq \xi, \eta \leq 1$. Consider now the transformation $X(\xi, \eta) = \xi - 1/2 + d(\xi, \eta)$, $Y(\xi, \eta) = \eta - 1/2 + d(\xi, \eta)$ with $d(\xi, \eta) = 0.08 \sin(2\pi(\xi -$

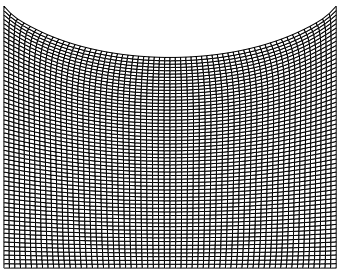

(a) Geometry for the pressure-loaded square test case. The left, right and bottom boundaries are fixed. The top boundary is loaded with a time-dependent pressure.

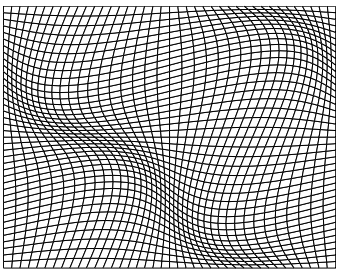

(b) Distorted grid.

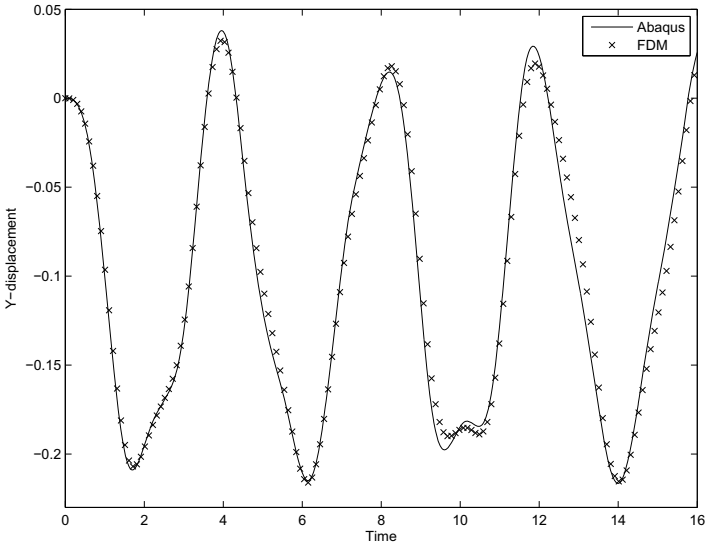

(c) Comparison of y-displacement of midpoint on top boundary of figure 5(a) in Abaqus/Explicit (–) vs. finite difference method ($\times$) for a square geometry with pressure load, neo-Hookean material.

Figure 5: Geometry and results for test case

$1/2))\sin(2\pi(\eta - 1/2))$. The domain is still a square, but the internal grid lines are no longer parallel, as seen in fig. 5(b). Computation on the distorted grid yields the same results as on the Cartesian grid.

Results

Geometry

The initial geometry for the vocal folds is here based on the geometry used in [34] for an oscillating glottis with a given time dependence. The initial shape of the vocal tract including the vocal fold is given as

$$r_w(x) = \frac{D_0 - D_{\min}}{4}\tanh s + \frac{D_0 + D_{\min}}{4}, \tag{16}$$

where r_w is the is the half height of the vocal tract, $D_0 = 5D_g$ is the height of the channel, $D_g = 4$ mm is the average glottis height, $D_{\min} = 2$ mm is the minimum glottis height, $s = b|x|/D_g - bD_g/|x|$, $c = 0.42$ and $b = 1.4$. For $-2D_g \leq x \leq 2D_g$, the function (16) describes the curved parts of the reference configuration for the top and bottom (with a minus sign) vocal folds.

Vocal fold material parameters

The density in the reference configuraiton is $\rho_0 = 1043\,\mathrm{kg/m^3}$, corresponding to the measured density of vocal fold tissue as reported by [10]. The Poisson ratio was chosen as $\nu = 0.47$ for the whole tissue, corresponding to a nearly incompressible material with $\nu = 0.5$ being the theoretical incompressible limit. A two-layer model for the vocal folds was used so that the shear modulus varied smoothly[1] from $\mu_\mathrm{c} = 3.5\,\mathrm{kPa}$ in the cover to $\mu_\mathrm{l} = 4.4\,\mathrm{kPa}$ in the ligament. The Lamé parameter λ, as a function of space, was then obtained as $\lambda = 2\mu\nu/(1 - 2\nu)$. The compressible neo-Hookean material model (4) was used.

Fluid model

We used a Reynolds number of 3000 based on the average glottis height $D_g = 0.004\,\mathrm{m}$ and an assumed average velocity in the glottis of $U_m = 40\,\mathrm{m/s}$. We used these particular values in order to be able to compare with previously published results by Zhao *et al.* [34, 32] and by ourselves [13, 14]. The Prandtl number was set to 1.0, and the Mach number was 0.2, based on the assumed average velocity and the speed of sound. We deliberately used a lower value for the speed of sound, $c_0 = 200\,\mathrm{m/s}$ in order to speed up the computations. The air density was $1.3\,\mathrm{kg/m^3}$ and the atmospheric pressure was $p_\mathrm{atm} = 101325\,\mathrm{Pa}$. The equation of state was the perfect gas law, and we assumed a Newtonian fluid. At the inlet, we imposed the acoustic pressure $p_\mathrm{acoustic} = p - p_\mathrm{atm} = 2736\,\mathrm{Pa}$, a typical lung pressure during phonation. The outlet pressure was set to atmospheric pressure, i.e. $p - p_\mathrm{atm} = 0\,\mathrm{Pa}$.

If we would not impose any asymmetry in the system, the solution should be symmetric with respect to the centerline at all times. However, this symmetric flow field is not stable, i.e. a small perturbation on one side would cause an asymmetry to build up and never go away (this was seen in our numerical experiments). Also, since the flow is not symmetric in nature, we chose to impose a non-symmetric pressure profile at the inlet by multiplying the given inlet acoustic pressure $p - p_\mathrm{atm}$ with a space varying factor $(1 + 0.025\sin(2\pi\eta))$ where η is a coordinate going from $\eta = 0$ at the lower boundary to $\eta = 1$ at the top boundary.

[1] $\mu(\eta) = \mu_\mathrm{average} + \Delta\mu\tanh(-4.5(\eta - 0.5))$, where $\mu_\mathrm{average} = (\mu_\mathrm{l} + \mu_\mathrm{c})/2$, $\Delta\mu = (\mu_\mathrm{l} - \mu_\mathrm{c})/2$ and η is a coordinate going from 0 in the ligament to 1 in the cover.

Numerical simulation

The computational domain is shown in figure 6 with the fluid domain in the middle, between the two independent structuree domains. The inflow boundary is to the left and the outflow is to the right. The part of the fluid boundary that is not in contact with the structure is a fixed no-slip adiabatic wall. The fluid-structure interface is a no-slip adiabatic wall which is allowed to deform due to the structure motion.

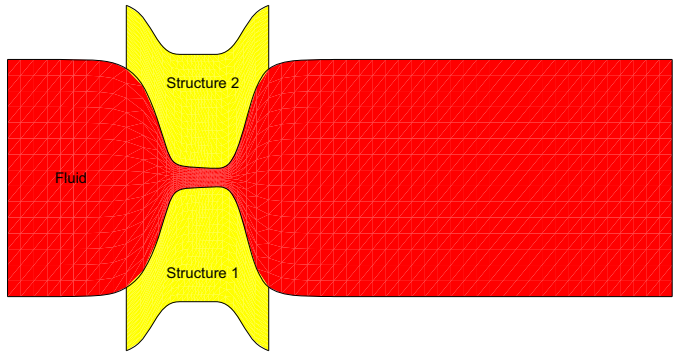

Figure 6: Sketch showing the computational domain for the fluid and the two structure domains.

Both fluid and structure used the same set of variables for nondimensionalization and the same time step was used for both fields so that the two solutions are always at the same time level. The structure grid consisted of 81×61 points for each vocal fold, i.e. for the upper and the lower vocal folds, and the fluid domain was 241×61 points. The time step was determined by the stability condition for the fluid discussed above, which was satisfied here by requiring $CFL \leq 1$. Since the fluid domain changes with time, the CFL condition puts a stricter constraint on the time step when the glottis is nearly closed. The solution was marched in time with given initial and boundary conditions to dimensional time $t = 20\,\mathrm{ms}$ or 416948 time steps, implying an average dimensional time step of $\Delta t = 48\,\mathrm{ns}$.

Figures 7 and 8 show results for the vorticity and pressure at certain time instants. Initially, the flow is symmetric with two start-up vortices followed by an elongated vortical structure on each side of the centerline. After the start-up vortices leave the domain, the elongated structure becomes unstable and breaks up into smaller circular vortices. As expected, the pressure is lowest inside the vortices. The observed frequency of the oscillation is about $80\,\mathrm{Hz}$, which is close to the typical frequencies that occur in phonation, i.e. $100\,\mathrm{Hz}$ for men and $200\,\mathrm{Hz}$ for women.

Conclusions

A solver for structural dynamics has been developed using a high order finite difference method to simulate the behavior of biological tissues. This new structural solver has been coupled to an existing compressible flow solver to simulate the fluid-structure interaction that occurs during phonation. The key features of this approach are high order differencing schemes on structured grids and matching grid points at the interface. The structural solver is verified with respect to a test case using the method of manufactured solution and by comparison with a commercial software package.

Our 2D model for the vocal folds and the air flow in the vocal tract proves to be able to capture

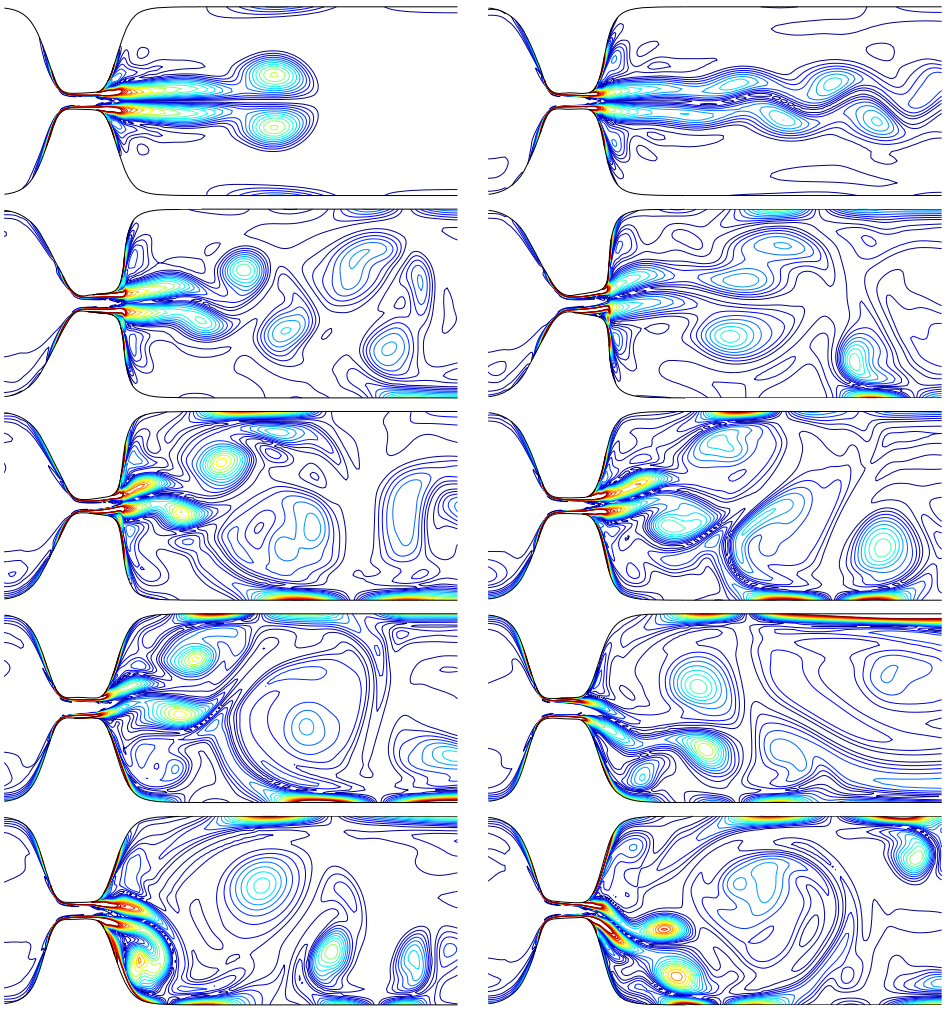

Figure 7: Vorticity contours at $2\,\mathrm{ms}$ intervals. Top left subplot is the vorticity at $t = 2\,\mathrm{ms}$, top right is at $t = 4\,\mathrm{ms}$ and so on up to $t = 20\,\mathrm{ms}$ (lower right). There are 20 equally spaced contour lines between $\omega = 0\,\mathrm{s}^{-1}$ and $\omega = 5 \times 10^4\,\mathrm{s}^{-1}$ in each subplot.

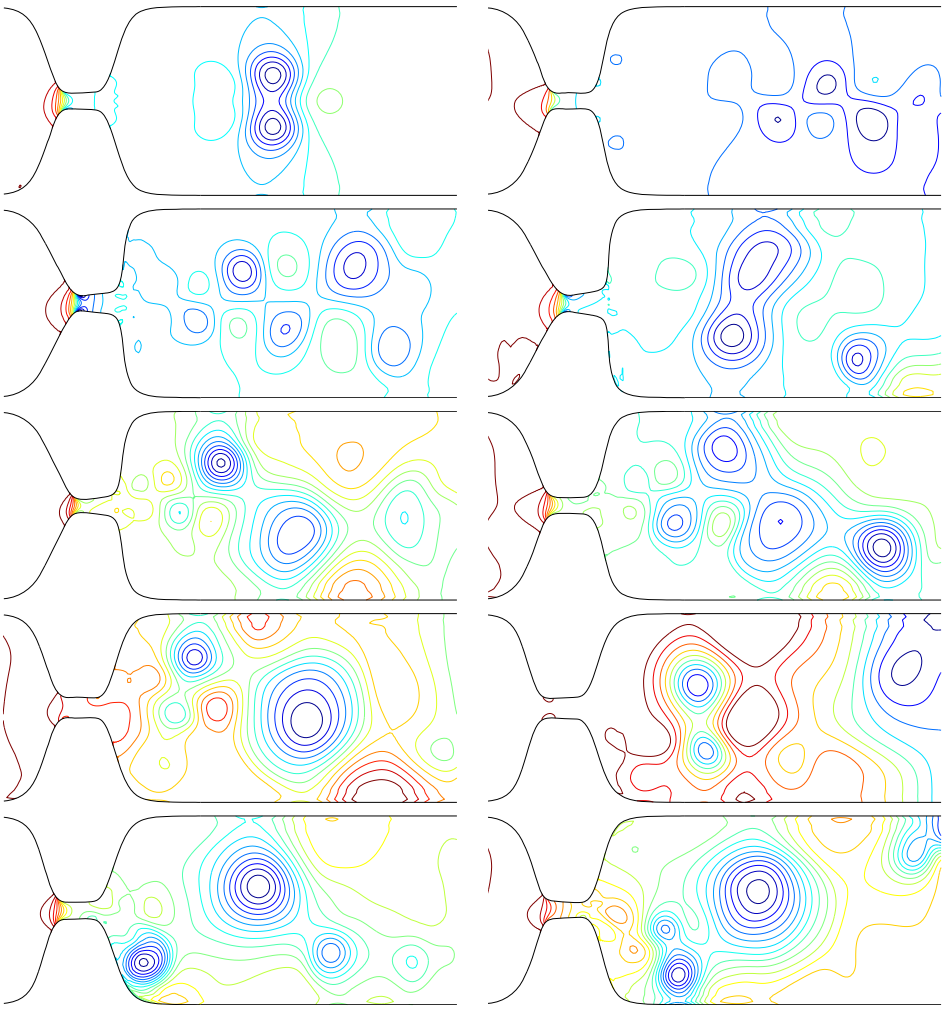

Figure 8: Pressure contours at $2\,\mathrm{ms}$ intervals. Top left image is the pressure at $t = 2\,\mathrm{ms}$, top right is at $t = 4\,\mathrm{ms}$ and so on up to $t = 20\,\mathrm{ms}$ (lower right). There are 20 equally spaced contour lines between $p_{\mathrm{acoustic}} = -3546\,\mathrm{Pa}$ and $p_{\mathrm{acoustic}} = 2837\,\mathrm{Pa}$ in each subplot, where p_{acoustic} is the pressure deviation from the atmospheric pressure, here $p_{\mathrm{atm}} = 101325\,\mathrm{Pa}$ (at the outlet).

the self-sustained pressure-driven oscillations and vortex generation in the glottis. The simulated frequency of $80\,\mathrm{Hz}$ is close to $100\,\mathrm{Hz}$, typical for men.

Acknowledgements

The authors thank Bjørn Skallerud, Paul Leinan and Victorien Prot at the Department of Structural Engineering, NTNU for valuable discussions on structure model and Abaqus support. The current research has been funded by the Swedish Research Council under the project "Numerical Simulation of Respiratory Flow".

References

[1] F. Alipour, D.A. Berry, and I.R. Titze. A finite-element model of vocal-fold vibration. *J. Acoust. Soc. Am.*, 108(6):3003 – 3012, 2000.

[2] F. Alipour and R.C. Scherer. Vocal fold bulging effects on phonation using a biophysical computer model. *J. Voice*, 14(4):470 – 483, 2000.

[3] F. Alipour and I.R. Titze. *Combined simulation of two-dimensional airflow and vocal fold vibration*. Ed. P. Davis and N. Fletcher, Singular Publishing Group, San Diego, 1996.

[4] Dassault Systémes Simulia Corp., Providence, RI, USA. *Abaqus: Analysis User's Manual, Version 6.8*, 2008.

[5] J. Degroote, P. Bruggeman, R. Haelterman, and J. Vierendeels. Stability of a coupling technique for partitioned solvers in FSI applications. *Computers and Structures*, 86:2224 – 2234, 2008.

[6] J.L. Flanagan and L. Landgraf. Self-oscillating source for vocal tract synthesizers. *IEEE Trans. Audio Electroacoust. AU*, 16:57 – 64, 1968.

[7] J.B. Grotberg and O.E. Jensen. Biofluid mechanics in flexible tubes. *Annu. Rev. Fluid Mech*, 36:121 – 147, 2004.

[8] B. Gustafsson. *High order difference methods for time-dependent PDE*. Springer-Verlag Berlin Heidelberg, 2008.

[9] B. Gustafsson, H.-O. Kreiss, and J. Oliger. *Time Dependent Problems and Difference Methods*. John Wiley & Sons, New York, 1995.

[10] E.J. Hunter, I.R. Titze, and F. Alipour. A three-dimensional model of vocal fold abduction/adduction. *J. Acoust. Soc. Am.*, 115(4), 2004.

[11] K. Kormann and M. Kronbichler. High order finite difference approximations for parabolic and hyperbolic-parabolic problems with variable coefficients. Project report, Department of Information Technology, Uppsala University, 2006.

[12] H.O. Kreiss and L. Wu. On the stability definition of difference approximations for the initial boundary value problem. *Applied Numer. Math.*, 12:213 – 227, 1993.

[13] M. Larsson. Numerical Simulation of Human Phonation, Master Thesis, Uppsala University, Department of Information Technology, 2007.

[14] M. Larsson and B. Müller. Numerical simulation of confined pulsating jets in human phonation. *Computers & Fluids, In Press*, 2008.

[15] H. Luo, R. Mittal, X. Zheng, S.A. Bielamowicz, R.J. Walsh, and J.K. Hahn. An immersed-boundary method for flow - structure interaction in biological systems with application to phonation. *Journal of Computational Physics*, 227:9303 – 9332, 2008.

[16] K. Mattsson and J. Nordström. Finite difference approximations of second derivatives on summation by parts form. *J. Comput. Physics*, 199:503 – 540, 2004.

[17] B. Müller. Linear stability condition for explicit Runge–Kutta methods to solve the compressible Navier–Stokes equations. *Mathematical Methods in the Applied Sciences*, 12:139 – 151, 1990.

[18] B. Müller. Computation of compressible low Mach number flow, Habilitation Thesis, ETH Zürich, 1996.

[19] B. Müller. High order numerical simulation of aeolian tones. *Computers & Fluids*, 37(4):450 – 462, 2008.

[20] R.W. Ogden. *Non-linear elastic deformations*. Ellis Horwood Limited, 1984.

[21] R.W. Ogden. Nonlinear elasticity and fibrous structure in arterial wall mechanics. Lecture Notes for Summer School on Modeling and Computation in Biomechanics held at Graz University of Technology, Austria, 2008.

[22] T.J. Poinsot and S.K. Lele. Boundary conditions for direct simulations of compressible viscous flows. *J. Comput. Physics*, 101:104 – 129, 1992.

[23] M. De Oliveira Rosa, J.C. Pereira, M. Grellet, and A. Alwan. A contribution to simulating a three-dimensional larynx model using the finite element method. *J. Acoust. Soc. Am.*, 114:2893 – 2905, 2003.

[24] D.H. Rudy and J.C. Strikwerda. A nonreflecting outflow boundary condition for subsonic Navier–Stokes calculations. *J. Comput. Physics*, 36:55 – 70, 1980.

[25] J. Sesterhenn, B. Müller, and H. Thomann. On the cancellation problem in calculating compressible low Mach number flows. *J. Comput. Physics*, 151:597 – 615, 1999.

[26] P. Šidlof. *Fluid-Structure interaction in human vocal folds*. PhD thesis, Charles University, Prague, 2007.

[27] B.H. Story and I.R. Titze. Voice simulation with a body-cover model of the vocal folds. *J. Acoust. Soc. Am.*, 97:1249 – 1260, 1995.

[28] B. Strand. Summation by parts for finite difference approximations for d/dx. *J. Comput. Physics*, 110:47 – 67, 1994.

[29] I.R. Titze. The human vocal cords: A mathematical model. Part I. *Phonetica*, 28:129 – 170, 1973.

[30] M.R. Visbal and D.V. Gaitonde. On the use of higher-order finite-difference schemes on curvilinear and deforming meshes. *J. Computat. Physics*, 181:155 – 185, 2002.

[31] M. Wang, J.B. Freund, and S.K. Lele. Computational prediction of flow-generated sound. *Annu. Rev. Fluid Mech.*, 38:483 – 512, 2006.

[32] C. Zhang, W. Zhao, S.H. Frankel, and L. Mongeau. Computational aeroacoustics of phonation, Part II: Effects of flow parameters and ventricular folds. *J. Acoust. Soc. Am.*, 112(5):2147 – 2154, 2002.

[33] W. Zhao, S.H. Frankel, and L. Mongeau. Numerical simulations of sound from confined pulsating axisymmetric jets. *AIAA Journal*, 39(10):1868 – 1874, 2001.

[34] W. Zhao, S.H. Frankel, and L. Mongeau. Computational aeroacoustics of phonation, Part I: Computational methods and sound generation mechanisms. *J. Acoust. Soc. Am.*, 112(5):2134 – 2146, 2002.

[35] R.J. Zwaan and B.B. Prananta. Fluid/structure interaction in numerical aeroelastic simulation. *Int. J. Non-Linear Mech.*, 37:987 – 1002, 2002.

PAPER 3

M. Larsson, B. Müller: Numerical Simulation of Fluid-Structure Interaction in Human Phonation: Application, Accepted for *Proceedings of ENUMATH 2009 Eighth European Conference on Numerical Mathematics and Advanced Applications*, Uppsala, Sweden, to be published by Springer 2010.

Numerical Simulation of Fluid–Structure Interaction in Human Phonation: Application

Martin Larsson and Bernhard Müller

Abstract Fluid-structure interaction in a simplified two-dimensional model of the larynx is considered in order to study human phonation. The flow is driven by an imposed pressure gradient across the glottis and interacts with the moving vocal folds in a self-sustained oscillation. The flow is computed by solving the 2D compressible Navier–Stokes equations using a high order finite difference method, which has been constructed to be strictly stable for linear hyperbolic and parabolic problems. The motion of the vocal folds is obtained by integrating the elastodynamic equations with a neo-Hookean constitutive model using a similar high order difference method as for the flow equations. Fluid and structure interact in a two-way coupling. In each time step at the fluid-structure interface, the structure provides the fluid with new no-slip boundary conditions and new grid velocities, and the fluid provides the structure with new traction boundary conditions.

1 Introduction

Fluid-structure interaction (FSI) occurs when a flexible structure interacts with a fluid. The fluid flow exerts a stress on the structure which causes it to deform, thereby generating a new geometry for the fluid flow. A direct consequence of FSI in the vocal tract is voice generation, where the motion of the soft tissue of the vocal folds interacts dynamically with the glottal airflow to produce sound. The self-sustained oscillations of the vocal folds can be explained by the Bernoulli principle which states that in the absence of gravity for inviscid incompressible steady flow,

Martin Larsson
Norwegian University of Science and Technology (NTNU), Department of Energy and Process Engineering (EPT), 7491 Trondheim, Norway, e-mail: martin.larsson@ntnu.no

Bernhard Müller
Norwegian University of Science and Technology (NTNU), Department of Energy and Process Engineering (EPT), 7491 Trondheim, Norway, e-mail: bernhard.muller@ntnu.no

the velocity v, pressure p and density ρ are related by $p+\rho v^2/2 = \text{const}$. The vocal folds being closed in their equilibrium position, initially at rest, are forced apart by the increasing lung pressure. As the air starts flowing, the velocity in the glottis increases and thus the pressure must decrease according to the Bernoulli principle. The pressure drop together with restoring elastic forces results in a closure of the vocal folds and a build-up of pressure. This cycle then repeats itself, driven only by the lung pressure. The computational challenge in aeroelastic simulations lies in dealing with unsteady flows at high Reynolds numbers, large deformations, moving interfaces, fluid-structure interaction and intrinsically 3D motion [1].

In this paper, we employ a high order finite difference approach based on summation by parts (SBP) operators [14, 3, 2] to solve the compressible Navier–Stokes equations and the elastodynamic equations using a neo-Hookean model. Fluid and structure interact in a two-way coupling. The approach has been tested for a 2D model of the larynx and the vocal folds.

2 Governing equations

2.1 Compressible Navier–Stokes equations

The perturbation formulation is used to minimize cancellation errors when discretizing the Navier–Stokes equations for compressible low Mach number flow [13, 9]. The 2D compressible Navier–Stokes equations in conservative form can be expressed in perturbation form as [10, 6]

$$\mathbf{U}'_t + \mathbf{F}^{c\prime}{}_x + \mathbf{G}^{c\prime}{}_y = \mathbf{F}^{v\prime}{}_x + \mathbf{G}^{v\prime}{}_y, \tag{1}$$

where the vector $\mathbf{U}'$ denotes the perturbation of the conservative variables with respect to the stagnation values. $\mathbf{U}'$ and the inviscid (superscript c) and viscous (superscript v) flux vectors are e.g. defined in [6].

General moving geometries are treated by a time dependent coordinate transformation $\tau = t$, $\xi = \xi(t,x,y)$, $\eta = \eta(t,x,y)$. The transformed 2D conservative compressible Navier–Stokes equations in perturbation form read [6]

$$\hat{\mathbf{U}}'_\tau + \hat{\mathbf{F}}'_\xi + \hat{\mathbf{G}}'_\eta = 0, \tag{2}$$

where $\hat{\mathbf{U}}' = J^{-1}\mathbf{U}'$, $\hat{\mathbf{F}}' = J^{-1}(\xi_t\mathbf{U}' + \xi_x(\mathbf{F}^{c\prime} - \mathbf{F}^{v\prime}) + \xi_y(\mathbf{G}^{c\prime} - \mathbf{G}^{v\prime}))$ and $\hat{\mathbf{G}}' = J^{-1}(\eta_t\mathbf{U}' + \eta_x(\mathbf{F}^{c\prime} - \mathbf{F}^{v\prime}) + \eta_y(\mathbf{G}^{c\prime} - \mathbf{G}^{v\prime}))$.

No-slip adiabatic wall boundary conditions and the Navier–Stokes Characteristic Boundary Conditions (NSCBC) technique by Poinsot and Lele in [12] are employed at the outflow [7]. At the inflow, pressure, temperature and velocity in the y-direction are imposed as $p = p_{\text{atm}} + \Delta p, T = T_0 = 310\,\text{K}$, and $v = 0$, respectively.

2.2 Elastodynamic equations

The governing equations for the motion of the structure are the Lagrangean field equations [11]

$$\frac{\partial S_{\alpha i}}{\partial X_\alpha} = \rho_0 \ddot{\phi}_i \tag{3}$$

where $\mathbf{X}$ are reference coordinates, $\mathbf{S}$ the nominal stress tensor, ϕ the displacement vector, ρ_0 the density in the reference configuration and the dots stand for partial time derivative at fixed $\mathbf{X}$.

As a constitutive model to obtain the nominal stress as a function of the displacement, the compressible neo-Hookean law

$$\mathbf{S} = \left[\mu \mathbf{1} + \left(\frac{\lambda}{2}\ln(\det(\mathbf{C})) - \mu\right)\mathbf{C}^{-1}\right]\mathbf{F}^{\mathrm{T}} \tag{4}$$

was used cf. e.g. [18]. Here, μ and λ are the Lamé parameters, $\mathbf{F} = \mathbf{1} + \nabla_{\mathbf{X}}\phi$ is the deformation gradient and $\mathbf{C} = \mathbf{F}^{\mathrm{T}}\mathbf{F}$ is the right Cauchy–Green strain tensor.

At boundaries where the structure is fixed in place, the displacement boundary condition $\phi(\mathbf{X},t) = \mathbf{0}$ is used, and on the fluid-structure interface the traction boundary condition $\mathbf{S}^{\mathrm{T}}\mathbf{N} = \mathbf{T}$ specifies the stress from the fluid on the structure boundary. If the stress tensor in the fluid is σ^{f}, then the force on the structure is [7, 8]

$$\mathbf{T} = \det(\mathbf{F})\sigma^{\mathrm{f}}\mathbf{F}^{-\mathrm{T}}\mathbf{N}. \tag{5}$$

By introducing a coordinate transformation from the reference configuration to computational coordinates $\xi = \xi(X_\alpha), \eta = \eta(X_\alpha)$ and a variable $\psi = \dot{\phi}$ for the velocity, the Lagrangean field equations can be expressed as a first-order system in time on an equidistant Cartesian grid

$$\begin{cases} \dot{\psi} = \frac{1}{J^{-1}\rho_0}\left[(\widehat{\mathbf{S}_1})_\xi + (\widehat{\mathbf{S}_2})_\eta\right] \\ \dot{\phi} = \psi \end{cases} \tag{6}$$

where ρ_0 is the material density in the reference configuration, $J^{-1} = |\partial(\xi,\eta)/\partial(X,Y$ is the Jacobian determinant of the coordinate transformation and $\widehat{\mathbf{S}_i} = J^{-1}\mathbf{S}^{\mathrm{T}}\nabla\xi_i$, $i = 1,2$, are transformed flux vectors.

The traction boundary condition specifies the momentum flux over the fluid-structure boundary. It can be shown, cf. [7, 8], that

$$\widehat{\mathbf{S}_2} = J^{-1}\sigma^{\mathrm{f}}\begin{pmatrix} F_{22} & -F_{21} \\ -F_{12} & F_{11} \end{pmatrix}\nabla\eta, \tag{7}$$

where $F_{i\alpha}$ are components of the deformation gradient $\mathbf{F}$, when the interface is at a line of constant η.

3 Fluid-structure interaction

3.1 Arbitrary Lagrangean–Eulerian (ALE) formulation

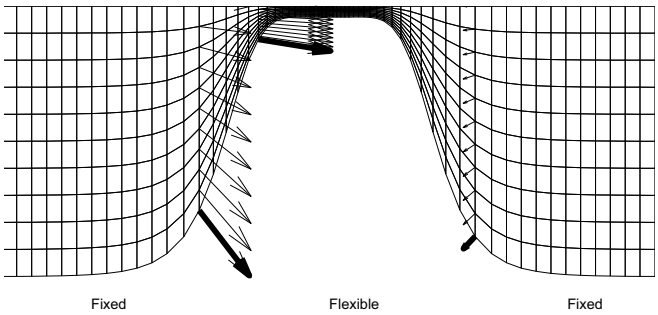

Fig. 1 The boundary of the fluid domain consists of fixed and flexible parts. The velocity at the boundary of the flexible part determines the internal grid point velocity. Only half domain shown.

The displacement of the structure interface determines the shape of the fluid domain and the structure velocity at the interface determines the internal grid point velocities in the fluid domain. The right and left boundaries of the fluid domain are the out- and inflow, respectively. The top and bottom parts of the fluid domain are bounded by the flexible vocal folds and the inner wall of the airpipe which is assumed to be rigid. As we do not assume symmetry, the motions of the two vocal folds are solved for individually. In our arbitrary Lagrangean–Eulerian (ALE) formulation, the positions and velocities of the grid points in the fluid domain are linearly interpolated from the positions and velocities of the structures at the interfaces. Figure 1 shows the given structure veolcities with bold arrows and the interpolated grid point velocities $\dot{x}, \dot{y}$ (thin arrows) for three grid lines.

To obtain the time derivative of J^{-1} as needed in (2), a geometric invariant [15] is used. This geometric conservation law states that $(J^{-1})_\tau + (J^{-1}\xi_t)_\xi + (J^{-1}\eta_t)_\eta = 0$. The time derivatives of the computational coordinates ξ, η can here be obtained from the grid point velocities $\dot{x}, \dot{y}$ as $\xi_t = -(\dot{x}\xi_x + \dot{y}\xi_y)$, $\eta_t = -(\dot{x}\eta_x + \dot{y}\eta_y)$ which can be seen by differentiating the transformation with respect to τ.

3.2 Description of fluid-structure interaction algorithm

First, we construct the fixed reference configuration for the structure and set the initial displacements and velocities to zero. The initial fluid domain is then uniquely determined by the reference boundary of the structure. We then take one time step for the fluid with imposed pressure boundary conditions at the inflow, zero initial conditions for the perturbation variables $\mathbf{U}'$ and adiabatic no-slip conditions, i.e.

$\mathbf{u} = 0$ and $\partial T/\partial n = 0$ on the wall. After the first fluid time step, the viscous fluid stress on the wall is calculated based on the new fluid velocities and pressures. These fluid stresses are passed on to the structure solver via the traction boundary condition (7). Using these boundary conditions, one time step is taken for the structure. The solution for the structure gives the velocities and displacements on the boundary, which in turn are used to generate the new fluid mesh and internal grid point velocities. This procedure is then repeated for each time step.

4 High order finite difference method

The summation by parts (SBP) operator Q is an approximation to the first spatial derivative. In the interior, Q corresponds to the standard 6th order explicit central operator, while Q is third order accurate at and near the boundaries. Through a special boundary treatment, SBP operators allow energy estimates for the discrete problems similar to the ones for the continuous problems that are approximated. Thus, SBP operators yield strictly stable schemes for general boundary conditions [14, 7]. The global order of accuracy of the present SBP operator Q is 4 [3, 2]. Second derivatives are approximated by applying the SBP operator Q twice. The classical fourth order explicit Runge-Kutta method is used for time integration. Spurious high wave number oscillations are suppressed by a sixth order explicit filter [10].

5 Results

The initial geometry for the vocal folds is here based on the geometry used in [17] for an oscillating glottis with a given time dependence. The initial shape of the vocal tract including the vocal fold is given as

$$r_w(x) = \frac{D_0 - D_{\min}}{4} \tanh s + \frac{D_0 + D_{\min}}{4}, \tag{8}$$

where r_w is the is the half height of the vocal tract, $D_0 = 5D_g$ is the height of the channel, $D_g = 4$ mm is the average glottis height, $D_{\min} = 2$ mm is the minimum glottis height, $s = b|x|/D_g - bD_g/|x|$, $c = 0.42$ and $b = 1.4$. For $-2D_g \leq x \leq 2D_g$, the function (8) describes the curved parts of the reference configuration for the top and bottom (with a minus sign) vocal folds.

5.1 Vocal fold material parameters

The density in the reference configuraiton is $\rho_0 = 1043\,\mathrm{kg/m^3}$, corresponding to the measured density of vocal fold tissue as reported by [4]. The Poisson ratio was

chosen as $\nu = 0.47$ for the whole tissue, corresponding to a nearly incompressible material with $\nu = 0.5$ being the theoretical incompressible limit. A two-layer model for the vocal folds was used so that the shear modulus varied smoothly from $\mu_c = 3.5\,\mathrm{kPa}$ in the cover to $\mu_l = 4.4\,\mathrm{kPa}$ in the ligament. The Lamé parameter λ, as a function of space, was then obtained as $\lambda = 2\mu\nu/(1-2\nu)$. A compressible neo-Hookean material model was used, cf. [7].

5.2 Fluid model

We used a Reynolds number of 3000 based on the average glottis height $D_g = 0.004\,\mathrm{m}$ and an assumed average velocity in the glottis of $U_m = 40\,\mathrm{m/s}$. We used these particular values in order to be able to compare with previously published results by Zhao *et al.* [17, 16] and by ourselves [5, 6]. The Prandtl number was set to 1.0, and the Mach number was 0.2, based on the assumed average velocity and the speed of sound. We deliberately used a lower value for the speed of sound, $c_0 = 200\,\mathrm{m/s}$ in order to speed up the computations. The air density was $1.3\,\mathrm{kg/m^3}$ and the atmospheric pressure was $p_{\mathrm{atm}} = 101325\,\mathrm{Pa}$. The equation of state was the perfect gas law, and we assumed a Newtonian fluid. At the inlet, we imposed a typical lung pressure during phonation with a small unsymmetric perturbance by setting the acoustic pressure to $p_{\mathrm{acoustic}} = p - p_{\mathrm{atm}} = (1 + 0.025\sin 2\pi\eta)2736\,\mathrm{Pa}$, where $\eta = 0$ at the lower edge and $\eta = 1$ at the upper edge of the inflow boundary. The outlet pressure was set to atmospheric pressure, i.e. $p - p_{\mathrm{atm}} = 0\,\mathrm{Pa}$.

5.3 Numerical simulation

Both fluid and structure used the same set of variables for nondimensionalization and the same time step was used for both fields so that the two solutions are always at the same time level. The structure grid consisted of 81×61 points for each vocal fold, i.e. for the upper and the lower vocal folds, and the fluid domain was 241×61 points. The time step was determined by the stability condition for the fluid, which was satisfied here by requiring $CFL \leq 1$. Since the fluid domain changes with time, the CFL condition puts a stricter constraint on the time step when the glottis is nearly closed. The solution was marched in time with given initial and boundary conditions to dimensional time $t = 20\,\mathrm{ms}$ or 416948 time steps, implying an average dimensional time step of $\Delta t = 48\,\mathrm{ns}$.

Figure 2 shows results for the vorticity at certain time instants. Initially, the flow is symmetric with two start-up vortices followed by an elongated vortical structure on each side of the centerline. After the start-up vortices leave the domain, the elongated structure becomes unstable and breaks up into smaller circular vortices. The observed frequency of the oscillation is about 80 Hz, which is close to the typical frequencies that occur in phonation, i.e. 100 Hz for men and 200 Hz for women.

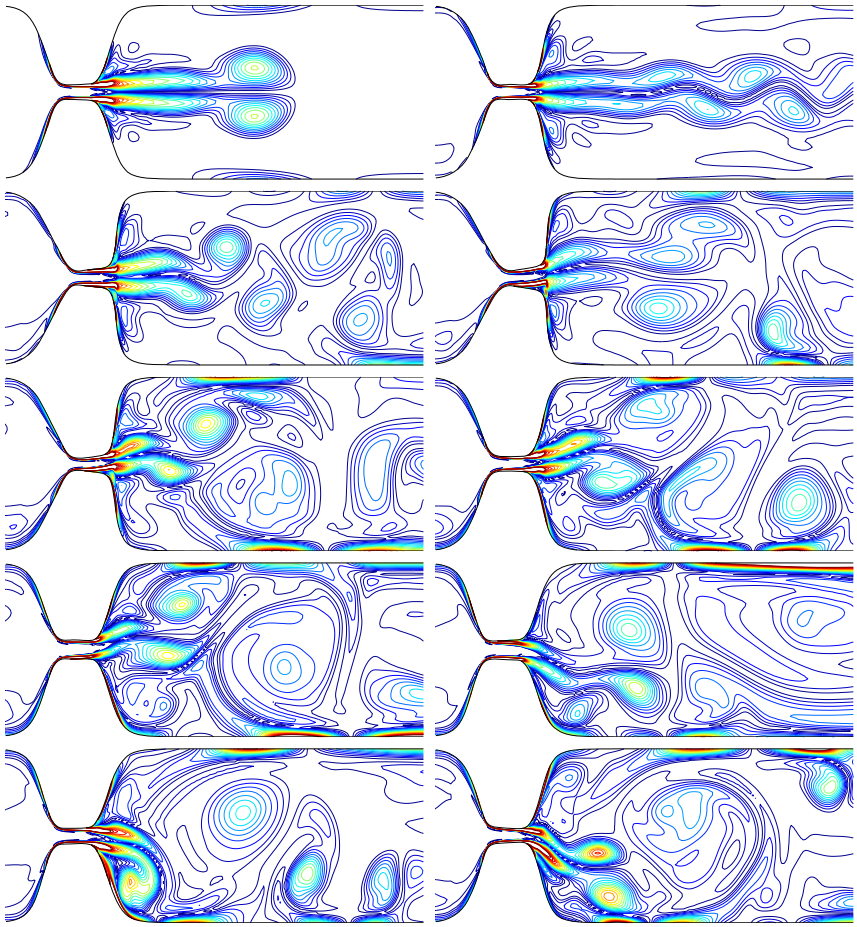

Fig. 2 Vorticity contours at 2 ms intervals. Top left subplot is the vorticity at $t = 2$ ms, top right is at $t = 4$ ms and so on up to $t = 20$ ms (lower right). There are 20 equally spaced contour lines between $\omega = 0\,\mathrm{s}^{-1}$ and $\omega = 5 \times 10^4\,\mathrm{s}^{-1}$ in each subplot.

6 Conclusions

Our 2D model for the vocal folds and the air flow in the vocal tract proves to be able to capture the self-sustained pressure-driven oscillations and vortex generation in the glottis. The simulated frequency of 80 Hz is close to 100 Hz, typical for men.

Acknowledgements The authors thank Bjørn Skallerud, Paul Leinan and Victorien Prot at the Department of Structural Engineering, NTNU for valuable discussions on the structure model and for Abaqus support. The current research has been funded by the Swedish Research Council under the project "Numerical Simulation of Respiratory Flow".

References

1. J.B. Grotberg and O.E. Jensen. Biofluid mechanics in flexible tubes. *Annu. Rev. Fluid Mech*, 36:121–147, 2004.
2. B. Gustafsson. *High order difference methods for time-dependent PDE*. Springer-Verlag Berlin Heidelberg, 2008.
3. B. Gustafsson, H.-O. Kreiss, and J. Oliger. *Time Dependent Problems and Difference Methods*. John Wiley & Sons, New York, 1995.
4. E.J. Hunter, I.R. Titze, and F. Alipour. A three-dimensional model of vocal fold abduction/adduction. *J. Acoust. Soc. Am.*, 115(4):1747–1759, 2004.
5. M. Larsson. *Numerical Simulation of Human Phonation*, Master Thesis, Uppsala University, Department of Information Technology, 2007.
6. M. Larsson and B. Müller. Numerical simulation of confined pulsating jets in human phonation. *Computers & Fluids*, 38:1375–1383, 2009.
7. M. Larsson and B. Müller. Numerical simulation of fluid-structure interaction in human phonation. In *B. Skallerud and H.I. Andersson, editors, MekIT 09 Fifth national conference on Computational Mechanics*, pages 261–280, Trondheim, Norway, 2009. Tapir Academic Press.
8. M. Larsson and B. Müller. Numerical simulation of fluid-structure interaction in human phonation: Verification of structure part. In *Proceedings of ICOSAHOM 09 International Conference on Spectral and High Order Methods*, Trondheim, Norway, 2009, to be published by Springer.
9. B. Müller. *Computation of compressible low Mach number flow*, Habilitation Thesis, ETH Zürich, 1996.
10. B. Müller. High order numerical simulation of aeolian tones. *Computers & Fluids*, 37(4):450–462, 2008.
11. R.W. Ogden. *Non-linear elastic deformations*. Ellis Horwood Limited, 1984.
12. T.J. Poinsot and S.K. Lele. Boundary conditions for direct simulations of compressible viscous flows. *J. Comput. Physics*, 101:104–129, 1992.
13. J. Sesterhenn, B. Müller, and H. Thomann. On the cancellation problem in calculating compressible low Mach number flows. *J. Comput. Physics*, 151:597–615, 1999.
14. B. Strand. Summation by parts for finite difference approximations for d/dx. *J. Comput. Physics*, 110:47–67, 1994.
15. M.R. Visbal and D.V. Gaitonde. On the use of higher-order finite-difference schemes on curvilinear and deforming meshes. *J. Computat. Physics*, 181:155–185, 2002.
16. C. Zhang, W. Zhao, S.H. Frankel, and L. Mongeau. Computational aeroacoustics of phonation, Part II. *J. Acoust. Soc. Am.*, 112(5):2147–2154, 2002.
17. W. Zhao, S.H. Frankel, and L. Mongeau. Computational aeroacoustics of phonation, Part I: Computational methods and sound generation mechanisms. *J. Acoust. Soc. Am.*, 112(5):2134–2146, 2002.
18. O.C. Zienkiewicz and R.L. Taylor. *The finite element method for solid and structural mechanics, 5th edition*. Elsevier Butterworth-Heinemann, 2000.

PAPER 4

M. Larsson, B. Müller: Numerical Simulation of Fluid-Structure Interaction in Human Phonation: Verification of Structure Part, Accepted for *Proceedings of ICOSAHOM 09 International Conference on Spectral and High Order Methods*, Trondheim, Norway, to be published as a special volume of the Lecture Notes in Computational Science and Engineering by Springer, 2010

Numerical Simulation of Fluid–Structure Interaction in Human Phonation: Verification of Structure Part

Martin Larsson and Bernhard Müller

Abstract A high order finite-difference method has been developed to model fluid–structure interaction during phonation in the human larynx. The motion of the vocal folds is obtained by solving the elastic equations while the airflow is modeled by solving the compressible Navier–Stokes equations. In this paper, we address the problem of obtaining time-stable solutions for the linear elastic equations.

1 Introduction

Fluid–structure interaction in the human larynx generates our voice [9, 5]. We have developed a high order difference method to simulate the interaction of compressible flow in the larynx with the elastic structure of the vocal folds [3]. This paper deals with obtaining time-stable solutions for the linear elastic wave equation in a first-order formulation, which form the basis for more advanced structure models.

When written as a system of first order equations, the stability theory which is well developed for hyperbolic systems, applies directly. The disadvantage compared with a second order formulation in time is the increased computational effort required for the additional variables. Our main motivation for using a first order formulation is, however, related to the application of fluid-structure interaction where the traction boundary condition dictates the stresses on the elastic body. In the first order formulation, the traction boundary condition can be easily formulated as a simple Dirichlet condition for a subset of the solution variables. Dirichlet boundary

Martin Larsson
Norwegian University of Science and Technology (NTNU), Department of Energy and Process Engineering (EPT), 7491 Trondheim, Norway, e-mail: martin.larsson@ntnu.no

Bernhard Müller
Norwegian University of Science and Technology (NTNU), Department of Energy and Process Engineering (EPT), 7491 Trondheim, Norway, e-mail: bernhard.muller@ntnu.no

conditions are not at all straight-forward to impose in a second order formulation [6].

2 Theory

The 2D linear elastic wave equation in first order form are

$$\begin{aligned} u_t &= (1/\rho) f_x + (1/\rho) g_y \\ v_t &= (1/\rho) g_x + (1/\rho) h_y \\ f_t &= (\lambda + 2\mu) u_x + \lambda v_y \\ g_t &= \mu v_x + \mu u_y \\ h_t &= \lambda u_x + (\lambda + 2\mu) v_y \end{aligned} \tag{1}$$

where u, v are the velocity components and f, g, h are the three independent components of the symmetric Cauchy stress tensor. The Lamé parameters λ, μ and the density ρ are here taken to be constant in space and time.

Introducing the solution vector q and coefficient matrices A and B allows us to write the linear elastic wave equation (1) as a first order hyperbolic system

$$q_t = A q_x + B q_y, \tag{2}$$

where $q = (u, v, f, g, h)^{\mathrm{T}}$. The wave speeds of the system are $c_s = \sqrt{\mu/\rho}$ and $c_p = \sqrt{(\lambda + 2\mu)/\rho}$, referred to as secondary (or shear) and primary wave velocity, respectively. For convenience, we also define the parameter $\alpha = (\lambda + 2\mu)/\lambda = c_p^2/(c_p^2 - 2c_s^2)$.

In order to obtain simultaneous approximation (SAT) terms (to be explained below) for the system, we need to transform the system to characteristic variables. This can indeed be done, since the system (2) is hyperbolic. Thus, there exists an invertible matrix $T(k)$ for all directions k in 2D such that $T^{-1}(k) P(k) T(k) = \Lambda(k)$, where $P(k) = k_1 A + k_2 B$. The diagonal real eigenvalue matrix $\Lambda(k)$ can be choosen such that the eigenvalues occur in descending order. For the x- and y-directions, we get the following characteristic variables for the system (2).

$$u^{(x)} = T_x^{-1} q = \frac{1}{2} \begin{bmatrix} \lambda u/c_p + f/\alpha \\ v + g/(\rho c_s) \\ -2f/\alpha + 2h \\ v - g/(\rho c_s) \\ -\lambda u/c_p + f/\alpha \end{bmatrix}, \quad u^{(y)} = T_y^{-1} q = \frac{1}{2} \begin{bmatrix} \lambda v/c_p + h/\alpha \\ u + g/(\rho c_s) \\ 2f - 2h/\alpha \\ u - g/(\rho c_s) \\ -\lambda v/c_p + h/\alpha \end{bmatrix}. \tag{3}$$

Note that we use the symbol u to refer to both the vector of characteristic variables and the first velocity component. The meaning of u should be clear from context. The transformation back to flow variables is given by $q = Tu$.

3 Summation by parts operators

The idea behind the summation by parts technique [8] is to construct a difference operator Q which satisfies a discrete analogue to the continuous integration by parts property. This is called a summation by parts (SBP) property and by the energy method (cf. e.g. [2]), the discrete problem then satisfies the same energy estimate as the continuous problem.

For diagonal norm matrices H, there exist difference operators Q accurate to order $\mathscr{O}(h^{2s})$ in the interior and $\mathscr{O}(h^s)$ near the boundaries for $s = 1, 2, 3$ and 4. These operators have an effective order of accuracy $\mathscr{O}(h^{s+1})$ in the entire domain. Explicit forms of such operators Q and norm matrices H have been derived by Strand [8]. For this study, we use an SBP operator based on the central sixth order explicit finite difference operator $(s = 3)$ which has been modified near the boundaries in order to satisfy the SBP property giving an effective $\mathscr{O}(h^4)$ order of accuracy in the whole domain.

With the injection method, numerical solutions with stable schemes can still exhibit a nonphysical growth in time which is not explained by the continuous equation. Simultaneous approximation terms (SAT) were devised to obtain time-stable solutions [1]. In this approach, a linear combination of the boundary condition and the differential equation is solved at the boundary instead of injecting the value at the end of each Runge–Kutta stage. This leads to a weak imposition of the physical boundary conditions. The imposition of SAT boundary conditions is accomplished by adding a term to the derivative operator, proportional to the difference between the value of the discrete solution u_N and the boundary condition to be fulfilled.

The strictly stable SAT method for a hyperbolic system in one space dimension with diagonal coefficient matrices was derived in [1] and is the basis for this work. The continuous 1D model problem is $u_t = \Lambda u_x$, $0 \le x \le 1$, with r unknowns and r equations and the coefficient matrix Λ is chosen such that the eigenvalues are in descending order, i.e. $\lambda_1 > \lambda_2 > ... > \lambda_k > 0 > \lambda_{k+1} > ... > \lambda_r$. We split the solution vector into two parts corresponding to positive and negative eigenvalues $\mathbf{u}^{\mathrm{I}} = (\mathbf{u}^{(1)}, ..., \mathbf{u}^{(k)})^{\mathrm{T}}$ and $\mathbf{u}^{\mathrm{II}} = (\mathbf{u}^{(k+1)}, ..., \mathbf{u}^{(r)})^{\mathrm{T}}$. For the variables in $\mathbf{u}^{\mathrm{I}}$ (each a grid function of length $N+1$) we have boundary conditions at $x = 1$, and for $\mathbf{u}^{\mathrm{II}}$ we need to specify boundary conditions at $x = 0$, as this is required for well-posedness.

Since we are here dealing with characteristic variables, we need to transform our physical boundary conditions to boundary conditions for the characteristic variables. This is done through the boundary functions $\mathbf{g}^{\mathrm{I}}(t) = (g^{(1)}(t), ..., g^{(k)}(t))$, $\mathbf{g}^{\mathrm{II}}(t) = (g^{(k+1)}(t), ..., g^{(r)}(t))$ and the coupling matrices R and L defined by

$$\mathbf{u}^{\mathrm{I}}(1,t) = R\mathbf{u}^{\mathrm{II}}(1,t) + \mathbf{g}^{\mathrm{I}}(t), \quad \mathbf{u}^{\mathrm{II}}(0,t) = L\mathbf{u}^{\mathrm{I}}(0,t) + \mathbf{g}^{\mathrm{II}}(t) \tag{4}$$

The SAT method is then:

$$\begin{aligned} \tfrac{d\mathbf{u}^{(i)}}{dt} &= \lambda_i Q\mathbf{u}^{(i)} - \lambda_i \tau \mathbf{S}^{(i)}(\mathbf{u}_N^{(i)} - (R\mathbf{u}^{\mathrm{II}})_N^{(i)} - g^{(i)}(t)), \quad 1 \le i \le k \\ \tfrac{d\mathbf{u}^{(i)}}{dt} &= \lambda_i Q\mathbf{u}^{(i)} + \lambda_i \tau \mathbf{S}^{(i)}(\mathbf{u}_0^{(i)} - (L\mathbf{u}^{\mathrm{I}})_0^{(i-k)} - g^{(i)}(t)), \quad k+1 \le i \le r \end{aligned} \tag{5}$$

where $\mathbf{S}^{(i)} = H^{-1}(0,0,...,1)^{\mathrm{T}}$ for $1 \leq i \leq k$ and $\mathbf{S}^{(i)} = H^{-1}(1,0,...,0)^{\mathrm{T}}$ for $k+1 \leq i \leq r$. Regarding the notation, $(R\mathbf{u}^{\mathrm{II}})_N^{(i)}$ should be interpreted as follows: $\mathbf{u}^{\mathrm{II}}$ is an $(r-k)\times 1$ vector where each component is a grid function of length $N+1$. Multiplying R (being a $k\times(r-k)$ matrix) with $\mathbf{u}^{\mathrm{II}}$ yields a new vector of grid functions ($k\times 1$ vector). Take the (i)th grid function in this vector and finally the Nth component in the resulting grid function. As shown in [1], the SAT method is both stable and time stable provided that

$$\frac{1-1\sqrt{1-|R||L|}}{|R||L|} \leq \tau \leq \frac{1+1\sqrt{1-|R||L|}}{|R||L|} \tag{6}$$

with the additional constraint that $|R||L| \leq 1$, where the matrix norm is defined as $|R| = \rho(R^T R)^{1/2}$ and ρ is the spectral radius.

4 Application to elastic wave equation

Now, we shall apply the general method outlined above to derive SAT expressions for boundary conditions on the velocity components. The vector of characteristic variables in the x-direction is given in equation (3), but henceforth we drop the superscript $^{(x)}$. The derivation for the y-direction is analogeous.

We let the grid functions $\mathbf{u}$ and $\mathbf{v}$ in 2D with points labeled $0 \leq i \leq N$ and $0 \leq j \leq M$ in the x- and y-directions, respectively, correspond to the solution variables u and v in the discretization of the linear elastic wave equation. We label the boundary $i = 0$ "left", $i = N$ "right", $j = 0$ "bottom", $j = M$ "top".

The boundary conditions for the velocity components in 2D are of the form $u(x = 0,y,t) = u_{\mathrm{left}}(y,t)$, i.e. a given function of time, which we write for the discrete variables as $u_{0,j}(t) = u_{\mathrm{left},j}(t)$, with similar notation for the other edges and the other solution variables. The SAT expressions, one for each spatial direction and for each solution variable, will also be grid functions.

We split the vector of characteristic variables into two smaller vectors corresponding to the positive and negative eigenvalues, omitting the characteristic with zero eigenvalue as the corresponding SAT expression will be zero,

$$u^{\mathrm{I}} = \frac{1}{2}\begin{bmatrix}(\lambda/c_p)u+(1/\alpha)f\\ v+(1/c_p\rho)g\end{bmatrix}, \quad u^{\mathrm{II}} = \frac{1}{2}\begin{bmatrix}v-(1/c_p\rho)g\\ (-\lambda/c_p)u+(1/\alpha)f\end{bmatrix}$$

and define the coefficient matrices $\Lambda^{\mathrm{I}} = \mathrm{diag}(c_p,c_s)$, $\Lambda^{\mathrm{II}} = \mathrm{diag}(-c_s,-c_p)$. The boundary functions g^{I}, g^{II}, and the matrices L and R are defined by the relations (4).

If we impose the boundary condition in the x-direction $u(x=1,t) = u_{\mathrm{right}}(t)$,$v(x=1,t) = v_{\mathrm{right}}(t)$, $u(x=0,t) = u_{\mathrm{left}}(t)$,$v(x=0,t) = v_{\mathrm{left}}(t)$, then the boundary matrices and functions are given by

$$R = \begin{bmatrix}0 & 1\\ -1 & 0\end{bmatrix},\ L = \begin{bmatrix}0 & -1\\ 1 & 0\end{bmatrix},\ g^{\mathrm{I}} = \begin{bmatrix}\lambda u_{\mathrm{right}}(t)/c_p\\ v_{\mathrm{right}}(t)\end{bmatrix},\ g^{\mathrm{II}}(t) = \begin{bmatrix}v_{\mathrm{left}}(t)\\ -\lambda u_{\mathrm{left}}(t)/c_p\end{bmatrix}.$$

In the y-direction, dictating $u(y=1,t)=u_{\text{top}}(t)$,$v(y=1,t)=v_{\text{top}}(t)$, $u(y=0,t)=u_{\text{bottom}}(t)$,$v(y=0,t)=v_{\text{bottom}}(t)$, we get, likewise

$$R=\begin{bmatrix}0 & 1\\ -1 & 0\end{bmatrix},\ L=\begin{bmatrix}0 & -1\\ 1 & 0\end{bmatrix},\ g^{\text{I}}=\begin{bmatrix}\lambda v_{\text{top}}(t)/c_p\\ u_{\text{top}}(t)\end{bmatrix},\ g^{\text{II}}(t)=\begin{bmatrix}u_{\text{bottom}}(t)\\ -\lambda v_{\text{bottom}}(t)/c_p\end{bmatrix}.$$

Corresponding expressions can be derived for boundary conditions on the stress components, but these are omitted here due to space limitations. We note that, as the spectral radius of both L and R is 1 in each case, the inequalities (6) lend no other choice than $\tau=1$ for time-stability.

Using the definition (5) with the expressions above, the SAT terms are first obtained for the characteristic variables, and then for the flow variables by applying the transformation matrices T for the x- and y-directions. The resulting expressions are

$$\begin{aligned}
\overline{\text{SAT}}^{x}_{i,j,1} &= -c_p\tau h_{00}^{-1}\left[\delta_{iN}\left(u_{N,j}-u_{\text{right},j}(t)\right)+\delta_{i0}\left(u_{0,j}-u_{\text{left},j}(t)\right)\right]\\
\overline{\text{SAT}}^{x}_{i,j,2} &= -c_s\tau h_{00}^{-1}\left[\delta_{iN}\left(v_{N,j}-v_{\text{right},j}(t)\right)+\delta_{i0}\left(v_{0,j}-v_{\text{left},j}(t)\right)\right]\\
\overline{\text{SAT}}^{x}_{i,j,3} &= -(\lambda+2\mu)\tau h_{00}^{-1}\left[\delta_{iN}\left(u_{N,j}-u_{\text{right},j}(t)\right)-\delta_{i0}\left(u_{0,j}-u_{\text{left},j}(t)\right)\right]\\
\overline{\text{SAT}}^{x}_{i,j,4} &= -\mu\tau h_{00}^{-1}\left[\delta_{iN}\left(v_{N,j}-v_{\text{right},j}(t)\right)-\delta_{i0}\left(v_{0,j}-v_{\text{left},j}(t)\right)\right]\\
\overline{\text{SAT}}^{x}_{i,j,5} &= -\lambda\tau h_{00}^{-1}\left[\delta_{iN}\left(u_{N,j}-u_{\text{right},j}(t)\right)-\delta_{i0}\left(u_{0,j}-u_{\text{left},j}(t)\right)\right]
\end{aligned}\tag{7}$$

$$\begin{aligned}
\overline{\text{SAT}}^{y}_{i,j,1} &= -c_s\tau h_{00}^{-1}\left[\delta_{jM}\left(u_{i,M}-u_{\text{top},i}(t)\right)+\delta_{j0}\left(u_{i,0}-u_{\text{bottom},i}(t)\right)\right]\\
\overline{\text{SAT}}^{y}_{i,j,2} &= -c_p\tau h_{00}^{-1}\left[\delta_{jM}\left(v_{i,M}-v_{\text{top},i}(t)\right)+\delta_{j0}\left(v_{i,0}-v_{\text{bottom},i}(t)\right)\right]\\
\overline{\text{SAT}}^{y}_{i,j,3} &= -\lambda\tau h_{00}^{-1}\left[\delta_{jM}\left(v_{i,M}-v_{\text{top},i}(t)\right)-\delta_{j0}\left(v_{i,0}-v_{\text{bottom},i}(t)\right)\right]\\
\overline{\text{SAT}}^{y}_{i,j,4} &= -\mu\tau h_{00}^{-1}\left[\delta_{jM}\left(u_{i,M}-u_{\text{top},i}(t)\right)-\delta_{j0}\left(u_{i,0}-u_{\text{bottom},i}(t)\right)\right]\\
\overline{\text{SAT}}^{y}_{i,j,5} &= -(\lambda+2\mu)\tau h_{00}^{-1}\left[\delta_{jM}\left(v_{i,M}-v_{\text{top},i}(t)\right)-\delta_{j0}\left(v_{i,0}-v_{\text{bottom},i}(t)\right)\right],
\end{aligned}\tag{8}$$

where δ_{ij} is the Dirac delta function, i.e. $\delta_{ij}=1$ if $i=j$ and 0 otherwise. The overline stands for physical (flow) variables.

5 Discretization

We consider the mapping $x=x(\xi,\eta)$, $y=y(\xi,\eta)$ and introduce an equidistant computational grid with coordinates $\xi_i, i=0,...,N$, $\eta_j, j=0,...,M$. The Jacobian determinant of the transformation is given by $J^{-1}=x_\xi y_\eta - x_\eta y_\xi$. The linear elastic wave equation can then be written

$$\hat{q}_t=(\hat{A}\hat{q})_\xi+(\hat{B}\hat{q})_\eta \tag{9}$$

where the hats signify that the quantities are in transformed coordinates, i.e. $\hat{q}=J^{-1}q$, $\hat{A}=\xi_x A+\xi_y B$ and $\hat{B}=\eta_x A+\eta_y B$.

Introduce a vector $\hat{\mathbf{q}}=(q_{ijk})^{\text{T}}=(q_{001},...,q_{005},q_{101},...,q_{105},...,q_{NM5})^{\text{T}}$ where the three indices i, j and k represent the ξ-coordinate, η-coordinate and the solution variable, respectively. We shall define our discretization in terms of Kronecker

products. This formulation is convenient because it mimics the finite difference implementation. Let $\mathbf{Q}_\xi = Q_\xi \otimes I_\eta \otimes I_5$ and $\mathbf{Q}_\eta = I_\xi \otimes Q_\eta \otimes I_5$ where Q_ξ is the 1D difference operator in the ξ-direction and I_ξ is the unit matrix of size $(N+1)\times(N+1)$. In the other direction, Q_η and I_η are $(M+1)\times(M+1)$ matrices. The computation of the spatial derivatives of $\hat{\mathbf{q}}$ can then be seen as operating on $\hat{\mathbf{q}}$ with one of the Kronecker products, i.e. $\mathbf{Q}_\eta\hat{\mathbf{q}}$ operates on the second index and yields a vector of the same size as $\hat{\mathbf{q}}$ representing the first derivative in the η-direction. To express the semi-discrete linear elastic wave equation, we also need to define $\hat{\mathbf{A}} = I_\xi \otimes I_\eta \otimes \hat{A}$ and $\hat{\mathbf{B}} = I_\xi \otimes I_\eta \otimes \hat{B}$. Note that these products are never actually explicitly formed as they are merely theoretical constructs to make the notation more compact. Using the Kronecker products defined above, the semidiscrete linear elastic wave equation including the SAT term can be written

$$\frac{d\hat{\mathbf{q}}}{dt} = \hat{\mathbf{A}}\mathbf{Q}_\xi\hat{\mathbf{q}} + \hat{\mathbf{B}}\mathbf{Q}_\eta\hat{\mathbf{q}} + \widehat{\mathbf{SAT}}. \tag{10}$$

This system of ordinary differential equations, including the SAT expression is solved using the classical 4th order explicit Runge–Kutta method. No injection is needed to impose boundary conditions, as this is taken care of by the SAT method. A 6th order explicit filter [7] is used to suppress unresolved modes.

The equations (7) and (8) give the expressions in Cartesian coordinates. However, we need the SAT expression for curvilinear coordinates. These can be obtained by considering the system $\hat{q}_t = (k_x A + k_y B)_k$ for the two spatial directions $k = \xi, \eta$. As the expressions become quite long, they are omitted here (cf. [4]).

6 Numerical experiment

We consider now a simple test for our 2D discretization: a square domain occupies the region $-1\,\mathrm{m} \le x \le 1\,\mathrm{m}$, $-1\,\mathrm{m} \le y \le 1\,\mathrm{m}$. At $t = 0\,\mathrm{s}$, we give an initial condition for the stress component $g(x,y,t=0) = g_0(x,y)$, while all other variables are initially zero. The initial condition is defined by $g_0(x,y) = s(2r_1+0.5) - s(2r_2+0.5)$, where $r_1^2 = (x-0.5\,\mathrm{m})^2 + y^2$, $r_2^2 = (x+0.5\,\mathrm{m})^2 + y^2$ and

$$s(r) = \begin{cases} \exp(-1/r - 1/(1-r) + 4)\,\mathrm{kg}/(\mathrm{m}\cdot\mathrm{s}^2), & \text{if } 0\,\mathrm{m} < r < 1\,\mathrm{m} \\ 0, & \text{otherwise.} \end{cases} \tag{11}$$

Thus, $g_0(x,y)$ is a smooth function with infinitely many derivatives and compact support representing two sources located at $(\pm 0.5, 0)$ meters. The material parameters are $\lambda = \mu = 1.0\,\mathrm{kg}/(\mathrm{m}\cdot\mathrm{s}^2)$, $\rho = 1.0\,\mathrm{kg}/\mathrm{m}^3$. We integrate the solution with CFL number 0.8 and impose homogeneous Dirichlet boundary conditions for u and v using the SAT approach (10). We plot the solution evaluated at time $t = 0.5\,\mathrm{s}$ in Figures 1(a) and 1(b). Since the largest wave speed $c_p = \sqrt{(\lambda+2\mu)/\rho} = \sqrt{3}\,\mathrm{m/s}$, at $t = 0.5\,\mathrm{s}$ the P-wave will have reached and been reflected from the left and right

boundaries which are situated a distance 0.5 m from the sources. As the solution is symmetric with respect to the center lines $x = 0$ and $y = 0$, only the first quadrant is shown. The value of the velocity components at the boundary is zero, as enforced by the SAT term.

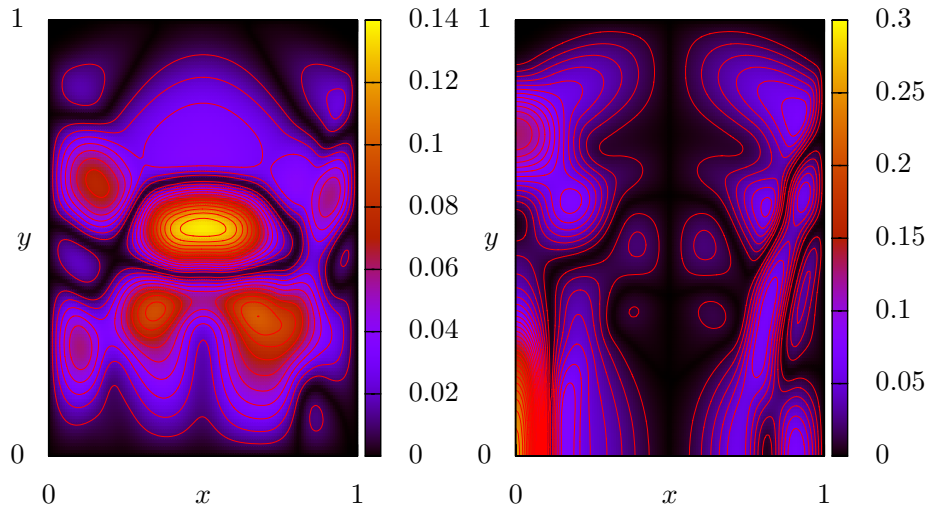

(a) Contour levels of solution variable u (b) Contour levels of solution variable v

Fig. 1 Contour plots showing the absolute value of the velocity components u and v with contour levels spaced 0.01 m/s apart.

$N \times M$	k	$e_2^{(k)}$	$\log_2(e_2^{(k+1)}/e_2^{(k)})$
32×32	6	3.646×10^{-2}	–
64×64	5	6.800×10^{-3}	2.423
128×128	4	8.521×10^{-4}	2.996
256×256	3	7.421×10^{-5}	3.521
512×512	2	4.558×10^{-6}	4.025
1024×1024	1	2.710×10^{-7}	4.072
2048×2048	0	0	–

Table 1 2-norms of error and rates of convergence.

For the same set of parameters and initial/boundary conditions, we compute the solution at different grid resolutions and consider the solution at the finest grid to be exact. We can then calculate the error at each grid level and thus determine the rate of convergence. We define the 2-norm of the error at any grid level k as

$$e_2^{(k)} = \left[\frac{1}{NM} \sum_{\phi \in \{u,v,f,g,h\}} \sum_{i=0}^{N} \sum_{j=0}^{M} \left| \phi_{i,j}^{(k)} - \phi_{\text{exact},i,j}^{(k)} \right|^2 \right]^{1/2}, \tag{12}$$

where $\phi_{\text{exact}}^{(k)}$ is the restriction of the solution $\phi^{(0)}$ on the finest grid to the grid on level k. As can be seen in Table 1, the order in the 2-norm approaches 4 as N and M increase, which is what we expected.

7 Conclusions

We have derived simultaneous approximation terms (SAT) for the 2D linear elastic wave equation in first-order form to yield strictly stable schemes for general Dirichlet boundary conditions. The implementation of the SAT approach for a fourth order difference scheme has proved that the convergence rate is indeed fourth order for a test case with smooth data. The advantage of our approach is that Dirichlet boundary conditions can easily be imposed for either the velocity or the stress components which is required for fluid-structure interaction. In the future, we plan to apply this approach to the nonlinear elastic equations based on a Neo-Hookean model.

Acknowledgements The authors thank Bjørn Skallerud, Paul Leinan and Victorien Prot at the Department of Structural Engineering, NTNU for valuable discussions on the structure model and for Abaqus support. The current research has been funded by the Swedish Research Council under the project "Numerical Simulation of Respiratory Flow".

References

1. M. H. Carpenter, D. Gottlieb, and S. Abarbanel. Time-stable boundary conditions for finite-difference schemes solving hyperbolic systems: Methodology and application to high-order compact schemes. *J. Comp. Phys.*, 111:220 – 236, 1994.
2. B. Gustafsson. *High order difference methods for time-dependent PDE*. Springer-Verlag Berlin Heidelberg, 2008.
3. M. Larsson and B. Müller. Numerical simulation of fluid-structure interaction in human phonation: Application. In *Proceedings of ENUMATH 2009 Eighth European Conference on Numerical Mathematics and Advanced Applications*, Uppsala, Sweden, 2009, to be published by Springer.
4. M. Larsson and B. Müller. Strictly stable high order difference method for the linear elastic wave equation. 2010. Submitted to Commun. Comput. Phys.
5. H. Luo, R. Mittal, X. Zheng, S.A. Bielamowicz, R.J. Walsh, and J.K. Hahn. An immersed-boundary method for flow - structure interaction in biological systems with application to phonation. *Journal of Computational Physics*, 227:9303 – 9332, 2008.
6. K. Mattsson, F. Ham, and G. Iaccarino. Stable boundary treatment for the wave equation on second-order form. *J. Sci. Comput.*, 41:366 – 383, 2009.
7. B. Müller. High order numerical simulation of aeolian tones. *Computers & Fluids*, 37(4):450 – 462, 2008.
8. B. Strand. Summation by parts for finite difference approximations for d/dx. *J. Comput. Physics*, 110:47 – 67, 1994.
9. I.R. Titze. *Principles of voice production*. National Center for Voice and Speech, 2000.

PAPER 5

M. Larsson, B. Müller: Strictly stable high order difference method for the linear elastic wave equation, submitted to *CiCP*, 2010.

Strictly stable high order difference method for the linear elastic wave equation

Martin Larsson[*], Bernhard Müller[†]

March 10, 2010

Department of Energy and Process Engineering, Norwegian University of Science and Technology (NTNU), 7491 Trondheim, Norway

Abstract

A strictly stable high order finite difference method has been developed for the linear elastic wave equation as a first order hyperbolic system. With summation by parts (SBP) operators and simultaneous approximation terms (SAT), a time stable solution can be guaranteed. We derive the SAT expressions for the 2D linear elastic wave equation in Cartesian and curvilinear coordinates and verify high convergence rate for smooth solutions (and low dispersion errors for a discontinuous solution).

1 Introduction

The numerical solution of wave equations finds applications in many fields including seismology, acoustics and general relativity. The main motivation for solving the linear elastic wave equations has been to model seismological waves in the Earth and wave propagation in inhomogeneous or discontinuous media. The linear elastic wave equation is often solved in a second order formulation because this formulation reduces the number of variables which need to be integrated [12, 5, 14].

When written as a system of first order equations, the well developed stability theory for hyperbolic systems applies directly. The disadvantage of the first order formulation of the wave equation is the increased computational effort required for the additional variables. Our main motivation for using a first order formulation is, however, related to the actual physical system that we want to simulate. In fluid-structure interaction, the traction boundary condition dictates the stresses on the elastic body. In the first order formulation, the traction boundary condition can be easily formulated as a simple Dirichlet condition for a subset of the solution variables. Dirichlet boundary conditions are not at all straightforward to impose in a second order formulation [12].

For simulations of wave propagation over large times, high order methods are superior to their low order counterparts in terms of accuracy per amount of computational power invested, especially in two and three space dimensions. Schemes that converge to the true solution as the grid size goes to zero and are stable in the classical sense may, however, still exhibit a non-physical growth of the solution as time increases. It is therefore important to make sure that schemes are time stable, also known as strictly stable (cf. e.g. [15]). This can be achieved by using of summation by parts operators [17, 10] together with simultaneous approximation terms (SAT) [2] for imposing boundary conditions. This gives an energy estimate for the discrete equations similar to the one for the continuous equations, which guarantees a non-growing energy and therefore strict stability for the discretized homogeneous wave equation. It is straightforward to derive SAT expressions for the Dirichlet boundary conditions in the first order formulation.

Faccioli et al. [6] used a spectral method with domain decomposition to model 3D elastic waves in the Earth employing non-reflecting boundary conditions to effectively approximate an infinite domain and the leap-frog method

[*]Corresponding author. martin.larsson@ntnu.no
[†]bernhard.muller@ntnu.no

for time integration. Discrete Galerkin methods have been used by Käser and Dumbser in [11] to solve the elastic wave equation in heterogeneous media on unstructured triangular grids. Fornberg and Ghrist [8] investigated different types of finite difference approximations for wave equations, leading to the conclusion that high order accurate compact schemes and staggered grids are computationally effective techniques for approximating the first derivatives in space for wave equations. The related study [9] investigated the stability and accuracy of different time integrators for finite difference discretizations of linear wave equations on staggered grids. It was found that staggered schemes have a smaller truncation error than their non-staggered counterparts. Casadei et al. [4] presented a hybrid spectral/finite element method for solving elastic wave propagation problems using a mortar method to handle the interface between spectral and finite elements. The method handles heterogeneous media and complex geometries. Appelö and Petersson [1] presented a stable second order accurate method for the elastic wave equation in second order formulation and curvilinear coordinates using summation by parts operators.

In this paper, we present a strictly stable high-order method for the linear elastic wave equation in curvilinear coordinates written as a hyperbolic system. We present all the ingredients necessary to implement SAT expressions both for velocity components and stress components.

Outline of presentation

The objective is to obtain simultaneous approximation term (SAT) expressions (cf. section 3.3) for the 2D linear elastic wave equation in transformed (curvilinear) coordinates. We accomplish this by diagonalizing the hyperbolic system in one spatial direction at the time in order to obtain the SAT expression for that direction in primitive variables. The corresponding 1D SAT expression in real (flow) variables is then the transformation matrix times the SAT expression in primitive variables, and finally the full 2D SAT expression is the sum of the contributions from the two coordinate directions. To keep the discussion simple, the main body of the text concerns SAT in Cartesian coordinates while the generalization to curvilinear grids is placed in the appendix.

In section 2, we introduce the governing equations, i.e. the linear elastic wave equations in first order form written as a hyperbolic system and describe how to decouple the system using characteristic variables in each space dimension. We then proceed in section 3 to give the details of the summation by parts (SBP) operators and simultaneous approximation terms applied to the decoupled hyperbolic systems. Numerical results for three different test cases are presented in section 4 and the conclusions are stated in section 5.

2 Linear elastic wave equation

The 2D linear elastic wave equation in first order form reads in Cartesian coordinates

$$\begin{aligned} u_t &= (1/\rho) f_x + (1/\rho) g_y \\ v_t &= (1/\rho) g_x + (1/\rho) h_y \\ f_t &= (\lambda + 2\mu) u_x + \lambda v_y \\ g_t &= \mu v_x + \mu u_y \\ h_t &= \lambda u_x + (\lambda + 2\mu) v_y \end{aligned} \tag{1}$$

where u, v are the velocity components and f, g, h are the three independent components of the symmetric Cauchy stress tensor σ. The Lamé parameters λ, μ and the density ρ are here taken to be constant in space and time.

Introducing the solution vector q and coefficient matrices A and B allows us to write the linear elastic wave equation (1) as a first order hyperbolic system

$$q_t = A q_x + B q_y, \tag{2}$$

where $q = (u, v, f, g, h)^{\mathrm{T}}$ and

$$A = \begin{bmatrix} 0 & 0 & 1/\rho & 0 & 0 \\ 0 & 0 & 0 & 1/\rho & 0 \\ \lambda + 2\mu & 0 & 0 & 0 & 0 \\ 0 & \mu & 0 & 0 & 0 \\ \lambda & 0 & 0 & 0 & 0 \end{bmatrix}, \quad B = \begin{bmatrix} 0 & 0 & 0 & 1/\rho & 0 \\ 0 & 0 & 0 & 0 & 1/\rho \\ 0 & \lambda & 0 & 0 & 0 \\ \mu & 0 & 0 & 0 & 0 \\ 0 & \lambda + 2\mu & 0 & 0 & 0 \end{bmatrix}.$$

The linear combination $P(k_x,k_y) = k_xA + k_yB$ where $k = (k_x,k_y) \in \mathbb{R}^2$ can be diagonalized with real eigenvalues and linearly independent eigenvectors. The eigenvalue matrix is defined as the diagonal matrix with the eigenvalues of $P(k_x,k_y)$ in decreasing order,

$$\tilde{\Lambda}(k_x,k_y) = (k_x^2+k_y^2)^{1/2}\mathrm{diag}(c_p,c_s,0,-c_s,-c_p) = \mathrm{diag}\left\{\tilde{\lambda}_i(k_x,k_y)\right\}_{i=1}^{5}, \tag{3}$$

where the wave speeds are $c_s = \sqrt{\mu/\rho}$ and $c_p = \sqrt{(\lambda+2\mu)/\rho}$, referred to as secondary (or shear) and primary wave velocity, respectively. For convenience, we also define the parameter $\alpha = (\lambda+2\mu)/\lambda = c_p^2/(c_p^2-2c_s^2)$. We will need to transform the system to characteristic variables in order to derive the SAT expression.

Since the system (2) is hyperbolic, there exists an nonsingular matrix $T(k_x,k_y)$ for all directions k such that $T^{-1}(k_x,k_y)P(k_x,k_y)T(k_x,k_y) = \Lambda(k_x,k_y)$. For the x-direction, $k_x = 1, k_y = 0$ gives the transformation matrix $T_x = T(1,0)$ and its inverse

$$T_x = \begin{bmatrix} c_p/\lambda & 0 & 0 & 0 & -c_p/\lambda \\ 0 & 1 & 0 & 1 & 0 \\ \alpha & 0 & 0 & 0 & \alpha \\ 0 & c_s\rho & 0 & -c_s\rho & 0 \\ 1 & 0 & 1 & 0 & 1 \end{bmatrix}, \quad T_x^{-1} = \frac{1}{2}\begin{bmatrix} \lambda/c_p & 0 & 1/\alpha & 0 & 0 \\ 0 & 1 & 0 & 1/(\rho c_s) & 0 \\ 0 & 0 & -2/\alpha & 0 & 2 \\ 0 & 1 & 0 & -1/(\rho c_s) & 0 \\ -\lambda/c_p & 0 & 1/\alpha & 0 & 0 \end{bmatrix}.$$

The characteristic variables $u^{(x)}$ in the x-direction are then

$$u^{(x)} = T_x^{-1}q = \frac{1}{2}\begin{bmatrix} \lambda u/c_p + f/\alpha \\ v + g/(\rho c_s) \\ -2f/\alpha + 2h \\ v - g/(\rho c_s) \\ -\lambda u/c_p + f/\alpha \end{bmatrix}. \tag{4}$$

Note that we use the symbol u to refer to both the vector of characteristic variables and the first velocity component. The meaning of u should be clear from the context. The decoupled characteristic equations in 1D are obtained by premultiplying (2) by T_x^{-1} and setting the y-derivative to zero,

$$u_t^{(x)} = \Lambda u_x^{(x)} \tag{5}$$

where $\Lambda = \mathrm{diag}(c_p,c_s,0,-c_s,-c_p)$. The transformation back to the flow variables is given by $q = T_x u^{(x)}$.

Likewise for the y-direction, the transformation matrix, its inverse, the characteristic variables and the transformation back are

$$T_y = \begin{bmatrix} 0 & 1 & 0 & 1 & 0 \\ c_p/\lambda & 0 & 0 & 0 & -c_p/\lambda \\ 1 & 0 & 1 & 0 & 1 \\ 0 & \rho c_s & 0 & -\rho c_s & 0 \\ \alpha & 0 & 0 & 0 & \alpha \end{bmatrix}, \quad T_y^{-1} = \frac{1}{2}\begin{bmatrix} 0 & \lambda/c_p & 0 & 0 & 1/\alpha \\ 1 & 0 & 0 & 1/(\rho c_s) & 0 \\ 0 & 0 & 2 & 0 & -2/\alpha \\ 1 & 0 & 0 & -1/(\rho c_s) & 0 \\ 0 & -\lambda/c_p & 0 & 0 & 1/\alpha \end{bmatrix}, \tag{6}$$

$$u^{(y)} = \frac{1}{2}\begin{bmatrix} \lambda v/c_p + h/\alpha \\ u + g/(\rho c_s) \\ 2f - 2h/\alpha \\ u - g/(\rho c_s) \\ -\lambda v/c_p + h/\alpha \end{bmatrix}, \quad q = T_y u^{(y)}. \tag{7}$$

2.1 Coordinate transformation

To treat curvilinear grids we introduce the mapping $x = x(\xi,\eta), y = y(\xi,\eta)$ and introduce an equidistant computational grid with coordinates $\xi_i, i = 0,...,N$, $\eta_j, j = 0,...,M$. The Jacobian determinant J of the transformation is given by $J^{-1} = x_\xi y_\eta - x_\eta y_\xi$. The linear elastic wave equation can then be written as

$$\hat{q}_t = (\hat{A}\hat{q})_\xi + (\hat{B}\hat{q})_\eta \tag{8}$$

where the hats signify that the quantities are in transformed coordinates, i.e. $\hat{q} = J^{-1}q$, $\hat{A} = \xi_x A + \xi_y B$ and $\hat{B} = \eta_x A + \eta_y B$.

3 Strictly stable high order difference method

3.1 Energy method

The energy method is a general technique to prove sufficient conditions for well-posedness of partial differential equations (PDE) and stability of difference methods with general boundary conditions.

Consider the solution of the model problem in 1D with

$$u_t = \lambda u_x,\ \lambda > 0,\ 0 \le x \le 1,\ t \ge 0,\ u(x,0) = f(x),\ u(1,t) = g(t). \tag{9}$$

The symbol λ represents here a general eigenvalue for the hyperbolic system and should not be confused with the Lamé parameter. Define the L_2 scalar product for real functions v and w on the interval $0 \le x \le 1$ as

$$(v,w) = \int_0^1 v(x)w(x)dx \tag{10}$$

which defines a norm of the continuous solution at some time t and an energy $E(t) = ||u(\cdot,t)||^2 = (u,u)$. Using integration by parts $(v,w_x) = v(1,t)w(1,t) - v(0,t)w(0,t) - (v_x,w)$, we get $\frac{dE}{dt} = \frac{d||u||^2}{dt} = (u_t,u) + (u,u_t) = \lambda[(u_x,u) + (u,u_x)] = \lambda[(u_x,u) + [u^2]_0^1 - (u_x,u)] = \lambda[u^2(1,t) - u^2(0,t)]$. If $\lambda > 0$, the boundary condition $u(1,t) = 0$ yields a non-growing solution (note that periodic boundary conditions would also yield a non-growing solution), i.e. $E(t) \le E(0) = ||f(x)||^2$. Thus, the energy of the solution is bounded by the energy of the initial data. Hence the problem is well-posed.

3.2 Summation by parts operators

The idea behind the summation by parts technique (cf. e.g. [10]) is to use an operator Q which satisfies the corresponding discrete property as the integration by parts of the continuous function, called the summation by parts (SBP) property. For the numerical solution of (9), we introduce the equidistant grid $x_j = jh,\ j = 0,...,N,\ h = 1/N$, and a solution vector containing the solution at the discrete grid points, $\mathbf{u} = (u_0(t), u_1(t), ..., u_N(t))^{\mathrm{T}}$. The semi-discrete problem can be stated using a difference operator Q approximating the first derivative,

$$\frac{d\mathbf{u}}{dt} = \lambda Q\mathbf{u},\ u_i(0) = f(x_i). \tag{11}$$

We also define a discrete scalar product and corresponding norm and energy by

$$(\mathbf{u},\mathbf{v})_h = h\sum_{i,j} h_{ij}u_i v_j = h\mathbf{u}^{\mathrm{T}}H\mathbf{v}, \quad E_h(t) = ||\mathbf{u}||_h^2 = (\mathbf{u},\mathbf{u})_h, \tag{12}$$

where the symmetric and positive definite norm matrix $H = \mathrm{diag}(H_L, I, H_R)$ has components h_{ij}. In order for (12) to define a scalar product, H_L and H_R must be symmetric and positive definite. We say that the scalar product satisfies the summation by parts property (SBP), if

$$(\mathbf{u},Q\mathbf{v})_h = u_N v_N - u_0 v_0 - (Q\mathbf{u},\mathbf{v})_h. \tag{13}$$

It can be seen that this property is satisfied if the matrix $G = HQ$ satisfies the condition that $G + G^{\mathrm{T}} = \mathrm{diag}(-1,0,...,0,1)$. If Q and its corresponding norm matrix H satisfy the SBP property (13), then the energy method for the discrete problem yields:

$$\frac{dE_h}{dt} = \frac{d||u||_h^2}{dt} = (u_t,u)_h + (u,u_t)_h = \lambda[(Qu,u)_h + (u,Qu)_h] = \lambda[(Qu,u)_h + u_N^2 - u_0^2 - (Qu,u)_h] = \lambda[u_N^2 - u_0^2]. \tag{14}$$

How to obtain $dE_h/dt \leq 0$ is the topic of the next section.

For diagonal H_L and H_R there exist difference operators Q accurate to order $\mathscr{O}(h^{2s})$ in the interior and $\mathscr{O}(h^s)$ near the boundaries for $s = 1,2,3$ and 4. These operators have an effective order of accuracy $\mathscr{O}(h^{s+1})$ in the entire domain. Explicit forms of such operators Q and norm matrices H were derived by Strand [17].

For this study, we use an SBP operator based on the central sixth order explicit finite difference operator ($s = 3$) which has been modified near the boundaries in order to satisfy the SBP property giving an effective $\mathscr{O}(h^4)$ order of accuracy in the whole domain.

3.3 Simultaneous approximation term

Since one of the terms in (14) is non-negative, strict stability does not follow when using the injection method for the summation by parts operator, i.e. by using $u_N(t) = g(t)$. In contrast, the simultaneous approximation term (SAT) method is an approach where a linear combination of the boundary condition and the differential equation is solved at the boundary. This leads to a weak imposition of the physical boundary conditions. The imposition of SAT boundary conditions is accomplished by adding a source term to the derivative operator, proportional to the difference between the value of the discrete solution u_N and the boundary condition to be fulfilled. The SAT method for the semidiscrete advection equation (11) can be expressed as

$$\frac{d\mathbf{u}}{dt} = \lambda Q\mathbf{u} - \lambda\,\tau\mathbf{S}(u_N - g(t))$$

where $\mathbf{S} = h^{-1}H^{-1}(0,0,...,0,1)^{\mathrm{T}}$ and τ is a free parameter.

The added term does not alter the accuracy of the scheme since it vanishes when the analytical solution is substituted. Thus, we can imagine the SAT expression as a modification to the difference operator so that we are effectively solving an equation $\mathbf{u}_t = \lambda\tilde{Q}\mathbf{u}$ with $\tilde{Q} = Q + Q^{\mathrm{sat}}$ without imposing the boundary conditions directly. When H is diagonal, the scheme is only modified at one point on the boundary. We can now show that this scheme is strictly stable for $g(t) = 0$. The energy rate for the solution of the semi-discrete equation is $\frac{dE_h}{dt} = \frac{d||u||_h^2}{dt} = (\mathbf{u}_t,\mathbf{u})_h + (\mathbf{u},\mathbf{u}_t)_h$ $= \lambda[(\mathbf{u},Q\mathbf{u} - \tau\mathbf{S}u_N)_h + (Q\mathbf{u} - \tau\mathbf{S}u_N,\mathbf{u})_h] = \lambda[(\mathbf{u},Q\mathbf{u})_h - \tau(\mathbf{u},\mathbf{S})_h u_N + (Q\mathbf{u},\mathbf{u})_h - \tau(\mathbf{S},\mathbf{u})_h u_N] = \lambda[(1-2\tau)u_N^2 - u_0^2]$ since $(\mathbf{S},\mathbf{u})_h = (\mathbf{u},\mathbf{S})_h = h\mathbf{u}^{\mathrm{T}}Hh^{-1}H^{-1}(0,0,...,0,1)^{\mathrm{T}} = u_N$. The discretization is time stable if $\tau \geq 1/2$.

We now present analogously but without proof (cf. [2]) the strictly stable SAT method for a hyperbolic system in one space dimension with diagonal coefficient matrices with the aim to obtain SAT expressions for the diagonalized linear elastic wave equation (5). In general, the continuous system is $u_t = \Lambda u_x$ with r unknowns and r equations ($r = 5$ here). The coefficient matrix Λ is chosen such that the eigenvalues are in descending order, i.e. $\lambda_1 > \lambda_2 > ... > \lambda_k > 0 > \lambda_{k+1} > ... > \lambda_r$. We split the solution vector into two parts corresponding to positive and negative eigenvalues $\mathbf{u}^{\mathrm{I}} = (\mathbf{u}^{(1)},...,\mathbf{u}^{(k)})^{\mathrm{T}}$ and $\mathbf{u}^{\mathrm{II}} = (\mathbf{u}^{(k+1)},...,\mathbf{u}^{(r)})^{\mathrm{T}}$, where the components $\mathbf{u}^{(i)}$ are grid functions of length $N+1$. For the components in $\mathbf{u}^{\mathrm{I}}$ we have boundary conditions at $x = 1$, and for $\mathbf{u}^{\mathrm{II}}$ we need to specify boundary conditions at $x = 0$, as this is required for well-posedness.

Since we are here dealing with characteristic variables, we need to transform our physical boundary conditions to boundary conditions for the characteristic variables. This is done by the boundary functions $\mathbf{g}^{\mathrm{I}}(t) = (g^{(1)}(t),...,g^{(k)}(t))$, $\mathbf{g}^{\mathrm{II}}(t) = (g^{(k+1)}(t),...,g^{(r)}(t))$ and the coupling matrices R and L defined by

$$\mathbf{u}^{\mathrm{I}}(1,t) = R\mathbf{u}^{\mathrm{II}}(1,t) + \mathbf{g}^{\mathrm{I}}(t), \quad \mathbf{u}^{\mathrm{II}}(0,t) = L\mathbf{u}^{\mathrm{I}}(0,t) + \mathbf{g}^{\mathrm{II}}(t). \tag{15}$$

The SAT method is then:

$$\begin{array}{rll} \frac{d\mathbf{u}^{(i)}}{dt} = & \lambda_i Q\mathbf{u}^{(i)} - \lambda_i\tau\mathbf{S}^{(i)}(\mathbf{u}_N^{(i)} - (R\mathbf{u}^{\mathrm{II}})_N^{(i)} - g^{(i)}(t)), & 1 \leq i \leq k \\ \frac{d\mathbf{u}^{(i)}}{dt} = & \lambda_i Q\mathbf{u}^{(i)} + \lambda_i\tau\mathbf{S}^{(i)}(\mathbf{u}_0^{(i)} - (L\mathbf{u}^{\mathrm{I}})_0^{(i-k)} - g^{(i)}(t)), & k+1 \leq i \leq r \end{array} \tag{16}$$

where $\mathbf{S}^{(i)} = h^{-1}H^{-1}(0,0,...,1)^{\mathrm{T}}$ for $1 \leq i \leq k$ and $\mathbf{S}^{(i)} = h^{-1}H^{-1}(1,0,...,0)^{\mathrm{T}}$ for $k+1 \leq i \leq r$. Regarding the notation, $(R\mathbf{u}^{\mathrm{II}})_N^{(i)}$ should be interpreted as follows: $\mathbf{u}^{\mathrm{II}}$ is an $(r-k)\times 1$ vector where each component is a grid function of length $N+1$. Multiplying R (being a $k\times(r-k)$ matrix) with $\mathbf{u}^{\mathrm{II}}$ yields a new vector of grid functions ($k\times 1$ vector). Take

the (i)th grid function in this vector and finally the Nth component in the resulting grid function. As shown in [2], the SAT method is both stable and time stable provided that

$$\frac{1-\sqrt{1-|R||L|}}{|R||L|} \leq \tau \leq \frac{1+\sqrt{1-|R||L|}}{|R||L|} \tag{17}$$

with the additional constraint that $|R||L| \leq 1$, where the matrix norm is defined as $|R| = \rho(R^T R)^{1/2}$ and ρ is the spectral radius.

3.4 SAT expressions for elastic wave equation

Here we shall show how the SAT expression is derived for the 2D linear elastic wave equation in Cartesian coordinates, but first we need to make a short digression on notation.

Notation

The Kronecker product of an $n \times m$ matrix C and a $k \times l$ matrix D is the $n \times m$ block matrix

$$C \otimes D = \begin{bmatrix} c_{11}D & \cdots & c_{1m}D \\ \vdots & \ddots & \vdots \\ c_{n1}D & \cdots & c_{nm}D \end{bmatrix}. \tag{18}$$

This notation will become useful later for writing the discretization in a compact form.

We adopt the notation $u(k_0,t) = \bar{u}(k = k_0,t)$ to represent a 1D boundary condition on the solution variable u in any direction k where $k = x$ or $k = y$ and $\bar{u}(k,t)$ is the given functions of time on the boundaries $k = 0$ and $k = 1$ which the solution variable u should match on those boundaries. For example, $\bar{u}(x = 1,t)$ is the given u-velocity on the boundary $x = 1$ and $u(1,t)$ is the corresponding solution to the equations. In 2D, the boundary condition also dependends on the second coordinate direction, which we indicate by $\bar{u}(x = 1,y,t)$ and $\bar{u}(x,y = 1,t)$ for boundary conditions in the x- and y-direction, respectively. Finally, for the discretized 2D boundary conditions, we write instead $\bar{u}_j(x = 1,t) = \bar{u}(x = 1,y_j,t)$ and $\bar{u}_i(y = 1,t) = \bar{u}(x_i,y = 1,t)$.

3.4.1 Derivation of SAT expressions

The vector of characteristic variables in the x-direction is given in Eq. (4), but henceforth we drop the superscript $^{(x)}$. The derivation for the y-direction is analogous.

We split (4) into two vectors corresponding to the positive and negative eigenvalues, omitting the characteristic variable corresponding to the zero eigenvalue (the omission is justified since the resulting SAT expression is proportional to the zero eigenvalue)

$$u^{\mathrm{I}} = \frac{1}{2}\begin{bmatrix} (\lambda/c_p)u + (1/\alpha)f \\ v + (1/c_s\rho)g \end{bmatrix}, \quad u^{\mathrm{II}} = \frac{1}{2}\begin{bmatrix} v - (1/c_s\rho)g \\ (-\lambda/c_p)u + (1/\alpha)f \end{bmatrix}$$

and define the coefficient matrices $\Lambda^{\mathrm{I}} = \mathrm{diag}(c_p, c_s)$, $\Lambda^{\mathrm{II}} = \mathrm{diag}(-c_s, -c_p)$. The boundary functions g^{I}, g^{II}, and the matrices L and R are defined by the relations (15). For example, the identify $u^{\mathrm{I}} = \begin{bmatrix} 0 & 1 \\ -1 & 0 \end{bmatrix} u^{\mathrm{II}} + \begin{bmatrix} \lambda u/c_p \\ v \end{bmatrix}$ defines $R = \begin{bmatrix} 0 & 1 \\ -1 & 0 \end{bmatrix}$ and $\mathbf{g}^{\mathrm{I}}(t) = g^{\mathrm{I}}(t) \otimes E_N$ where $g^{\mathrm{I}}(t) = \begin{bmatrix} \lambda\bar{u}(x = 1,t)/c_p \\ \bar{v}(x = 1,t) \end{bmatrix}$ for the boundary conditions $u(1,t) = \bar{u}(x = 1,t)$, $v(1,t) = \bar{v}(x = 1,t)$ and the matrix E_N is

$$E_N = \begin{bmatrix} 0 & \cdots & 0 & 0 \\ \vdots & \ddots & \vdots & \vdots \\ 0 & \cdots & 0 & 0 \\ 0 & \cdots & 0 & 1 \end{bmatrix}. \tag{19}$$

Boundary condition	R	$g^{\mathrm{I}}(t)$
$u(1,t)=\bar{u}(x=1,t)$,$v(1,t)=\bar{v}(x=1,t)$	$\begin{bmatrix} 0 & 1 \\ -1 & 0 \end{bmatrix}$	$\begin{bmatrix} \lambda\bar{u}(x=1,t)/c_p \\ \bar{v}(x=1,t) \end{bmatrix}$
$f(1,t)=\bar{f}(x=1,t)$, $g(1,t)=\bar{g}(x=1,t)$	$\begin{bmatrix} 0 & -1 \\ 1 & 0 \end{bmatrix}$	$\begin{bmatrix} (1/\alpha)\bar{f}(x=1,t) \\ \bar{g}(x=1,t)/(\rho c_s) \end{bmatrix}$

Table 1: Boundary conditions at $x=1$ (right)

Boundary condition	L	$g^{\mathrm{II}}(t)$
$u(0,t)=\bar{u}(x=0,t)$, $v(0,t)=\bar{v}(x=0,t)$	$\begin{bmatrix} 0 & -1 \\ 1 & 0 \end{bmatrix}$	$\begin{bmatrix} \bar{v}(x=0,t) \\ -\lambda\bar{u}(x=0,t)/c_p \end{bmatrix}$
$f(0,t)=\bar{f}(x=0,t)$, $g(0,t)=\bar{g}(x=0,t)$	$\begin{bmatrix} 0 & 1 \\ -1 & 0 \end{bmatrix}$	$\begin{bmatrix} -\bar{g}(x=0,t)/(\rho c_s) \\ (1/\alpha)\bar{f}(x=0,t) \end{bmatrix}$

Table 2: Boundary conditions at $x=0$ (left)

The expressions for some important combinations of boundary conditions are given in Tables 1 and 2. Other combinations of boundary conditions are possible, e.g. u and g given, but these are physically not interesting and are therefore not included here. We do not consider non-reflecting boundary conditions here. The corresponding boundary conditions for the characteristic variables in the y-direction are stated in tables 3 and 4.

The discrete 1D SAT expression (16) is formed using the first rows of Tables 1, 2, 3 and 4 for boundary conditions on the velocity components. We let the grid functions $\mathbf{u}$ and $\mathbf{v}$ in 2D with points labeled $i \in \{0,...,N\}$ and $j \in \{0,...,M\}$ in the x- and y-directions, respectively, correspond to the solution variables u and v in the discretization of the linear elastic wave equation. The SAT expressions, one for each spatial direction and for each solution variable are also grid functions of the same size as $\mathbf{u}$ and $\mathbf{v}$ but only nonzero on the boundaries. The SAT expressions in characteristic variables are given in Table 5. Note that δ_{ij} in Table 5 denotes the Kronecker delta, i.e. the SAT expressions are nonzero only on the boundaries.

Remark

We note that, as the spectral radius of both L and R is 1 (cf. Tables 1, 2, 3 and 4), for all types of boundary conditions considered here, the inequalities (17) lend no other choice than $\tau = 1$ to guarantee time-stability.

3.5 Discretization

Introduce a vector $\hat{\mathbf{q}} = (q_{ijk})^{\mathrm{T}} = (q_{001},...,q_{005},q_{101},...,q_{105},...,q_{NM5})^{\mathrm{T}}$ where the three indices i, j and k represent the ξ-coordinate, η-coordinate and the solution variable, respectively. We define difference operators in terms of Kronecker products that operate on one index at a time.

Let $\mathbf{Q}_\xi = Q_\xi \otimes I_M \otimes I_5$ and $\mathbf{Q}_\eta = I_N \otimes Q_\eta \otimes I_5$ where Q_ξ and Q_η are 1D difference operators in the ξ- and η-directions satisfying the SBP property (13). The identity operators I_N and I_M are unit matrices of size $(N+1)\times(N+1)$ and $(M+1)\times(M+1)$, respectively. The computation of the spatial derivatives of $\hat{\mathbf{q}}$ can then be seen as operating on $\hat{\mathbf{q}}$ with one of the Kronecker products, i.e. $\mathbf{Q}_\eta\hat{\mathbf{q}}$ operates on the second index and yields a vector of the same size as $\hat{\mathbf{q}}$

Boundary condition	R	$g^{\mathrm{I}}(t)$
$u(1,t)=\bar{u}(y=1,t)$,$v(1,t)=\bar{v}(y=1,t)$	$\begin{bmatrix} 0 & 1 \\ -1 & 0 \end{bmatrix}$	$\begin{bmatrix} \lambda\bar{v}(y=1,t)/c_p \\ \bar{u}(y=1,t) \end{bmatrix}$
$g(1,t)=\bar{g}(y=1,t)$, $h(1,t)=\bar{g}(y=1,t)$	$\begin{bmatrix} 0 & -1 \\ 1 & 0 \end{bmatrix}$	$\begin{bmatrix} \bar{g}(y=1,t)/\alpha \\ \bar{g}(y=1,t)/(\rho c_s) \end{bmatrix}$

Table 3: Boundary conditions at $y=1$ (top)

Boundary condition	L	$g^{\mathrm{II}}(t)$
$u(0,t)=\bar{u}(y=0,t), v(0,t)=v(y=0,t)$	$\begin{bmatrix} 0 & -1 \\ 1 & 0 \end{bmatrix}$	$\begin{bmatrix} \bar{u}(y=0,t) \\ -\lambda v(y=0,t)/c_p \end{bmatrix}$
$g(0,t)=\bar{g}(y=0,t)$, $h(0,t)=\bar{g}(y=0,t)$	$\begin{bmatrix} 0 & 1 \\ -1 & 0 \end{bmatrix}$	$\begin{bmatrix} -\bar{g}(y=0,t)/(\rho c_s) \\ \bar{g}(y=0,t)/\alpha \end{bmatrix}$

Table 4: Boundary conditions at $y=0$ (bottom)

SAT	BC on u,v	BC on f,g or g,h
$\mathrm{SAT}^x_{i,j,1} =$	$-\lambda\tau(h_x h_{NN})^{-1}\delta_{iN}\left(u_{N,j}-\bar{u}_j(x=1,t)\right)$	$(-c_p/\alpha)\tau(h_x h_{NN})^{-1}\delta_{iN}\left(f_{N,j}-\bar{f}_j(x=1,t)\right)$
$\mathrm{SAT}^x_{i,j,2} =$	$-c_s\tau(h_x h_{NN})^{-1}\delta_{iN}\left(v_{N,j}-\bar{v}_j(x=1,t)\right)$	$(-1/\rho)\tau(h_x h_{NN})^{-1}\delta_{iN}\left(g_{N,j}-\bar{g}_j(x=1,t)\right)$
$\mathrm{SAT}^x_{i,j,3} =$	0	0
$\mathrm{SAT}^x_{i,j,4} =$	$-c_s\tau(h_x h_{00})^{-1}\delta_{i0}\left(v_{0,j}-\bar{v}_j(x=0,t)\right)$	$(1/\rho)\tau(h_x h_{00})^{-1}\delta_{i0}\left(g_{0,j}-\bar{g}_j(x=0,t)\right)$
$\mathrm{SAT}^x_{i,j,5} =$	$\lambda\tau(h_x h_{00})^{-1}\delta_{i0}\left(u_{0,j}-\bar{u}_j(x=0,t)\right)$	$(-c_p/\alpha)\tau(h_x h_{00})^{-1}\delta_{i0}\left(f_{0,j}-\bar{f}_j(x=0,t)\right)$
$\mathrm{SAT}^y_{i,j,1} =$	$-\lambda\tau(h_y h_{MM})^{-1}\delta_{jM}\left(v_{i,M}-\bar{v}_i(y=1,t)\right)$	$(-c_s/\alpha)\tau(h_y h_{MM})^{-1}\delta_{jM}\left(h_{i,M}-\bar{h}_i(y=1,t)\right)$
$\mathrm{SAT}^y_{i,j,2} =$	$-c_s\tau(h_y h_{MM})^{-1}\delta_{jM}\left(u_{i,M}-\bar{u}_i(y=1,t)\right)$	$(-1/\rho)\tau(h_y h_{MM})^{-1}\delta_{jM}\left(g_{i,M}-\bar{g}_i(y=1,t)\right)$
$\mathrm{SAT}^y_{i,j,3} =$	0	0
$\mathrm{SAT}^y_{i,j,4} =$	$-c_s\tau(h_y h_{00})^{-1}\delta_{j0}\left(u_{i,0}-\bar{u}_i(y=0,t)\right)$	$(1/\rho)\tau(h_y h_{00})^{-1}\delta_{j0}\left(g_{i,0}-\bar{g}_i(y=0,t)\right)$
$\mathrm{SAT}^y_{i,j,5} =$	$\lambda\tau(h_y h_{00})^{-1}\delta_{j0}\left(v_{i,0}-\bar{v}_i(y=0,t)\right)$	$(-c_p/\alpha)\tau(h_y h_{00})^{-1}\delta_{j0}\left(h_{i,0}-\bar{h}_i(y=0,t)\right)$

Table 5: Explicit forms of SAT expressions in characteristic variables in the x-direction (first five rows) and in the y-direction (last five rows). The Kronecker delta δ_{ij} is defined by $\delta_{ij}=1$ if $i=j$ and $\delta_{ij}=0$ if $i\neq j$. The parameter τ is defined by Eq. (17). Here: $\tau=1$. The constant grid spacings in the x- and y-directions are h_x and h_y, respectively. The components of the norm matrix H are denoted by h_{ij}. The SAT expressions corresponding to eigenvalue 0 disappear in each case because the SAT expressions are all proportional to the eigenvalue.

representing the first derivative in the η-direction. To express the semi-discrete linear elastic wave equation, we also need to define $\hat{\mathbf{A}}=I_N\otimes I_M\otimes\hat{A}$ and $\hat{\mathbf{B}}=I_N\otimes I_M\otimes\hat{B}$. Note that these products are never actually explicitly formed as they are merely theoretical constructs to make the notation more compact. The products correspond well to the actual finite difference implementation, i.e. the first derivatives are calculated by operating on successive lines of values in the computational domain. Using the Kronecker products defined above, the semi-discrete linear elastic wave equation with constant coefficients including the SAT expression can be written as

$$\frac{d\hat{\mathbf{q}}}{dt}=\mathbf{Q}_\xi(\hat{\mathbf{A}}\hat{\mathbf{q}})+\mathbf{Q}_\eta(\hat{\mathbf{B}}\hat{\mathbf{q}})+\widehat{\overline{\mathbf{SAT}}} \tag{20}$$

where $\widehat{\overline{\mathbf{SAT}}}$ is the SAT expression in transformed coordinates. To illustrate the procedure, we give the SAT expression in Cartesian coordinates in section 3.5.1 and give the generalization to curvilinear coordinates in the appendix.

3.5.1 SAT expressions in Cartesian coordinates

In table 5 are listed the SAT expressions in characteristic variables in the x-direction and y-directions for all combinations of boundary conditions that make sense physically. These SAT expressions can be transformed to flow variables, indicated in the equations with an over-line, by operating with the transformation matrix, given in section 2, on the last index, i.e. $\overline{\mathbf{SAT}}^x=(I_N\otimes I_M\otimes T^x)\mathbf{SAT}^x$ and $\overline{\mathbf{SAT}}^y=(I_N\otimes I_M\otimes T^y)\mathbf{SAT}^y$, which yields for boundary conditions on u,v in the x-direction

$$\begin{aligned}
\overline{\mathrm{SAT}}^x_{i,j,1} &= -c_p\tau h_x^{-1}\left[h_{NN}^{-1}\delta_{iN}\left(u_{N,j}-\bar{u}_j(x=1,t)\right)+h_{00}^{-1}\delta_{i0}\left(u_{0,j}-\bar{u}_j(x=0,t)\right)\right]\\
\overline{\mathrm{SAT}}^x_{i,j,2} &= -c_s\tau h_x^{-1}\left[h_{NN}^{-1}\delta_{iN}\left(v_{N,j}-\bar{v}_j(x=1,t)\right)+h_{00}^{-1}\delta_{i0}\left(v_{0,j}-\bar{v}_j(x=0,t)\right)\right]\\
\overline{\mathrm{SAT}}^x_{i,j,3} &= -(\lambda+2\mu)\tau h_x^{-1}\left[h_{NN}^{-1}\delta_{iN}\left(u_{N,j}-\bar{u}_j(x=1,t)\right)-h_{00}^{-1}\delta_{i0}\left(u_{0,j}-\bar{u}_j(x=0,t)\right)\right]\\
\overline{\mathrm{SAT}}^x_{i,j,4} &= -\mu\tau h_x^{-1}\left[h_{NN}^{-1}\delta_{iN}\left(v_{N,j}-\bar{v}_j(x=1,t)\right)-h_{00}^{-1}\delta_{i0}\left(v_{0,j}-\bar{v}_j(x=0,t)\right)\right]\\
\overline{\mathrm{SAT}}^x_{i,j,5} &= -\lambda\tau h_x^{-1}\left[h_{NN}^{-1}\delta_{iN}\left(u_{N,j}-\bar{u}_j(x=1,t)\right)-h_{00}^{-1}\delta_{i0}\left(u_{0,j}-\bar{u}_j(x=0,t)\right)\right]
\end{aligned} \tag{21}$$

and in the y-direction we get, similarly,

$$\begin{aligned}
\overline{\mathrm{SAT}}^y_{i,j,1} &= -c_s\tau h_y^{-1}\left[h_{MM}^{-1}\delta_{jM}\left(u_{i,M}-\bar{u}_i(y=1,t)\right)+h_{00}^{-1}\delta_{j0}\left(u_{i,0}-\bar{u}_i(y=0,t)\right)\right]\\
\overline{\mathrm{SAT}}^y_{i,j,2} &= -c_p\tau h_y^{-1}\left[h_{MM}^{-1}\delta_{jM}\left(v_{i,M}-\bar{v}_i(y=1,t)\right)+h_{00}^{-1}\delta_{j0}\left(v_{i,0}-\bar{v}_i(y=0,t)\right)\right]\\
\overline{\mathrm{SAT}}^y_{i,j,3} &= -\lambda\tau h_y^{-1}\left[h_{MM}^{-1}\delta_{jM}\left(v_{i,M}-\bar{v}_i(y=1,t)\right)-h_{00}^{-1}\delta_{j0}\left(v_{i,0}-\bar{v}_i(y=0,t)\right)\right]\\
\overline{\mathrm{SAT}}^y_{i,j,4} &= -\mu\tau h_y^{-1}\left[h_{MM}^{-1}\delta_{jM}\left(u_{i,M}-\bar{u}_i(y=1,t)\right)-h_{00}^{-1}\delta_{j0}\left(u_{i,0}-\bar{u}_i(y=0,t)\right)\right]\\
\overline{\mathrm{SAT}}^y_{i,j,5} &= -(\lambda+2\mu)\tau h_y^{-1}\left[h_{MM}^{-1}\delta_{jM}\left(v_{i,M}-\bar{v}_i(y=1,t)\right)-h_{00}^{-1}\delta_{j0}\left(v_{i,0}-\bar{v}_i(y=0,t)\right)\right]
\end{aligned} \tag{22}$$

Remark

There is one small technical detail to consider: In a corner, say $i=0$, $j=0$ where the bottom and left edges meet, we must choose whether to impose the boundary condition $u_{0,0}=\bar{u}_0(x=0,t)$ from the boundary condition in the y-direction, *or* $u_{0,0}=\bar{u}_0(y=0,t)$ from the x-direction and then only include the SAT expression corresponding to either one of these cases. The same goes for the variable v and the other three corners.

3.6 Time integration

The system (20) of ordinary differential equations can readily be solved by the classical 4th order explicit Runge–Kutta method. Calling the right-hand side of (20) $\mathbf{f}(t_n,\hat{\mathbf{q}}^n)$ at the time level n, we advance the solution to level $n+1$ by performing the steps

$$\begin{aligned}
\mathbf{k}_1 &= \mathbf{f}(t_n,\hat{\mathbf{q}}^n)\\
\mathbf{k}_2 &= \mathbf{f}\left(t_n+\frac{\Delta t}{2},\hat{\mathbf{q}}^n+\frac{\Delta t}{2}\mathbf{k}_1\right)\\
\mathbf{k}_3 &= \mathbf{f}\left(t_n+\frac{\Delta t}{2},\hat{\mathbf{q}}^n+\frac{\Delta t}{2}\mathbf{k}_2\right)\\
\mathbf{k}_4 &= \mathbf{f}(t_n+\Delta t,\hat{\mathbf{q}}^n+\Delta t\mathbf{k}_3)\\
\hat{\mathbf{q}}^{n+1} &= \hat{\mathbf{q}}^n+\frac{\Delta t}{6}(\mathbf{k}_1+2\mathbf{k}_2+2\mathbf{k}_3+\mathbf{k}_4).
\end{aligned}$$

Remark

If the time-dependent boundary conditions for the classical 4th order Runge–Kutta method are injected at the end of each internal stage, then the cancellation of errors in the Taylor expansion of the method is ruined and the 4th order convergence rate is lost, cf. [7, 3]. The first order error $\mathcal{O}(\Delta t)$ at the boundary leads to second order convergence only. On the other hand, injecting the value on the boundary only after the final stage gives the theoretical convergence but at the cost of a more restrictive CFL condition. With the SAT method, the boundary conditions are in effect part of the derivative operator and should be evaluated at the same time as the current stage in the Runge–Kutta method.

3.6.1 Choice of time step

Using explicit time integration for the discrete equations, we need to make sure that the CFL condition is satisfied. The maximum CFL number depends on which particular time and space discretization we use, but we can generally state that a condition of the form

$$\Delta t \le \frac{\mathrm{CFL}}{c_p}\min\left\{\frac{h_\xi}{\max_{i,j}\sqrt{(\xi_x^2)_{i,j}+(\xi_y^2)_{i,j}}},\frac{h_\eta}{\max_{i,j}\sqrt{(\eta_x^2)_{i,j}+(\eta_y^2)_{i,j}}}\right\} \tag{23}$$

must hold, as c_p is always the largest wave speed. For a 1D problem with periodic boundary conditions, the maximum CFL number when using the 4th order explicit Runge–Kutta method in time and a 6th order central difference method in space, is about 1.7. Here, in 2D with non-periodic boundaries, we expect the maximum CFL number to be a bit lower, say 1.3 grosso modo.

3.7 Explicit filter

Waves with wave number $k = \pi/h$ where h is the grid spacing, are not damped by standard central difference operators like the sixth order one which our SBP operator Q corresponds to in the interior. To get rid of these waves, we use an explicit filter [13] which is applied to the solution after each time step. Defining the Kronecker products $\mathbf{D}_\xi^{(6)} = D_\xi^{(6)} \otimes I_M \otimes I_5$ and $\mathbf{D}_\eta^{(6)} = I_N \otimes D_\eta^{(6)} \otimes I_5$ the filtered solution at time level $n+1$ is obtained as

$$\hat{\mathbf{q}}^{n+1} \longleftarrow \hat{\mathbf{q}}^{n+1} - \left[\mathbf{D}_\xi^{(6)}\hat{\mathbf{q}} + \mathbf{D}_\eta^{(6)}\hat{\mathbf{q}}\right]^{n+1} \tag{24}$$

where $D_\xi^{(p)}\mathbf{u}$ represents the central difference approximation

$$(D_\xi^{(p)}\mathbf{u})_{i,j} = \frac{(-1)^{p/2}}{2^p}\delta_\xi^{(p)} u_{i,j} \tag{25}$$

and $\delta_\xi^{(2)} u_{i,j} = u_{i+1,j} - 2u_{i,j} + u_{i-1,j}$ is the finite difference approximation of $h_\xi^2 \dfrac{\partial^2 u(ih_\xi, jh_\eta)}{\partial \xi^2}$ with analogous definitions for the η-direction. With $p = 6$, the filter suppresses modes with the highest wave number $k = \pi/h$ while modes in the region $k \leq 0.8/h$ are essentially undamped.

4 Numerical experiments

4.1 2D test case

We consider now a simple test for our 2D discretization: a square domain occupying the region $-1 \leq x \leq 1$, $-1 \leq y \leq 1$ in dimensionless variables. At $t = 0$ we give an initial condition for the stress component $g(x,y,t=0) = g_0(x,y)$ while all other variables are initially zero. The initial condition is defined by

$$g_0(x,y) = s(2r_1 + 0.5) - s(2r_2 + 0.5) \tag{26}$$

where $r_1^2 = (x-0.5)^2 + y^2$, $r_2^2 = (x+0.5)^2 + y^2$ and

$$s(r) = \begin{cases} \exp(-1/r - 1/(1-r) + 4), & \text{if } 0 < r < 1 \\ 0, & \text{otherwise.} \end{cases} \tag{27}$$

Thus, $g_0(x,y)$ is a smooth function with infinitely many derivatives and compact support, representing two sources located at $(\pm 0.5, 0)$. The material parameters are $\lambda = \mu = 1.0$ and density $\rho = 1.0$. We integrate the solution with CFL number 0.8 and impose homogeneous Dirichlet boundary conditions for u and v using the SAT approach (21-22). Hence no displacement is imposed on the boundary. To obtain the displacement $\delta(t) = \delta(0) + \int_0^t u(\tau)d\tau$, we integrate the velocity numerically at each grid point using the 4th order explicit Runge–Kutta method. We plot the solution evaluated at time $t = 0.5$ in figures 1(a), 1(c) and 2. Since the largest wave speed $c_p = \sqrt{(\lambda + 2\mu)/\rho} = \sqrt{3}$, at $t = 0.5$ the P-wave will have reached and been reflected from the right boundary which is situated a distance 0.5 from the center of the source.

The numerical solution to the 2D test case is shown in Figures 1(a) and 1(c) computed on a 2049×2049 grid, and in Figures 1(b) and 1(d) is shown the magnitude of the error in the solution on a 513×513 grid when compared with the solution on the finest grid. The positions of the wave fronts are best seen in the error plots; we see that waves have been reflected on the right and top boundaries and that the error is largest where the wave fronts meet.

As the solution is symmetric with respect to the center lines $x = 0$ and $y = 0$, only the first quadrant is shown. The value of the velocity components at the boundary is zero, as enforced by the SAT term.

For the same set of parameters and initial/boundary conditions, we compute the solution at different grid resolutions and consider the solution on the finest grid to be exact. We can then calculate the error at each grid level and thus determine the convergence rate. We define the 2-norm of the error at any grid level k as

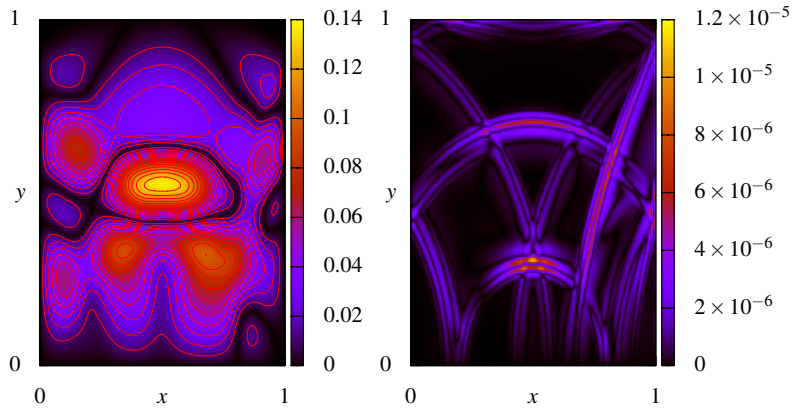

(a) Contour levels spaced 0.01 apart for solution variable u

(b) Error in solution variable u on 513×513 grid

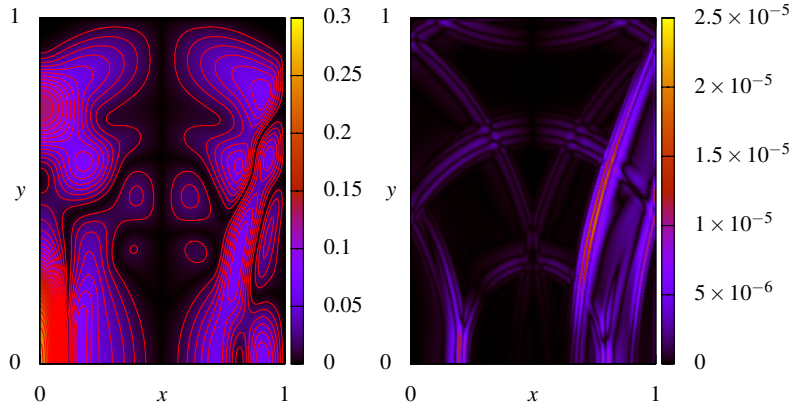

(c) Contour levels spaced 0.01 apart for solution variable v

(d) Error in solution variable v on 513×513 grid

Figure 1: 2D test case in first quadrant: contour plots of velocity components (top) and modulus of displacement vector (bottom) evaluated at $t = 0.5$.

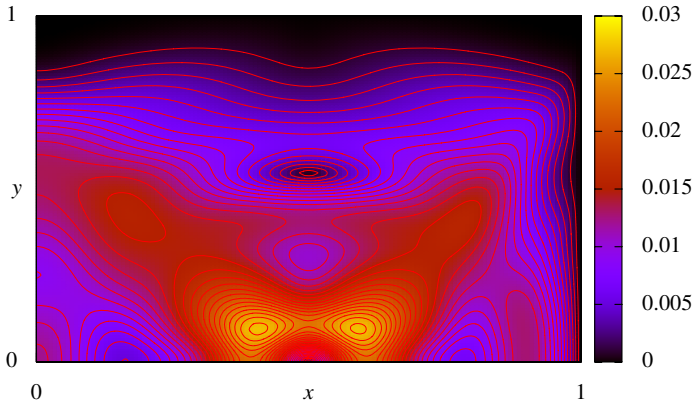

Figure 2: 2D test case: Contour levels spaced 0.001 apart for modulus of displacement vector

$N \times M$	k	$e_2^{(k)}$	$e_\infty^{(k)}$	$\log_2(e_2^{(k+1)}/e_2^{(k)})$	$\log_2(e_\infty^{(k+1)}/e_\infty^{(k)})$
32×32	6	3.646×10^{-2}	7.540×10^{-2}	–	–
64×64	5	6.800×10^{-3}	1.563×10^{-2}	2.423	2.271
128×128	4	8.521×10^{-4}	2.652×10^{-3}	2.996	2.559
256×256	3	7.421×10^{-5}	4.827×10^{-4}	3.521	2.458
512×512	2	4.558×10^{-6}	5.642×10^{-5}	4.025	3.097
1024×1024	1	2.710×10^{-7}	6.456×10^{-6}	4.072	3.128
2048×2048	0	0	0	–	–

Table 6: Errors and convergence rates in 2-norm and maximum norm for 2D test case at $t = 0.5$.

$$e_2^{(k)} = \left[\frac{1}{NM} \sum_{\phi \in \{u,v,f,g,h\}} \sum_{i=0}^{N} \sum_{j=0}^{M} \left| \phi_{i,j}^{(k)} - \phi_{\text{exact},i,j}^{(k)} \right|^2 \right]^{1/2}, \tag{28}$$

where $\phi_{\text{exact}}^{(k)}$ is the restriction of the solution $\phi^{(0)}$ on the finest grid to the grid on level k. The ∞-norm is likewise defined as

$$e_\infty^{(k)} = \max_{\phi \in \{u,v,f,g,h\}} \max_{i,j} |\phi_{i,j}^{(k)} - \phi_{\text{exact},i,j}^{(k)}|.$$

As can be seen in Table 6, the convergence rate in the 2-norm approaches 4 as N and M increase, which is what we expected. However, we do not yet see a fourth order convergence rate in the ∞-norm, but only a little better than third order.

4.2 Wave propagation in 1D

As a second verification case, we consider elastic wave propagation in 1D by not imposing any boundary conditions in one of the two spatial directions. If we assume no variation in the x-direction, we are effectively solving the system $q_t = Bq_y$ with $q = (u, v, f, g, h)^{\mathrm{T}}$. From the characteristic variables in the y-direction (7), we know that a disturbance in u will will travel at speed c_s and a disturbance in v will propagate with wave speed c_p. Thus, if we solve the 1D linear elastic wave equation in a domain $0 \leq y \leq L$ with zero initial conditions and the boundary conditions $\bar{u}(y = 0, t) = \bar{v}(y = 10) = 1$, $\bar{u}(y = 10) = \bar{v}(y = 0) = 0$ we expect a discontinuous solution propagating back and forth in the domain with different speeds for the variables u and v. Numerically, we locate the discontinuities by finding the point where the first derivative of the solution is maximum.

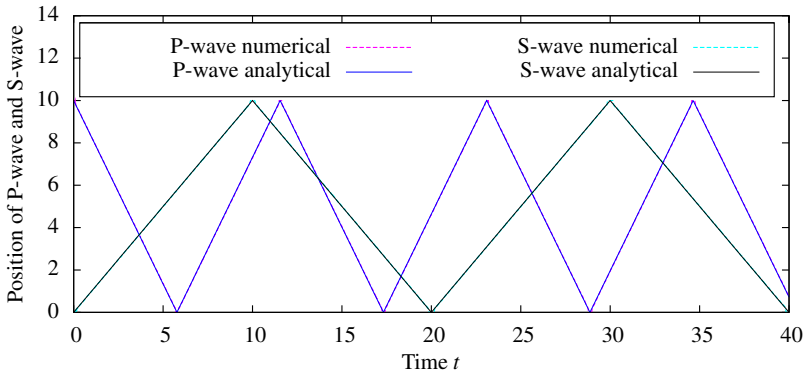

Figure 3: Results for 1D wave propagation experiment: The lines represent the position of the wave-fronts as a function of time. The theoretical position is also plotted but it is hard to distinguish since it is so near the numerically predicted value.

In figure (3) is plotted the analytical and numerically calculated wavefront positions for a domain of length $L = 10$ discretized with 200 points in the direction of propagation. The analytical wave speeds are $c_s = 1$ and $c_p = \sqrt{3}$. The numerical results reproduce the analytical solution quite well as seen in the figure. Surface plots of the solution are shown in figures 4(a) and 4(a). The Gibbs phenomenon is visible near the discontinuities. This simple test case verifies that we get the correct numerical wave speeds in our high order discretization for a discontinuous solution and that the filter does a good job at suppressing the high frequency waves in the solution.

4.3 Manufactured solution

Using the method of manufactured solution [16], we can test the accuracy of the method with reference to an exact solution and without referring to the numerical solution on a finer grid. We choose to consider the rectangle $-1 \leq x \leq 1$, $-1 \leq y \leq 1$ and the vector-valued function

$$\tilde{q} = (\tilde{u}, \tilde{v}, \tilde{f}, \tilde{g}, \tilde{h})^{\mathrm{T}} = (\sin(\pi x/2)\sin(\pi y/2)\sin(\omega t), -\sin(\pi x/4)\sin(\pi y/4)\sin(\omega t), 0, 0, 0)^{\mathrm{T}} \tag{29}$$

with $\omega = 2\pi$. Inserting the function into the continuous equation yields a source term $\tilde{q}_t - A\tilde{q}_x - B\tilde{q}_y$. Including the corresponding source term in the equations forces the function to be the analytical solution. The time dependent boundary conditions given by the analytical solution $\tilde{u}$ and $\tilde{v}$ are enforced on all four boundaries by the SAT procedure.

With a CFL number of 0.8, we evaluated the numerical solution at the time $t = 0.5$, at which the analytical solution is zero. At different grid resolutions, we obtained the results shown in Table 7. Since there are no high frequency components in the solution, we did not use a filter here. In the 2-norm, the order of accuracy is about 3.5. It is unclear why we don't get 4 but it is possible that the time dependence in the source term gives rise to a dominant error term if $\omega\Delta t$ is large.

With the manufactured solution, we can calculate the error exactly at each time level. To see how the CFL number affects the error in the solution, we used a fixed grid of size 129×129 and integrated the manufactured solution up to $t = 4.0$ for different CFL numbers while calculating the error at each time level. The results shown in Figure 5 indicate that a CFL number below 0.2 has little effect on the error in the solution. The error then grows as the CFL number is increased until the solution becomes unstable at CFL $= 1.0$. The error oscillates in time at the same frequency as the driving function. However, there is no overall tendency of an increase in the error.

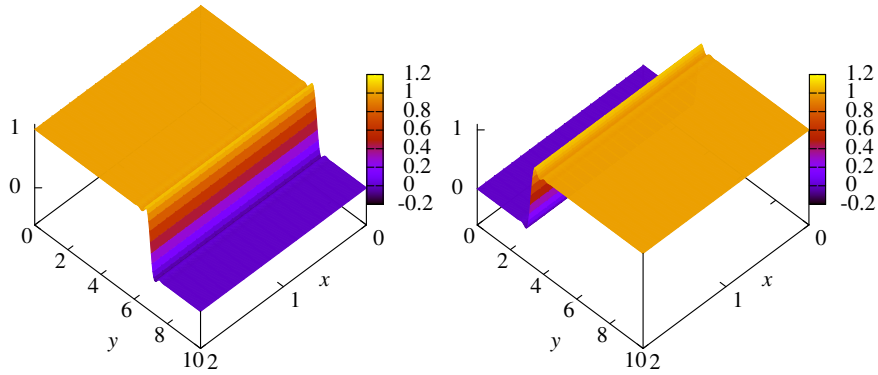

(a) Solution variable u (b) Solution variable v

Figure 4: Results for 1D wave propagation experiment: Surface plot of solution variables at time $t = 27$, CFL $= 0.8$. The boundary conditions are $\bar{u}(y = 0, t) = \bar{v}(y = 10) = 1$, $\bar{u}(y = 10) = \bar{v}(y = 0) = 0$, enforced via the SAT method.

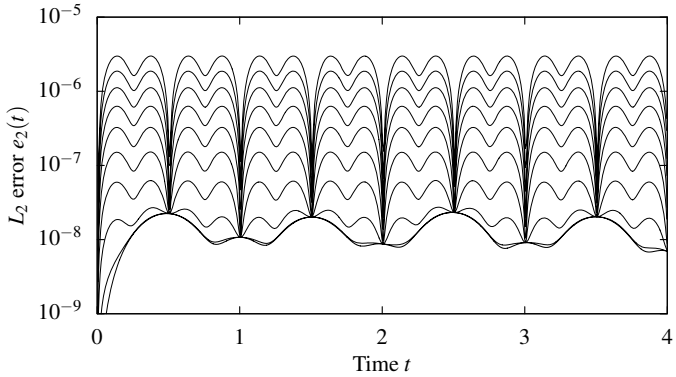

Figure 5: L_2 error as a function of time for different CFL numbers while computing the manufactured solution on a 129×129 grid. The lowest errors are obtained for CFL $= 0.1$ and CFL $= 0.2$ which correspond to the two lowest lines in the graph. The other lines correspond to CFL $= 0.3$ up to and including CFL $= 1.0$.

$N \times M$	k	$e_2^{(k)}$	$e_\infty^{(k)}$	$\log_2(e_2^{(k+1)}/e_2^{(k)})$	$\log_2(e_\infty^{(k+1)}/e_\infty^{(k)})$
32×32	6	4.258×10^{-4}	2.871×10^{-3}	–	–
64×64	5	3.563×10^{-5}	3.917×10^{-4}	3.580	2.873
128×128	4	3.248×10^{-6}	4.495×10^{-5}	3.455	3.123
256×256	3	2.730×10^{-7}	6.293×10^{-6}	3.573	2.836
512×512	2	2.522×10^{-8}	6.225×10^{-7}	3.436	3.338
1024×1024	1	2.215×10^{-9}	8.797×10^{-8}	3.509	2.823

Table 7: Error and convergence rate for manufactured solution in 2- and ∞-norms.

5 Conclusions

We have derived simultaneous approximation terms (SAT) for the 2D linear elastic wave equation in first order form to yield strictly stable high order difference operators for general Dirichlet boundary conditions. The implementation of the SAT approach for a fourth order difference scheme has proved that the convergence rate is indeed fourth order for a test case with smooth data. The advantage of our approach is that Dirichlet boundary conditions can easily be imposed for either the velocity or the stress components which is required for fluid-structure interaction.

Appendix: SAT in transformed coordinates

To obtain SAT expressions for the transformed coordinates we need to find the characteristic variables for the transformed equation where the coefficient matrices are linear combinations of the coefficient matrices in the x- and y-directions

$$\hat{q}_t = ((k_x A + k_y B)\hat{q})_k \tag{30}$$

where $k = \xi, \eta$. We form the linear combination $P(k_x,k_y) = k_x A + k_y B$. The coefficient matrices A and B have the same set of eigenvalues $\Lambda = \mathrm{diag}(c_p, c_s, 0, -c_s, -c_p)$, whereas for the linear combination $P(k_x,k_y)$ we get $\tilde{\Lambda}(k_x,k_y) = (k_x^2 + k_y^2)^{1/2}\Lambda$. To find the linearly independent eigenvectors of $P(k_x,k_y)$, we solve the underdetermined system $(P(k_x,k_y) - \tilde{\lambda}_i I)v_i = 0$ for $i = 1,...,5$. These five eigenvectors v_i become the columns in the matrix

$$T(k_x,k_y) = \begin{bmatrix} k_x\tilde{c}_p/\lambda & -k_y/\bar{k} & 0 & -k_y/\bar{k} & -k_x\tilde{c}_p/\lambda \\ k_y\tilde{c}_p/\lambda & k_x/\bar{k} & 0 & k_x/\bar{k} & -k_y\tilde{c}_p/\lambda \\ k_x^2\alpha + k_y^2 & -2k_xk_y\tilde{c}_s\rho/(\bar{k}r^2) & k_y^2 & 2k_xk_y\tilde{c}_s\rho/(\bar{k}r^2) & k_x^2\alpha + k_y^2 \\ 2k_xk_y\mu/\lambda & \rho\tilde{c}_s & -k_xk_y & -\rho\tilde{c}_s & 2\mu k_xk_y/\lambda \\ k_y^2\alpha + k_x^2 & 2k_xk_y\tilde{c}_s\rho/(\bar{k}r^2) & k_x^2 & -2k_xk_y\tilde{c}_s\rho/(\bar{k}r^2) & k_y^2\alpha + k_x^2 \end{bmatrix} \tag{31}$$

We have some degrees of freedom in choosing T, each column could for example be scaled by any nonzero constant. The inverse of this matrix is obtained with a symbolic computer program, the result being

$$T^{-1}(k_x,k_y) = \frac{1}{2r^2}\begin{bmatrix} \frac{k_x\lambda}{\tilde{c}_p} & \frac{k_y\lambda}{\tilde{c}_p} & \frac{k_x^2}{\alpha r^2} & 2\frac{k_yk_x}{\alpha r^2} & \frac{k_y^2}{\alpha r^2} \\ -k_y\bar{k} & k_x\bar{k} & -\frac{\bar{k}k_xk_y}{\rho\tilde{c}_s} & \frac{\bar{k}^2r^2}{\rho\tilde{c}_s} & \frac{\bar{k}k_xk_y}{\rho\tilde{c}_s} \\ 0 & 0 & -\frac{2\bar{k}}{\alpha} + \frac{4k_y^2}{\beta r^2} & -8\frac{k_xk_y(\lambda+\mu)}{r^2(\lambda+2\mu)} & \frac{2\bar{k}}{\alpha} + 4\frac{k_x^2}{\beta r^2} \\ -k_y\bar{k} & k_x\bar{k} & \frac{\bar{k}k_xk_y}{\rho\tilde{c}_s} & -\frac{\bar{k}^2r^2}{\rho\tilde{c}_s} & -\frac{\bar{k}k_xk_y}{\rho\tilde{c}_s} \\ -\frac{\lambda k_x}{\tilde{c}_p} & -\frac{\lambda k_y}{\tilde{c}_p} & \frac{k_x^2}{\alpha r^2} & 2\frac{k_yk_x}{\alpha r^2} & \frac{k_y^2}{\alpha r^2} \end{bmatrix} \tag{32}$$

where the parameters are defined by $\bar{k} = (k_x^2 - k_y^2)/(k_x^2 + k_y^2)$, $r = (k_x^2 + k_y^2)^{1/2}$, $\tilde{c}_p = rc_p$, $\tilde{c}_s = rc_s$, $\alpha = (\lambda + 2\mu)/\lambda$ and $\beta = \alpha\lambda/\mu$. The astute reader will readily verify that $T^{-1}(k_x,k_y)P(k_x,k_y)T(k_x,k_y) = \tilde{\Lambda}(k_x,k_y)$.

The characteristic variables are $u(k_x,k_y) = T^{-1}(k_x,k_y)\hat{q}$ where $\hat{q} = J^{-1}(u,v,f,g,h)^{\mathrm{T}}$ and since T^{-1} is dense for general coordinates, four of the characteristic variables have contributions from all five physical variables. We form the two sub-vectors corresponding to positive and negative eigenvalues as $u^{\mathrm{I}}(k_x,k_y) = (u_1,u_2)^{\mathrm{T}}$ and $u^{\mathrm{II}}(k_x,k_y) = (u_4,u_5)^{\mathrm{T}}$ with the aim to form boundary conditions with the matrices R and L. At a first glance, it might seem like a hopeless predicament to derive expressions for L, R, g^{I} and g^{II} in transformed coordinates but thanks to the symmetry in $T^{-1}(k_x,k_y)$, we are so lucky that the same L and R as we used for Cartesian coordinates also work for transformed coordinates, since they also isolate the right components of $u^{\mathrm{I,II}}(k_x,k_y)$ in Eq. (15). Eq. (15) now gives our new boundary functions $g^{\mathrm{I}}(k_x,k_y,t)$ and $g^{\mathrm{II}}(k_x,k_y,t)$ as

$$g^{\mathrm{I}}(k_x,k_y,t) = \bar{u}^{\mathrm{I}}(k_x,k_y,k=0,t) - R\bar{u}^{\mathrm{II}}(k_x,k_y,k=0,t), \quad g^{\mathrm{II}}(k_x,k_y,t) = \bar{u}^{\mathrm{II}}(k_x,k_y,k=1,t) - L\bar{u}^{\mathrm{I}}(k_x,k_y,k=1,t)$$

where the functions $\bar{u}^{\mathrm{I,II}}$ are the previously defined $u^{\mathrm{I,II}}$ but with the solution variables substituted for their corresponding boundary conditions. Note that L and R are independent of the direction. For boundary conditions on u and v, we get, using L and R from Tables 1 and 2

$$g^{\mathrm{I}}(k_x,k_y,t) = \frac{J^{-1}}{r^2}\begin{bmatrix} \dfrac{\lambda}{\tilde{c}_p}(k_x\bar{u}(k=1,t)+k_y\bar{v}(k=1,t)) \\ \bar{k}(-k_y\bar{u}(k=1,t)+k_x\bar{v}(k=1,t)) \end{bmatrix} \tag{33}$$

$$g^{\mathrm{II}}(k_x,k_y,t) = \frac{J^{-1}}{r^2}\begin{bmatrix} \bar{k}(-k_y\bar{u}(k=0,t)+k_x\bar{v}(k=0,t)) \\ \dfrac{\lambda}{\tilde{c}_p}(-k_x\bar{u}(k=0,t)-k_y\bar{v}(k=0,t)) \end{bmatrix} \tag{34}$$

where $\bar{u}(k,t),\bar{v}(k,t)$ are the given boundary conditions on u,v on the boundaries. Similarly, for boundary conditions on the stress components using the appropriate R and L, we obtain

$$g^{\mathrm{I}}(k_x,k_y,t) = \frac{J^{-1}}{r^2}\begin{bmatrix} \dfrac{1}{\alpha r^2}(k_x^2\bar{f}(k=1,t)+2k_yk_x\bar{g}(k=1,t)+k_y^2\bar{h}(k=1,t)) \\ \dfrac{\bar{k}}{\rho\tilde{c}_s}(-k_xk_y\bar{f}(k=1,t)+(k_x^2-k_y^2)\bar{g}(k=1,t)+k_xk_y\bar{h}(k=1,t)) \end{bmatrix} \tag{35}$$

$$g^{\mathrm{II}}(k_x,k_y,t) = \frac{J^{-1}}{r^2}\begin{bmatrix} \dfrac{\bar{k}}{\rho\tilde{c}_s}(k_xk_y\bar{f}(k=0,t)-(k_x^2-k_y^2)\bar{g}(k=0,t)-k_xk_y\bar{h}(k=0,t)) \\ \dfrac{1}{\alpha r^2}(k_x^2\bar{f}(k=0,t)+2k_yk_x\bar{g}(k=0,t)+k_y^2\bar{h}(k=0,t)) \end{bmatrix}. \tag{36}$$

These expressions reduce to their Cartesian counterparts for the case when either of k_x,k_y is zero.

Remark

Seemingly, equations (35) and (36) require all three stress components f,g,h to be known on each boundary. However, we know from the characteristic analysis that we can only give information on the two characteristics that enter the computational domain. Typically, the boundary conditions on the stresses come from a traction boundary condition of the form $\sigma n = \bar{t}$ where $\bar{t} = (\bar{t}_x,\bar{t}_y)^{\mathrm{T}}$ is the given traction vector and σ is the Cauchy stress tensor $\begin{bmatrix} f & g \\ g & h \end{bmatrix}$. The unit normal n can be expressed in terms of the coordinate transformation (cf. Figure 6) as $n = (1/r)(k_x,k_y)^{\mathrm{T}}$ and the components of g^{I} and g^{II} can thus be rewritten as

$$g^{\mathrm{I}}(k_x,k_y,t) = \frac{J^{-1}}{r^2}\begin{bmatrix} \dfrac{1}{\alpha r}(k_x\bar{t}_x(k=1,t)+k_y\bar{t}_y(k=1,t)) \\ \dfrac{r\bar{k}}{\rho\tilde{c}_s}(-k_y\bar{t}_x(k=1,t)+k_x\bar{t}_y(k=1,t)) \end{bmatrix}$$

$$g^{\mathrm{II}}(k_x,k_y,t) = \frac{J^{-1}}{r^2}\begin{bmatrix} \dfrac{r\bar{k}}{\rho\tilde{c}_s}(k_y\bar{t}_x(k=0,t)-k_x\bar{t}_y(k=0,t)) \\ \dfrac{1}{\alpha r}(k_x\bar{t}_x(k=0,t)+k_y\bar{t}_y(k=0,t)) \end{bmatrix}$$

and therefore it is sufficient to specify the two parameters $\bar{t}_x$ and $\bar{t}_y$ on each boundary, which does not violate well-posedness.

Remark

Our definition of the unit normal n differs from the traditional notion of an outward unit normal in that our normal is only pointing out of the domain on the lines $\xi = 1$ and $\eta = 1$. On $\xi = 0$ and $\eta = 0$, the outward unit normal is $-n$ in our notation.

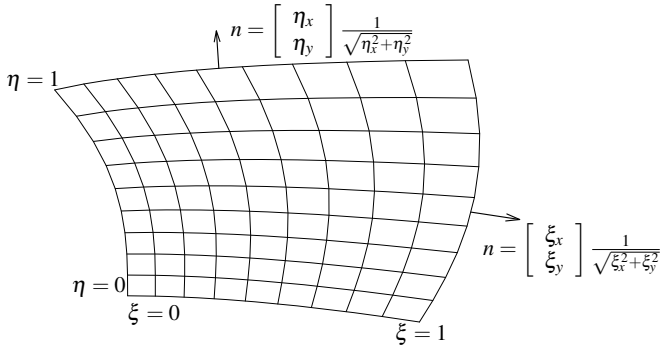

Figure 6: Coordinate transformation

Complete SAT expressions for boundary conditions on u, v

Inserting (33) and (34) into the definition, the following 1D SAT expression in primitive variables and transformed coordinates is obtained:

$$\mathrm{SAT}_i^{(k)}(k_x,k_y,t) = -\frac{\tau J^{-1}}{h_k r^2} \begin{bmatrix} \lambda h_{NN}^{-1}\delta_{iN}[k_x(u_N-\bar{u}(k=1,t))+k_y(v_N-\bar{v}(k=1,t))] \\ \tilde{c}_s\bar{k}(h_{NN})^{-1}\delta_{iN}[-k_y(u_N-\bar{u}(k=1,t))+k_x(v_N-\bar{v}(k=1,t))] \\ 0 \\ \tilde{c}_s\bar{k}(h_{00})^{-1}\delta_{i0}[-k_y(u_0-\bar{u}(k=0,t))+k_x(v_0-\bar{v}(k=0,t))] \\ \lambda h_{00}^{-1}\delta_{i0}[-k_x(u_0-\bar{u}(k=0,t))-k_y(v_0-\bar{v}(k=0,t))] \end{bmatrix} \tag{37}$$

Here, k can be either one of the coordinates ξ, η, i.e. h_k is the grid spacing in either the ξ- or η-direction. N is the maximum index in the corresponding direction. We have used i as general coordinate index. When $k=\eta$, we would instead call the index j and the maximum index would be M. To go back to flow variables, we apply the transformation matrix,

$$\overline{\mathrm{SAT}}_i^{(k)} = T(k_x,k_y)\mathrm{SAT}_i^{(k)}(k_x,k_y) \tag{38}$$

for $k=\xi$ and η. The full expressions are lengthy and add nothing to the discussion so they are omitted here. In 2D, the total SAT expression is then the sum of the two contributions from the two coordinate directions.

$$\widehat{\overline{\mathrm{SAT}}}_{i,j} = \overline{\mathrm{SAT}}_{i,j}^{(\xi)}(\xi_x,\xi_y) + \overline{\mathrm{SAT}}_{i,j}^{(\eta)}(\eta_x,\eta_y) \tag{39}$$

Acknowledgments

The current research has been funded by the Swedish Research Council under the project "Numerical Simulation of Respiratory Flow".

References

[1] D. Appelö and N. A. Petersson. A stable finite difference method for the elastic wave equation on complex geometries with free surfaces. *Commun. Comput. Phys.*, 5(1):84 – 107, 2009.

[2] M. H. Carpenter, D. Gottlieb, and S. Abarbanel. Time-stable boundary conditions for finite-difference schemes solving hyperbolic systems: Methodology and application to high-order compact schemes. *J. Comp. Phys.*, 111:220 – 236, 1994.

[3] M.H. Carpenter, D. Gottlieb, S. Abarbanel, and W.-S. Don. The theoretical accuracy of Runge–Kutta time discretizations for the initial boundary value problem: A study of the boundary error. *SIAM J. Sci. Comp.*, 16(6):1241 – 1252, 1995.

[4] F. Casadei, E. Gabellini, G. Fotia, F. Maggio, and A. Quarteroni. A mortar spectral/finite element method for complex 2d and 3d elastodynamic problems. *Comput. Methods Appl. Mech. Engrg.*, 191:5119 – 5148, 2002.

[5] G. C. Cohen. *Higher-Order Numerical Methods for Transient Wave Equations*. Springer, 2002.

[6] E. Faccioli, F. Maggio, R. Paolucci, and A. Quarteroni. 2d and 3d elastic wave propagation by a pseudo-spectral domain decomposition method. *Journal of Seismology*, 1:237 – 251, 1997.

[7] B. Fornberg. *A Practical Guide to Pseudospectral Methods*. Cambridge University Press, 1998.

[8] B. Fornberg and M. Ghrist. Spatial finite difference approximations for wave-type equations. *SIAM Journal on Numerical Analysis*, 37(1):105 – 130, 2000.

[9] M. Ghrist, B. Fornberg, and T. A. Discoll. Staggered time integrators for wave equations. *SIAM Journal on Numerical Analysis*, 38(3):718 – 741, 2001.

[10] B. Gustafsson. *High order difference methods for time-dependent PDE*. Springer-Verlag Berlin Heidelberg, 2008.

[11] M. Käser and M. Dumbser. An arbitrary high-order discontinuous galerkin method for elastic waves on unstructured meshes - I. The two-dimensional isotropic case with external source terms. *Geophysical Journal International*, 142, 2000.

[12] K. Mattsson, F. Ham, and G. Iaccarino. Stable boundary treatment for the wave equation on second-order form. *J. Sci. Comput.*, 41:366 – 383, 2009.

[13] B. Müller. High order numerical simulation of aeolian tones. *Computers & Fluids*, 37(4):450 – 462, 2008.

[14] S. Nilsson, N.A. Petersson, B. Sjögreen, and H.-O. Kreiss. Stable difference approximations for the elastic wave equation in second order formulation. *SIAM Journal on Numerical Analysis*, 45(5):1902 – 1936, 2007.

[15] J. Nordström and M.H. Carpenter. Boundary and Interface Conditions for High-Order Finite-Difference Methods Applied to the Euler and Navier–Stokes Equations. *JCP*, 148:621 – 645, 1999.

[16] P.J. Roache. *Verification and validation in computational science and engineering*. Hermosa Publishers, 1998.

[17] B. Strand. Summation by parts for finite difference approximations for d/dx. *J. Comput. Physics*, 110:47 – 67, 1994.

PAPER 6

M. Larsson, B. Müller: High order numerical simulation of fluid-structure interaction in human phonation, *Proceedings of ECCOMAS CFD 2010 conference*, Lisbon, Portugal, 14–17 June 2010.

V European Conference on Computational Fluid Dynamics
ECCOMAS CFD 2010
J. C. F. Pereira and A. Sequeira (Eds)
Lisbon, Portugal,14-17 June 2010

HIGH ORDER NUMERICAL SIMULATION OF FLUID-STRUCTURE INTERACTION IN HUMAN PHONATION

Martin Larsson and Bernhard Müller

Norwegian University of Science and Technology
Department of Energy and Process Engineering, 7491 Trondheim, Norway
e-mail: {martin.larsson,bernhard.muller}@ntnu.no

Key words: Fluid-Structure Interaction, High Order Method, Finite Difference, Phonation

Abstract. *Fluid-structure interaction in a simplified two-dimensional model of the larynx is considered in order to study human phonation. The flow is driven by an imposed pressure gradient across the glottis and interacts with the moving vocal folds in a self-sustained oscillation. The flow is computed by solving the 2D compressible Navier–Stokes equations using a high order finite difference method, which has been constructed to be strictly stable for linear hyperbolic and parabolic problems. The motion of the vocal folds is obtained by integrating the linear elastic wave equation using a similar high order difference method as for the flow equations. Fluid and structure interact in a two-way coupling. In each time step at the fluid-structure interface, the structure provides the fluid with new no-slip boundary conditions and new grid velocities, and the fluid provides the structure with new traction boundary conditions which are imposed via the simultaneous approximation term (SAT) approach.*

1 INTRODUCTION

Fluid-structure interaction (FSI) occurs when a flexible structure interacts with a fluid. The fluid flow exerts a stress on the structure which causes it to deform, thereby generating a new geometry for the fluid flow. A direct consequence of FSI in the vocal tract is voice generation, where the motion of the soft tissue of the vocal folds interacts dynamically with the glottal airflow to produce sound. The self-sustained oscillations of the vocal folds can be explained by the Bernoulli principle which states that in the absence of gravity for inviscid incompressible steady flow, the velocity v, pressure p and density ρ are related by $p + \rho v^2/2 = \text{const}$. The vocal folds being closed in their equilibrium position, initially at rest, are forced apart by the increasing lung pressure. As the air starts flowing, the velocity in the glottis increases and thus the pressure must decrease according to the Bernoulli principle. The pressure drop together with restoring elastic forces results in a closure of the vocal folds and a build-up of pressure. This cycle then repeats itself, driven only by the lung pressure. The computational challenge in aeroelastic simulations lies in dealing with unsteady flows at high Reynolds numbers, large deformations, moving interfaces, fluid-structure interaction and intrinsically 3D motion [3].

In this paper, we employ a high order finite difference approach based on summation by parts (SBP) operators [16, 5, 4] to solve the compressible Navier–Stokes equations and the linear elastic wave equation on first order form. Fluid and structure interact in a two-way coupling, meaning that fluid stresses deform the flexible structure which in turn causes the fluid to conform to the new structural boundary via boundary conditions. The approach has been tested for a 2D model of the larynx and the vocal folds.

2 GOVERNING EQUATIONS

2.1 Compressible Navier–Stokes equations

The perturbation formulation is used to minimize cancellation errors when discretizing the Navier–Stokes equations for compressible low Mach number flow [15, 12]. The 2D compressible Navier–Stokes equations in conservative form can be expressed in perturbation form as [13, 8]

$$U'_t + F^{c\prime}_x + G^{c\prime}_y = F^{v\prime}_x + G^{v\prime}_y , \tag{1}$$

where the vector U' denotes the perturbation of the conservative variables with respect to the stagnation values. U' and the inviscid (superscript c) and viscous (superscript v) flux vectors are e.g. defined in [8].

General moving geometries are treated by a time dependent coordinate transformation $\tau = t$, $\xi = \xi(t, x, y)$, $\eta = \eta(t, x, y)$. The transformed 2D conservative compressible Navier–Stokes equations in perturbation form read [8]

$$\hat{U}'_\tau + \hat{F}'_\xi + \hat{G}'_\eta = 0 , \tag{2}$$

where $\hat{U}' = J^{-1}U'$, $\hat{F}' = J^{-1}(\xi_t U' + \xi_x(F^{c\prime} - F^{v\prime}) + \xi_y(G^{c\prime} - G^{v\prime}))$ and $\hat{G}' = J^{-1}(\eta_t U' + \eta_x(F^{c\prime} - F^{v\prime}) + \eta_y(G^{c\prime} - G^{v\prime}))$.

No-slip adiabatic wall boundary conditions and the Navier–Stokes Characteristic Boundary Conditions (NSCBC) technique by Poinsot and Lele in [14] are employed at the outflow [9]. At the inflow, pressure, temperature and velocity in the y-direction are imposed as $p = p_{\text{atm}} + \Delta p, T = T_0 = 310\,\text{K}$, and $v = 0$, respectively.

2.2 Linear elastic wave equation

The 2D linear elastic wave equation written as a first order hyperbolic system reads in Cartesian coordinates

$$q_t = Aq_x + Bq_y, \tag{3}$$

where the unknown vector $q = (u, v, f, g, h)^{\text{T}}$ contains the velocity components u, v and the stress components f, g, h and the coefficient matrices A, B (cf. e.g. [2, 11, 10]) depend on the the Lamé parameters λ, μ and the density ρ which are here all taken to be constant in space and time.

The linear combination $P(k_x, k_y) = k_x A + k_y B$ can be diagonalized with real eigenvalues and linearly independent eigenvectors. The eigenvalue matrix is defined as the diagonal matrix with the eigenvalues of $P(k_x, k_y)$ in decreasing order,

$$\tilde{\Lambda}(k_x, k_y) = (k_x^2 + k_y^2)^{1/2}\text{diag}(c_p, c_s, 0, -c_s, -c_p) = \text{diag}\left\{\tilde{\lambda}_i(k_x, k_y)\right\}_{i=1}^{5}, \tag{4}$$

where the wave speeds are $c_p = \sqrt{(\lambda + 2\mu)/\rho}$ and $c_s = \sqrt{\mu/\rho}$, referred to as primary and secondary (or shear) wave velocity, respectively.

To treat curvilinear grids we introduce the mapping $x = x(\xi, \eta)$, $y = y(\xi, \eta)$. The Jacobian determinant J of the transformation is given by $J^{-1} = x_\xi y_\eta - x_\eta y_\xi$ and the linear elastic wave equation can then be written as

$$\hat{q}_t = (\hat{A}\hat{q})_\xi + (\hat{B}\hat{q})_\eta \tag{5}$$

where the hats signify that the quantities are in transformed coordinates, i.e. $\hat{q} = J^{-1}q$, $\hat{A} = \xi_x A + \xi_y B$ and $\hat{B} = \eta_x A + \eta_y B$.

2.3 Characteristic variables

In order to describe the SAT expressions in transformed coordinates we need to find the characteristic variables for the transformed equation in which the coefficient matrices are linear combinations of the coefficient matrices in the x- and y-directions.

$$\hat{q}_t = ((k_x A + k_y B)\hat{q})_k \tag{6}$$

where $k = \xi, \eta$. We form the linear combination $P(k_x, k_y) = k_x A + k_y B$. The coefficient matrices A and B have the same set of eigenvalues $\Lambda = \text{diag}(c_p, c_s, 0, -c_s, -c_p)$, whereas for the linear combination $P(k_x, k_y)$ we get $\tilde{\Lambda}(k_x, k_y) = (k_x^2 + k_y^2)^{1/2}\Lambda$. To find the linearly

independent eigenvectors of $P(k_x, k_y)$, we solve the underdetermined system $(P(k_x, k_y) - \tilde{\lambda}_i I)v_i = 0$ for $i = 1, ..., 5$. These five eigenvectors v_i become the columns in the matrix

$$T(k_x, k_y) = \begin{bmatrix} k_x\tilde{c}_p/\lambda & -k_y/\bar{k} & 0 & -k_y/\bar{k} & -k_x\tilde{c}_p/\lambda \\ k_y\tilde{c}_p/\lambda & k_x/\bar{k} & 0 & k_x/\bar{k} & -k_y\tilde{c}_p/\lambda \\ k_x^2\alpha + k_y^2 & -2k_xk_y\tilde{c}_s\rho/(\bar{k}r^2) & k_y^2 & 2k_xk_y\tilde{c}_s\rho/(\bar{k}r^2) & k_x^2\alpha + k_y^2 \\ 2k_xk_y\mu/\lambda & \rho\tilde{c}_s & -k_xk_y & -\rho\tilde{c}_s & 2\mu k_xk_y/\lambda \\ k_y^2\alpha + k_x^2 & 2k_xk_y\tilde{c}_s\rho/(\bar{k}r^2) & k_x^2 & -2k_xk_y\tilde{c}_s\rho/(\bar{k}r^2) & k_y^2\alpha + k_x^2 \end{bmatrix} \quad (7)$$

We have some degrees of freedom in choosing T, because each column can be scaled by any nonzero constant. The inverse of this matrix is obtained with a symbolic computer program, the result being

$$T^{-1}(k_x, k_y) = \frac{1}{2r^2}\begin{bmatrix} \frac{k_x\lambda}{\tilde{c}_p} & \frac{k_y\lambda}{\tilde{c}_p} & \frac{k_x^2}{\alpha r^2} & 2\frac{k_yk_x}{\alpha r^2} & \frac{k_y^2}{\alpha r^2} \\ -k_y\bar{k} & k_x\bar{k} & -\frac{\bar{k}k_xk_y}{\rho\tilde{c}_s} & \frac{\bar{k}^2r^2}{\rho\tilde{c}_s} & \frac{\bar{k}k_xk_y}{\rho\tilde{c}_s} \\ 0 & 0 & -\frac{2\bar{k}}{\alpha} + \frac{4k_y^2}{\beta r^2} & -8\frac{k_xk_y(\lambda+\mu)}{r^2(\lambda+2\mu)} & \frac{2\bar{k}}{\alpha} + 4\frac{k_x^2}{\beta r^2} \\ -k_y\bar{k} & k_x\bar{k} & \frac{\bar{k}k_xk_y}{\rho\tilde{c}_s} & -\frac{\bar{k}^2r^2}{\rho\tilde{c}_s} & -\frac{\bar{k}k_xk_y}{\rho\tilde{c}_s} \\ -\frac{\lambda k_x}{\tilde{c}_p} & -\frac{\lambda k_y}{\tilde{c}_p} & \frac{k_x^2}{\alpha r^2} & 2\frac{k_yk_x}{\alpha r^2} & \frac{k_y^2}{\alpha r^2} \end{bmatrix} \quad (8)$$

where the parameters are defined by $\bar{k} = (k_x^2 - k_y^2)/(k_x^2 + k_y^2)$, $r = (k_x^2 + k_y^2)^{1/2}$, $\tilde{c}_p = rc_p$, $\tilde{c}_s = rc_s$, $\alpha = (\lambda + 2\mu)/\lambda$ and $\beta = \alpha\lambda/\mu$. For all directions (k_x, k_y) we have that $T^{-1}(k_x, k_y)P(k_x, k_y)T(k_x, k_y) = \tilde{\Lambda}(k_x, k_y)$. The transformation to characteristic variables u is given by $u^{(k)} = T^{-1}(k_x, k_y)\hat{q}$ for each of the two coordinate directions $k = \xi, \eta$. The transformation back to flow variables is given by $\hat{q} = T(k_x, k_y)u^{(k)}$.

3 STRICTLY STABLE HIGH ORDER DIFFERENCE METHOD

3.1 Energy method

The energy method is a general technique to prove sufficient conditions for well-posedness of partial differential equations (PDE) and stability of difference methods with general boundary conditions.

Consider the solution of the model problem in 1D with

$$u_t = \lambda u_x,\ \lambda > 0,\ 0 \le x \le 1,\ t \ge 0,\ u(x, 0) = f(x),\ u(1, t) = g(t). \quad (9)$$

The symbol λ represents here a general eigenvalue for the hyperbolic system and should not be confused with the Lamé parameter. Define the L_2 scalar product for real functions

v and w on the interval $0 \leq x \leq 1$ as

$$(v, w) = \int_0^1 v(x)w(x)dx \tag{10}$$

which defines a norm of the continuous solution at some time t and an energy $E(t) = ||u(\cdot, t)||^2 = (u, u)$. Using integration by parts $(v, w_x) = v(1, t)w(1, t) - v(0, t)w(0, t) - (v_x, w)$, we get $\frac{dE}{dt} = \frac{d||u||^2}{dt} = (u_t, u) + (u, u_t) = \lambda[(u_x, u) + (u, u_x)] = \lambda[(u_x, u) + [u^2]_0^1 - (u_x, u)] = \lambda[u^2(1, t) - u^2(0, t)]$. If $\lambda > 0$, the boundary condition $u(1, t) = 0$ yields a non-growing solution (note that periodic boundary conditions would also yield a non-growing solution), i.e. $E(t) \leq E(0) = ||f(x)||^2$. Thus, the energy of the solution is bounded by the energy of the initial data. Hence the problem is well-posed.

3.2 Summation by parts operators

The idea behind the summation by parts technique (cf. e.g. [4]) is to use an operator Q which satisfies the corresponding discrete property as the integration by parts of the continuous function, called the summation by parts (SBP) property. For the numerical solution of (9), we introduce the equidistant grid $x_j = jh$, $j = 0, ..., N$, $h = 1/N$, and a solution vector containing the solution at the discrete grid points, $\mathbf{u} = (u_0(t), u_1(t), ..., u_N(t))^{\mathrm{T}}$. The semi-discrete problem can be stated using a difference operator Q approximating the first derivative,

$$\frac{d\mathbf{u}}{dt} = \lambda Q\mathbf{u}, \; u_i(0) = f(x_i). \tag{11}$$

We also define a discrete scalar product and corresponding norm and energy by

$$(\mathbf{u}, \mathbf{v})_h = h\sum_{i,j} h_{ij}u_i v_j = h\mathbf{u}^{\mathrm{T}}H\mathbf{v}, \quad E_h(t) = ||\mathbf{u}||_h^2 = (\mathbf{u}, \mathbf{u})_h, \tag{12}$$

where the symmetric and positive definite norm matrix $H = \mathrm{diag}(H_L, I, H_R)$ has components h_{ij}. In order for (12) to define a scalar product, H_L and H_R must be symmetric and positive definite. We say that the scalar product satisfies the summation by parts property (SBP), if

$$(\mathbf{u}, Q\mathbf{v})_h = u_N v_N - u_0 v_0 - (Q\mathbf{u}, \mathbf{v})_h. \tag{13}$$

It can be seen that this property is satisfied if the matrix $G = HQ$ satisfies the condition that $G + G^{\mathrm{T}} = \mathrm{diag}(-1, 0, ..., 0, 1)$. If Q and its corresponding norm matrix H satisfy the SBP property (13), then the energy method for the discrete problem yields:

$$\frac{dE_h}{dt} = \frac{d||u||_h^2}{dt} = (u_t, u)_h + (u, u_t)_h = \lambda[(Qu, u)_h + (u, Qu)_h] \tag{14}$$

$$= \lambda[(Qu, u)_h + u_N^2 - u_0^2 - (Qu, u)_h] = \lambda[u_N^2 - u_0^2]. \tag{15}$$

How to obtain $dE_h/dt \leq 0$ is the topic of the next section.

For diagonal H_L and H_R there exist difference operators Q accurate to order $\mathcal{O}(h^{2s})$ in the interior and $\mathcal{O}(h^s)$ near the boundaries for $s = 1, 2, 3$ and 4. These operators have an effective order of accuracy $\mathcal{O}(h^{s+1})$ in the entire domain. Explicit forms of such operators Q and norm matrices H were derived by Strand [16].

For this study, we use an SBP operator based on the central sixth order explicit finite difference operator ($s = 3$) which has been modified near the boundaries in order to satisfy the SBP property giving an effective $\mathcal{O}(h^4)$ order of accuracy in the whole domain.

3.3 Simultaneous approximation term

Since one of the terms in (15) is non-negative, strict stability does not follow when using the injection method for the summation by parts operator, i.e. by using $u_N(t) = g(t)$. In contrast, the simultaneous approximation term (SAT) method is an approach where a linear combination of the boundary condition and the differential equation is solved at the boundary. This leads to a weak imposition of the physical boundary conditions. The imposition of SAT boundary conditions is accomplished by adding a source term to the difference operator, proportional to the difference between the value of the discrete solution u_N and the boundary condition to be fulfilled. The SAT method for the semidiscrete advection equation (11) can be expressed as

$$\frac{d\mathbf{u}}{dt} = \lambda Q\mathbf{u} - \lambda\tau\mathbf{S}(u_N - g(t))$$

where $\mathbf{S} = h^{-1}H^{-1}(0, 0, ..., 0, 1)^{\mathrm{T}}$ and τ is a free parameter.

The added term does not alter the accuracy of the scheme since it vanishes when the analytical solution is substituted. Thus, we can imagine the SAT expression as a modification to the difference operator so that we are effectively solving an equation $\mathbf{u}_t = \lambda\tilde{Q}\mathbf{u}$ with $\tilde{Q} = Q + Q^{\mathrm{sat}}$ without imposing the boundary conditions directly. When H is diagonal, the scheme is only modified at one point on the boundary. We can now show that this scheme is strictly stable for $g(t) = 0$. The energy rate for the solution of the semi-discrete equation is $\frac{dE_h}{dt} = \frac{d||u||_h^2}{dt} = (\mathbf{u}_t, \mathbf{u})_h + (\mathbf{u}, \mathbf{u}_t)_h = \lambda[(\mathbf{u}, Q\mathbf{u} - \tau\mathbf{S}u_N)_h + (Q\mathbf{u} - \tau\mathbf{S}u_N, \mathbf{u})_h] = \lambda[(\mathbf{u}, Q\mathbf{u})_h - \tau(\mathbf{u}, \mathbf{S})_h u_N + (Q\mathbf{u}, \mathbf{u})_h - \tau(\mathbf{S}, \mathbf{u})_h u_N] = \lambda[(1-2\tau)u_N^2 - u_0^2]$ since $(\mathbf{S}, \mathbf{u})_h = (\mathbf{u}, \mathbf{S})_h = h\mathbf{u}^{\mathrm{T}}Hh^{-1}H^{-1}(0, 0, ..., 0, 1)^{\mathrm{T}} = u_N$. The discretization is time stable if $\tau \geq 1/2$.

The extension to hyperbolic systems (cf. [1]) of the strictly stable SAT method for hyperbolic systems $u_t = \Lambda u_x$ in one space dimension with diagonal coefficient matrices (r unknowns and r equations) is done in the following way. The coefficient matrix Λ is chosen such that the eigenvalues are in descending order, i.e. $\lambda_1 > \lambda_2 > ... > \lambda_k > 0 > \lambda_{k+1} > ... > \lambda_r$. The solution vector is split into two parts corresponding to positive and negative eigenvalues $u^{\mathrm{I}} = (u^{(1)}, ..., u^{(k)})^{\mathrm{T}}$ and $u^{\mathrm{II}} = (u^{(k+1)}, ..., u^{(r)})^{\mathrm{T}}$, where $u^{(i)}$ is the eigenvector, i.e. the characteristic variable corresponding to the eigenvalue $\lambda^{(i)}$. We define $\mathbf{u}^{\mathrm{I}} = (\mathbf{u}^{(1)}, ..., \mathbf{u}^{(k)})^{\mathrm{T}}$ and $\mathbf{u}^{\mathrm{II}} = (\mathbf{u}^{(k+1)}, ..., \mathbf{u}^{(r)})^{\mathrm{T}}$, where the components $\mathbf{u}^{(i)}$ are grid functions of length $N + 1$.

For the components in $\mathbf{u}^{\mathrm{I}}$ we have boundary conditions at $x = 1$, and for $\mathbf{u}^{\mathrm{II}}$ we need to specify boundary conditions at $x = 0$, as this is required for well-posedness.

Since we are here dealing with characteristic variables, we need to transform our physical boundary conditions to boundary conditions for the characteristic variables. This is done by the boundary functions $\mathbf{g}^{\mathrm{I}}(t) = (g^{(1)}(t), ..., g^{(k)}(t))$, $\mathbf{g}^{\mathrm{II}}(t) = (g^{(k+1)}(t), ..., g^{(r)}(t))$ and the coupling matrices R and L defined by

$$\mathbf{u}^{\mathrm{I}}(1,t) = R\mathbf{u}^{\mathrm{II}}(1,t) + \mathbf{g}^{\mathrm{I}}(t), \quad \mathbf{u}^{\mathrm{II}}(0,t) = L\mathbf{u}^{\mathrm{I}}(0,t) + \mathbf{g}^{\mathrm{II}}(t). \tag{16}$$

The SAT method is then:

$$\begin{array}{rll} \frac{d\mathbf{u}^{(i)}}{dt} = & \lambda_i Q\mathbf{u}^{(i)} - \lambda_i \tau \mathbf{S}^{(i)}(\mathbf{u}_N^{(i)} - (R\mathbf{u}^{\mathrm{II}})_N^{(i)} - g^{(i)}(t)), & 1 \le i \le k \\ \frac{d\mathbf{u}^{(i)}}{dt} = & \lambda_i Q\mathbf{u}^{(i)} + \lambda_i \tau \mathbf{S}^{(i)}(\mathbf{u}_0^{(i)} - (L\mathbf{u}^{\mathrm{I}})_0^{(i-k)} - g^{(i)}(t)), & k+1 \le i \le r \end{array} \tag{17}$$

where $\mathbf{S}^{(i)} = h^{-1}H^{-1}(0, 0, ..., 1)^{\mathrm{T}}$ for $1 \le i \le k$ and $\mathbf{S}^{(i)} = h^{-1}H^{-1}(1, 0, ..., 0)^{\mathrm{T}}$ for $k+1 \le i \le r$. Regarding the notation, $(R\mathbf{u}^{\mathrm{II}})_N^{(i)}$ should be interpreted as follows: $\mathbf{u}^{\mathrm{II}}$ is an $(r-k)\times 1$ vector where each component is a grid function of length $N+1$. Multiplying R (being a $k \times (r-k)$ matrix) with $\mathbf{u}^{\mathrm{II}}$ yields a new vector of grid functions ($k \times 1$ vector). Take the (i)th grid function in this vector and finally the Nth component in the resulting grid function. As shown in [1], the SAT method is both stable and time stable provided that

$$\frac{1 - \sqrt{1 - |R||L|}}{|R||L|} \le \tau \le \frac{1 + \sqrt{1 - |R||L|}}{|R||L|} \tag{18}$$

with the additional constraint that $|R||L| \le 1$, where the matrix norm is defined as $|R| = \rho(R^T R)^{1/2}$ and ρ is the spectral radius.

4 SAT EXPRESSIONS FOR THE LINEAR ELASTIC WAVE EQUATION

Notation for boundary conditions

We adopt the notation $u(k_0, t) = \bar{u}(k = k_0, t)$ to represent a 1D boundary condition on the solution variable u in any direction k where $k = x$ or $k = y$ and $\bar{u}(k, t)$ is the given functions of time on the boundaries $k = 0$ and $k = 1$ which the solution variable u should match on those boundaries. For example, $\bar{u}(x = 1, t)$ is the given u-velocity at the boundary $x = 1$ and $u(1, t)$ is the corresponding solution to the equations. In 2D, the boundary condition also dependends on the second coordinate direction, which we indicate by $\bar{u}(x = 1, y, t)$ and $\bar{u}(x, y = 1, t)$ for boundary conditions in the x- and y-direction, respectively. Finally, for the discretized 2D boundary conditions, we write instead $\bar{u}_j(x = 1, t) = \bar{u}(x = 1, y_j, t)$ and $\bar{u}_i(y = 1, t) = \bar{u}(x_i, y = 1, t)$.

4.1 Presentation of SAT expressions

SAT expressions for the linear elastic wave equation were derived in [10], here we summarize the findings.

The characteristic variables are $u(k_x, k_y) = T^{-1}(k_x, k_y)\hat{q}$ where $\hat{q} = J^{-1}(u, v, f, g, h)^{\mathrm{T}}$ We form the two sub-vectors corresponding to positive and negative eigenvalues as

$$u^{\mathrm{I}}(k_x, k_y) = (u_1, u_2)^{\mathrm{T}},\ u^{\mathrm{II}}(k_x, k_y) = (u_4, u_5)^{\mathrm{T}} \tag{19}$$

with the aim to form boundary conditions with the matrices R and L. Since many components in $T^{-1}(k_x, k_y)$ occur in positive/negative pairs, it is easy to find 2×2 matrices L and R which, when applied to $u^{\mathrm{I,II}}(k_x, k_y)$ in Eq. (16), isolate the components which we need in order to state the boundary conditions. Eq. (16) now gives our new boundary functions $g^{\mathrm{I}}(k_x, k_y, t)$ and $g^{\mathrm{II}}(k_x, k_y, t)$ as

$$g^{\mathrm{I}}(k_x, k_y, t) = \bar{u}^{\mathrm{I}}(k_x, k_y, k = 0, t) - R\bar{u}^{\mathrm{II}}(k_x, k_y, k = 0, t) \tag{20}$$

$$g^{\mathrm{II}}(k_x, k_y, t) = \bar{u}^{\mathrm{II}}(k_x, k_y, k = 1, t) - L\bar{u}^{\mathrm{I}}(k_x, k_y, k = 1, t) \tag{21}$$

where the functions $\bar{u}^{\mathrm{I,II}}(k_x, k_y, k, t)$ are the previously defined $u^{\mathrm{I,II}}(k_x, k_y)$ from Eq. (19) but with the solution variables substituted for their corresponding time-dependent boundary conditions. Note that L and R are independent of the direction, but depend on the particular type of boundary condition to impose (velocity or traction). For boundary conditions on the velocities u and v, we get using the definitions (20)–(21) and choosing L and R so that the appropriate components of the characteristic variables u are recovered, the following expressions

$$g^{\mathrm{I}}(k_x, k_y, t) = \frac{J^{-1}}{r^2}\begin{bmatrix} \dfrac{\lambda}{\tilde{c}_p}(k_x\bar{u}(k=1,t) + k_y\bar{v}(k=1,t)) \\ \bar{k}(-k_y\bar{u}(k=1,t) + k_x\bar{v}(k=1,t)) \end{bmatrix},\quad R = \begin{bmatrix} 0 & 1 \\ -1 & 0 \end{bmatrix} \tag{22}$$

$$g^{\mathrm{II}}(k_x, k_y, t) = \frac{J^{-1}}{r^2}\begin{bmatrix} \bar{k}(-k_y\bar{u}(k=0,t) + k_x\bar{v}(k=0,t)) \\ \dfrac{\lambda}{\tilde{c}_p}(-k_x\bar{u}(k=0,t) - k_y\bar{v}(k=0,t)) \end{bmatrix},\quad L = \begin{bmatrix} 0 & -1 \\ 1 & 0 \end{bmatrix} \tag{23}$$

where $\bar{u}(k,t), \bar{v}(k,t)$ are the given boundary conditions on u, v at the boundaries.

The boundary conditions on the stresses come from a traction boundary condition of the form $\sigma n = \bar{t}$ where $\bar{t} = (\bar{t}_x, \bar{t}_y)^{\mathrm{T}}$ is the given traction vector from the fluid and σ is the Cauchy stress tensor in the structure $\begin{bmatrix} f & g \\ g & h \end{bmatrix}$. The unit normal n can be expressed in terms of the coordinate transformation (cf. Figure 1) as $n = (1/r)(k_x, k_y)^{\mathrm{T}}$ and the components of g^{I} and g^{II} for traction boundary conditions can be written as

$$g^{\mathrm{I}}(k_x, k_y, t) = \frac{J^{-1}}{r^2}\begin{bmatrix} \dfrac{1}{\alpha r}(k_x\bar{t}_x(k=1,t) + k_y\bar{t}_y(k=1,t)) \\ \dfrac{r\bar{k}}{\rho\tilde{c}_s}(-k_y\bar{t}_x(k=1,t) + k_x\bar{t}_y(k=1,t)) \end{bmatrix},\quad R = \begin{bmatrix} 0 & -1 \\ 1 & 0 \end{bmatrix} \tag{24}$$

$$g^{\mathrm{II}}(k_x, k_y, t) = \frac{J^{-1}}{r^2}\begin{bmatrix} \dfrac{r\bar{k}}{\rho\tilde{c}_s}(k_y\bar{t}_x(k=0,t) - k_x\bar{t}_y(k=0,t)) \\ \dfrac{1}{\alpha r}(k_x\bar{t}_x(k=0,t) + k_y\bar{t}_y(k=0,t)) \end{bmatrix},\quad L = \begin{bmatrix} 0 & 1 \\ -1 & 0 \end{bmatrix} \tag{25}$$

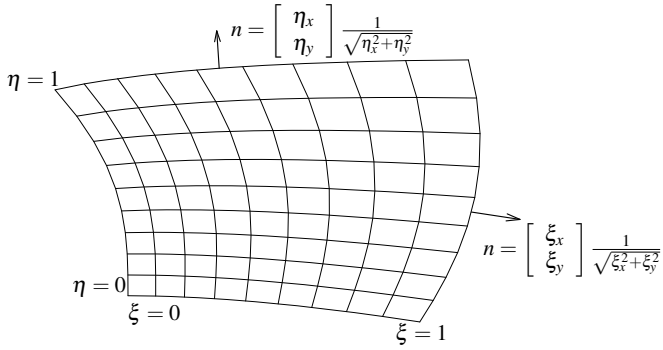

Figure 1: Coordinate transformation

and therefore it is sufficient to specify the two parameters $\bar{t}_x$ and $\bar{t}_y$ on each boundary instead of all of the three $\bar{f}, \bar{g}, \bar{h}$, which might otherwise violate well-posedness.

Inserting the definitions of $g^{\mathrm{I,II}}$ and R, L gives with Eq. (17) a SAT expression (which we call simply SAT) for each of the five equations in characteristic variables. For each of the two spatial directions, the transformation matrix $T(k_x, k_y)$ is applied to get the corresponding SAT expressions in flow variables.

$$\overline{\mathrm{SAT}}_i^{(k)} = T(k_x, k_y)\mathrm{SAT}_i^{(k)}(k_x, k_y) \tag{26}$$

for $k = \xi$ and η. Finally, the total SAT expression is then the sum of the two contributions from the two coordinate directions.

$$\widehat{\overline{\mathrm{SAT}}}_{i,j} = \overline{\mathrm{SAT}}_{i,j}^{(\xi)}(\xi_x, \xi_y) + \overline{\mathrm{SAT}}_{i,j}^{(\eta)}(\eta_x, \eta_y) \tag{27}$$

5 FLUID-STRUCTURE INTERACTION

5.1 Arbitrary Lagrangean–Eulerian (ALE) formulation

The displacement of the structure interface determines the shape of the fluid domain and the structure velocity at the interface determines the internal grid point velocities in the fluid domain. The right and left boundaries of the fluid domain are the out- and inflow, respectively. The top and bottom parts of the fluid domain are bounded by the flexible vocal folds and the inner wall of the airpipe which is assumed to be rigid. As we do not assume symmetry, the motions of the two vocal folds are solved for individually. In our arbitrary Lagrangean–Eulerian (ALE) formulation, the positions and velocities of the grid points in the fluid domain are linearly interpolated from the positions and velocities of the structures at the interfaces. Figure 2 shows the given structure velocities with bold arrows and the interpolated grid point velocities $\dot{x}, \dot{y}$ (thin arrows) for three grid lines.

To obtain the time derivative of J^{-1} as needed in (2), a geometric invariant [17] is used. This geometric conservation law states that $(J^{-1})_\tau + (J^{-1}\xi_t)_\xi + (J^{-1}\eta_t)_\eta = 0$. The time

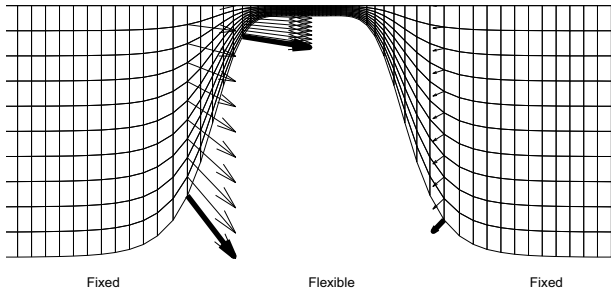

Figure 2: The boundary of the fluid domain consists of fixed and flexible parts. The velocity at the boundary of the flexible part determines the internal grid point velocity. Only half domain shown.

derivatives of the computational coordinates ξ, η can here be obtained from the grid point velocities $\dot{x}, \dot{y}$ as $\xi_t = -(\dot{x}\xi_x + \dot{y}\xi_y)$, $\eta_t = -(\dot{x}\eta_x + \dot{y}\eta_y)$ which can be seen by differentiating the transformation with respect to τ.

5.2 Description of fluid-structure interaction algorithm

At the start of a simulation, we construct the fixed reference configuration for the structure and set the initial variables to zero (no internal stresses and zero velocity). Zero initial conditions are taken for the perturbation variables U' in the fluid domain (stagnation conditions). In the first time step, the fluid domain is uniquely determined by the reference boundary of the structure. To go from time level n to $n+1$, we first take one time step for the fluid with imposed pressure boundary conditions at the inflow and adiabatic no-slip conditions on the walls, i.e. $\mathbf{u} = 0$ and $\partial T/\partial n = 0$. After the first fluid time step, the viscous fluid stress on the wall is calculated based on the new fluid velocities and pressures. These fluid stresses σ^f are passed on to the structure solver via the traction boundary condition. The force per unit area exerted on a surface element with unit normal n is $\bar{t} = \sigma^f n$, where n is here the inward unit normal in the structure, calculated from the displacement vector field.

The traction computed at time level n for the fluid is then used to advance the structure solution to time level $n+1$. The solution for the structure at the new time level gives the velocities and displacements on the boundary, which in turn are used to generate the new fluid mesh and internal grid point velocities. This procedure is repeated for each time step.

6 DISCRETIZATION

Notation

The Kronecker product of an $n \times m$ matrix C and a $k \times l$ matrix D is the $n \times m$ block matrix

$$C \otimes D = \begin{bmatrix} c_{11}D & \cdots & c_{1m}D \\ \vdots & \ddots & \vdots \\ c_{n1}D & \cdots & c_{nm}D \end{bmatrix}. \tag{28}$$

This notation will be useful for writing the discretization in a compact form.

6.1 Linear elastic wave equation

Introduce a vector $\hat{\mathbf{q}} = (\hat{q}_{ijk})^{\mathrm{T}} = (\hat{q}_{001}, ..., \hat{q}_{005}, \hat{q}_{101}, ..., \hat{q}_{105}, ..., \hat{q}_{NM5})^{\mathrm{T}}$ where the three indices i, j and k represent the ξ-coordinate, η-coordinate and the solution variable, respectively. We define difference operators in terms of Kronecker products that operate on one index at a time.

Let $\mathbf{Q}_\xi = Q_\xi \otimes I_M \otimes I_5$ and $\mathbf{Q}_\eta = I_N \otimes Q_\eta \otimes I_5$ where Q_ξ and Q_η are 1D difference operators in the ξ- and η-directions satisfying the SBP property (13). The identity operators I_N and I_M are unit matrices of size $(N+1) \times (N+1)$ and $(M+1) \times (M+1)$, respectively. The computation of the spatial differences of $\hat{\mathbf{q}}$ can then be seen as operating on $\hat{\mathbf{q}}$ with one of the Kronecker products, i.e. $\mathbf{Q}_\eta \hat{\mathbf{q}}$ operates on the second index and yields a vector of the same size as $\hat{\mathbf{q}}$ representing the first derivative approximation in the η-direction. To express the semi-discrete linear elastic wave equation, we also need to define $\hat{\mathbf{A}} = I_N \otimes I_M \otimes \hat{A}$ and $\hat{\mathbf{B}} = I_N \otimes I_M \otimes \hat{B}$. Note that these products are never actually explicitly formed as they are merely theoretical constructs to make the notation more compact. The products correspond well to the actual finite difference implementation, i.e. the first derivatives are calculated by operating on successive lines of values in the computational domain. Using the Kronecker products defined above, the semi-discrete linear elastic wave equation with constant coefficients including the SAT expression can be written as

$$\frac{d\hat{\mathbf{q}}}{dt} = \mathbf{Q}_\xi(\hat{\mathbf{A}}\hat{\mathbf{q}}) + \mathbf{Q}_\eta(\hat{\mathbf{B}}\hat{\mathbf{q}}) + \widehat{\overline{\mathbf{SAT}}} \tag{29}$$

where $\widehat{\overline{\mathbf{SAT}}}$ is the SAT expression in transformed coordinates, defined in Eq. (27).

6.2 Navier–Stokes equations

For the fluid equations, we employ a similar procedure, i.e. we define vectors for the solution variables $\hat{\mathbf{U}}' = (\hat{U}'_{ijk})^{\mathrm{T}} = (\hat{U}'_{001}, ..., \hat{U}'_{004}, \hat{U}'_{101}, ..., \hat{U}'_{104}, ..., \hat{U}'_{NM4})^{\mathrm{T}}$, and the two flux vectors $\hat{\mathbf{F}}'$ and $\hat{\mathbf{G}}'$ similarly defined, where, again, the three indices i, j and k represent the ξ-coordinate, η-coordinate and the solution variable, respectively. The same derivative operators are used as for the linear elastic equation. The discretized fluid equation can

thus be written

$$\frac{d\hat{\mathbf{U}}'}{d\tau} = -\mathbf{Q}_\xi \hat{\mathbf{F}}' - \mathbf{Q}_\eta \hat{\mathbf{G}}' \tag{30}$$

6.3 Time integration

The systems (29) and (30) of ordinary differential equations can readily be solved by the classical 4th order explicit Runge–Kutta method. For the linear elastic wave equation, calling the right-hand side of (29) $\mathbf{f}(t_n, \hat{\mathbf{q}}^n)$ at the time level n, we advance the solution to level $n+1$ by performing the steps

$$\begin{aligned}
\mathbf{k}_1 &= \mathbf{f}(t_n, \hat{\mathbf{q}}^n) \\
\mathbf{k}_2 &= \mathbf{f}\left(t_n + \frac{\Delta t}{2}, \hat{\mathbf{q}}^n + \frac{\Delta t}{2}\mathbf{k}_1\right) \\
\mathbf{k}_3 &= \mathbf{f}\left(t_n + \frac{\Delta t}{2}, \hat{\mathbf{q}}^n + \frac{\Delta t}{2}\mathbf{k}_2\right) \\
\mathbf{k}_4 &= \mathbf{f}(t_n + \Delta t, \hat{\mathbf{q}}^n + \Delta t \mathbf{k}_3) \\
\hat{\mathbf{q}}^{n+1} &= \hat{\mathbf{q}}^n + \frac{\Delta t}{6}(\mathbf{k}_1 + 2\mathbf{k}_2 + 2\mathbf{k}_3 + \mathbf{k}_4)
\end{aligned}$$

and similar expressions for the fluid equations (30). The boundary conditions are updated only after all four stages for the respective field have been completed. That is to say, the structure solution at level $n+1$ is obtained using only the fluid stress at time level n. Likewise, the fluid solution at time level $n+1$ is based only on the position and velocity of the structure at time level n.

7 RESULTS

Verification

Our fluid solver has previously been verified and tested for numerical simulation of Aeolian tones [13] and qualitatively tested for simulation of human phonation on fixed grids [8] as well as moving grids in ALE formulation [7].

The solver for the linear elastic equations with SAT term has been tested with a manufactured solution and an academic 2D test case in [10] where we obtained a rate of convergence of 3.5 to 4 in 2-norm.

7.1 Problem parameters

The initial geometry for the vocal folds is here based on the geometry used in [19] for an oscillating glottis with a given time dependence. The initial shape of the vocal tract including the vocal fold is given as

$$r_w(x) = \frac{D_0 - D_{\min}}{4} \tanh s + \frac{D_0 + D_{\min}}{4}, \tag{31}$$

where r_w is the half height of the vocal tract, $D_0 = 5D_g$ is the height of the channel, $D_g = 4$ mm is the average glottis height, $D_{\min} = 1.6$ mm is the minimum glottis height, $s = b|x|/D_g - bD_g/|x|$, $c = 0.42$ and $b = 1.4$. For $-2D_g \leq x \leq 2D_g$, the function (31) describes the curved parts of the reference configuration for the top and bottom (with a minus sign) vocal folds. The x-coordinates for the in- and outflow boundaries are $-4D_g$ and $10D_g$, repectively.

7.2 Vocal fold material parameters

The density in the reference configuraiton is $\rho_0 = 1043\,\mathrm{kg/m^3}$, corresponding to the measured density of vocal fold tissue as reported by [6]. The Poisson ratio was chosen as $\nu = 0.47$ for the tissue, corresponding to a nearly incompressible material with $\nu = 0.5$ being the theoretical incompressible limit. The Lamé parameters were chosen as $\mu = 3.5\,\mathrm{kPa}$ and λ given by $\lambda = 2\mu\nu/(1-2\nu)$.

7.3 Fluid model

We used a Reynolds number of 3000 based on the average glottis height $D_g = 0.004\,\mathrm{m}$ and an assumed average velocity in the glottis of $U_m = 40\,\mathrm{m/s}$. We used these particular values in order to be able to compare with previously published results by Zhao *et al.* [19, 18] and by ourselves [7, 8]. The Prandtl number was set to 1.0, and the Mach number was 0.2, based on the assumed average velocity and the speed of sound. We deliberately used a lower value for the speed of sound, $c_0 = 200\,\mathrm{m/s}$ in order to speed up the computations. The air density was $1.3\,\mathrm{kg/m^3}$ and the atmospheric pressure was $p_{\mathrm{atm}} = 101325\,\mathrm{Pa}$. The equation of state was the perfect gas law, and we assumed a Newtonian fluid. At the inlet, we imposed a typical lung pressure during phonation with a small unsymmetric perturbance by setting the acoustic pressure to $p_{\mathrm{acoustic}} = p - p_{\mathrm{atm}} = (1 + 0.025\sin 2\pi\eta)2736\,\mathrm{Pa}$, where $\eta = 0$ at the lower vertex and $\eta = 1$ at the upper vertex of the inflow boundary. The outlet pressure was set to atmospheric pressure, i.e. $p - p_{\mathrm{atm}} = 0\,\mathrm{Pa}$.

7.4 Numerical simulation

Both fluid and structure used the same set of variables for nondimensionalization and the same time step was used for both fields so that the two solutions are always at the same time level. The structure grid consisted of 81×61 points for each vocal fold, i.e. for the upper and the lower vocal folds, and the fluid domain was 241×61 points. The time step was determined by the stability condition for the fluid, which was satisfied here by requiring $CFL \leq 1$. Since the fluid domain changes with time, the CFL condition puts a stricter constraint on the time step when the glottis is nearly closed. The solution was marched in time with given initial and boundary conditions to dimensional time $t = 12\,\mathrm{ms}$ (total number of time steps 277310).

The solution was first integrated to time $t = 6\,\mathrm{ms}$ so that the effect of initial conditions

would be negligible. After that, the solution was recorded at consecutive 2 ms intervals as shown in Figure 3 where the vorticity is depicted in the left column and the corresponding pressure field is on the right.

Initially, a starting jet is formed in the glottis which becomes unstable near the exit and creates the beginnings of vortical structures at time $t = 6$ ms. Since the boundary conditions are not symmetric with respect to the centerline, also the solution is not symmetric. In the following, vortices are shed near the glottis and propagated downstream driven by the pressure gradient. The pressure plots indicate a sharp pressure drop just before the orifice. Downstream, the pressure minima occur in the vortex centers, as expected.

8 CONCLUSIONS

Our 2D model for the vocal folds based on the linear elastic wave equation in first order form and the air flow based on the compressible Navier–Stokes equations in the vocal tract proves to be able to capture the self-sustained pressure-driven oscillations and vortex generation in the glottis. The high order method for the linear elastic wave equation with a SAT formulation for the boundary conditions ensures a time-stable solution. The fluid and structure fields are simultaneously integrated explicitly in time and boundary data is exchanged only at the end of a time step. With this formulation, there is no need to do iterations in order to find the equilibrium displacement for the structure depending on the fluid stresses. For the problem we consider here, the limiting factor on the time step is the CFL condition from the compressible Navier–Stokes equations. Since the fluid grid has many more grid points, the effort of integrating the linear elastic wave equation, to get the structure displacement, is sub-dominant.

9 ACKNOWLEDGEMENTS

The authors thank Bjørn Skallerud, Paul Leinan and Victorien Prot at the Department of Structural Engineering, NTNU for valuable discussions on the structure model and for Abaqus support. The current research has been funded by the Swedish Research Council under the project "Numerical Simulation of Respiratory Flow".

REFERENCES

[1] M. H. Carpenter, D. Gottlieb, and S. Abarbanel. Time-stable boundary conditions for finite-difference schemes solving hyperbolic systems: Methodology and application to high-order compact schemes. *J. Comp. Phys.*, 111:220 – 236, 1994.

[2] B. Fornberg. *A Practical Guide to Pseudospectral Methods*. Cambridge University Press, 1998.

[3] J.B. Grotberg and O.E. Jensen. Biofluid mechanics in flexible tubes. *Annu. Rev. Fluid Mech*, 36:121 – 147, 2004.

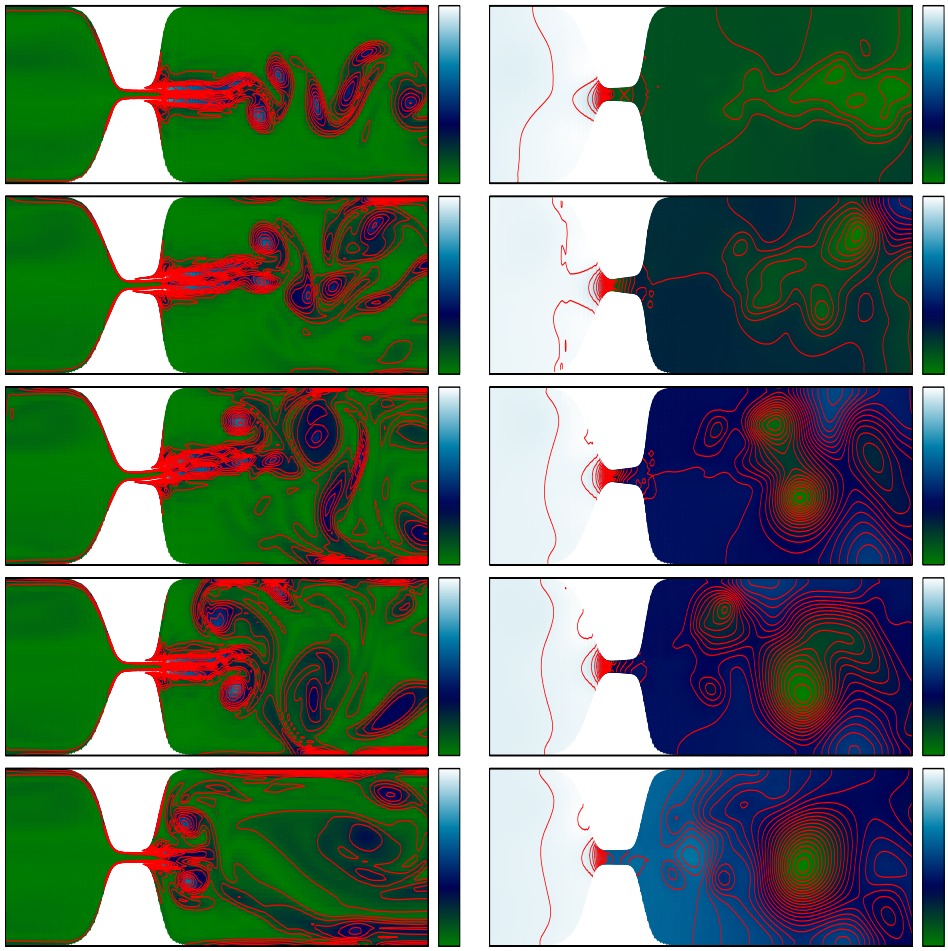

Figure 3: Vorticity and pressure contours at 2 ms intervals. The left column shows vorticity contours, the right column shows pressure contours. The top row shows the solution evaluated at $t = 6\,\mathrm{ms}$, the second row is at $t = 8\,\mathrm{ms}$ and so on up to $t = 14\,\mathrm{ms}$ (last row). The colorbar in the vorticity column stretches from 0 to $50\,000\,\mathrm{s}^{-1}$ and the contour levels are spaced $3\,750\,\mathrm{s}^{-1}$ apart. For the pressure column, the inflow is at $p = p_\infty + \Delta p$, the outflow is at (approximately) $p = p_\infty$ and the contour levels are spaced 71 Pa apart.

[4] B. Gustafsson. *High order difference methods for time-dependent PDE*. Springer-Verlag Berlin Heidelberg, 2008.

[5] B. Gustafsson, H.-O. Kreiss, and J. Oliger. *Time Dependent Problems and Difference Methods*. John Wiley & Sons, New York, 1995.

[6] E.J. Hunter, I.R. Titze, and F. Alipour. A three-dimensional model of vocal fold abduction/adduction. *J. Acoust. Soc. Am.*, 115(4):1747 – 1759, 2004.

[7] M. Larsson. Numerical Simulation of Human Phonation, Master Thesis, Uppsala University, Department of Information Technology, 2007.

[8] M. Larsson and B. Müller. Numerical simulation of confined pulsating jets in human phonation. *Computers & Fluids*, 38:1375 – 1383, 2009.

[9] M. Larsson and B. Müller. Numerical simulation of fluid-structure interaction in human phonation. In B. Skallerud and H.I. Andersson, editors, *MekIT 09 Fifth national conference on Computational Mechanics*, pages 261 – 280, Trondheim, Norway, 2009. Tapir Academic Press.

[10] M. Larsson and B. Müller. Strictly stable high order difference method for the linear elastic wave equation. 2010. Submitted to Commun. Comput. Phys.

[11] R.J. LeVeque. *Finite volume methods for hyperbolic problems*. Cambridge University Press, 2002.

[12] B. Müller. Computation of compressible low Mach number flow, Habilitation Thesis, ETH Zürich, 1996.

[13] B. Müller. High order numerical simulation of aeolian tones. *Computers & Fluids*, 37(4):450 – 462, 2008.

[14] T.J. Poinsot and S.K. Lele. Boundary conditions for direct simulations of compressible viscous flows. *J. Comput. Physics*, 101:104 – 129, 1992.

[15] J. Sesterhenn, B. Müller, and H. Thomann. On the cancellation problem in calculating compressible low Mach number flows. *J. Comput. Physics*, 151:597 – 615, 1999.

[16] B. Strand. Summation by parts for finite difference approximations for d/dx. *J. Comput. Physics*, 110:47 – 67, 1994.

[17] M.R. Visbal and D.V. Gaitonde. On the use of higher-order finite-difference schemes on curvilinear and deforming meshes. *J. Computat. Physics*, 181:155 – 185, 2002.

[18] C. Zhang, W. Zhao, S.H. Frankel, and L. Mongeau. Computational aeroacoustics of phonation, Part II. *J. Acoust. Soc. Am.*, 112(5):2147 – 2154, 2002.

[19] W. Zhao, S.H. Frankel, and L. Mongeau. Computational aeroacoustics of phonation, Part I: Computational methods and sound generation mechanisms. *J. Acoust. Soc. Am.*, 112(5):2134 – 2146, 2002.